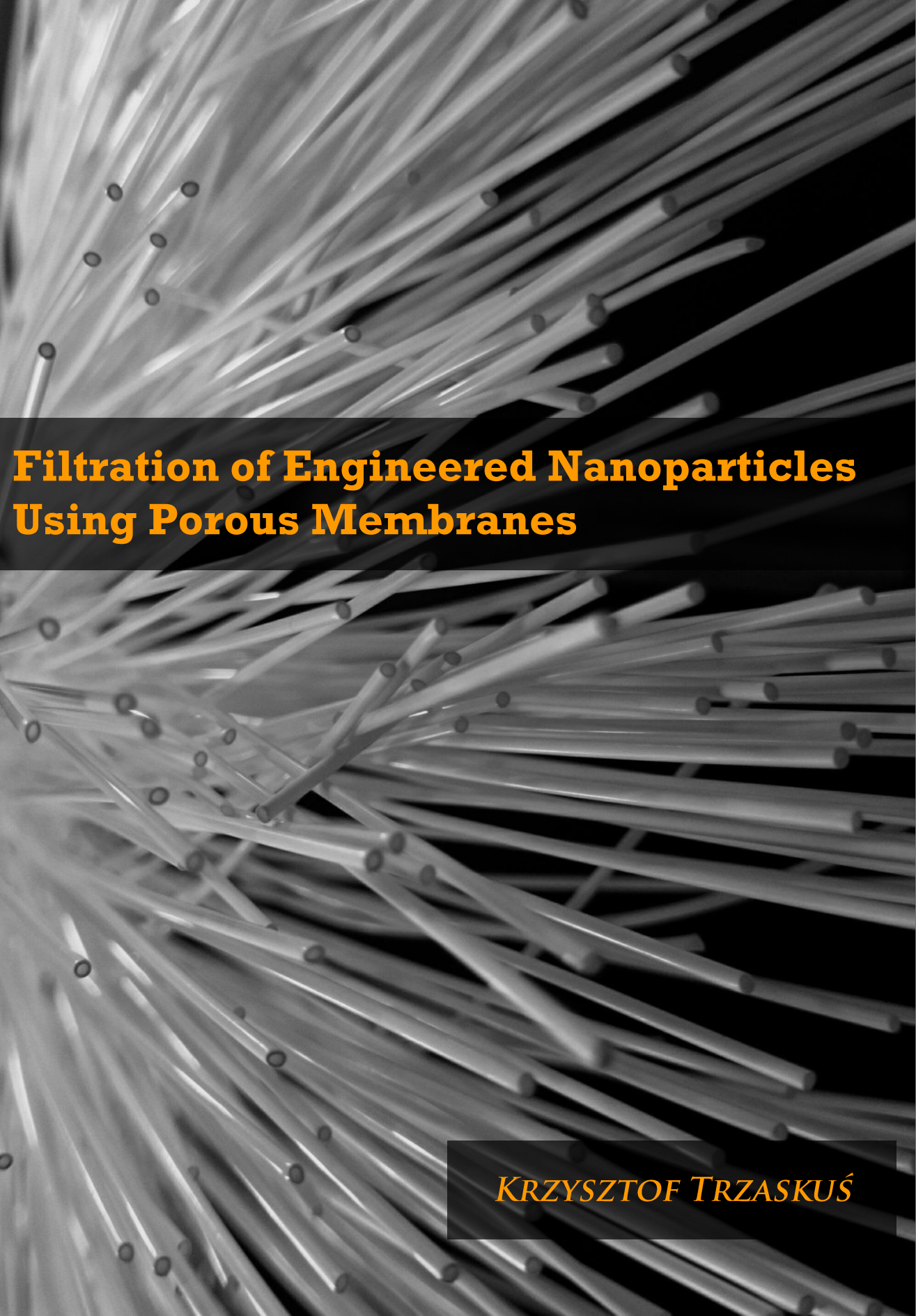

Filtration of Engineered Nanoparticles Using Porous Membranes

Krzysztof Trzaskuś

FILTRATION OF ENGINEERED NANOPARTICLES USING POROUS MEMBRANES

Krzysztof Trzaskuś

This work was supported by NanoNextNL, a micro- and nanotechnology consortium of the government of the Netherlands and 130 partners.

Promotion Committee

Chairman:	
Prof. Dr. J.W.M. Hilgenkamp	University of Twente
Promotor:	
Prof. Dr. Ir. D.C. Nijmeijer	University of Twente
Assistant promotor:	
Dr. Ir. A.J.B. Kemperman	University of Twente
Members:	
Dr. Pierre Aimar	University of Toulouse
Prof. Dr. Ir. W.G.J. van der Meer	Delft University of Technology
Prof. Dr. Ir. C.G.P.H. Schroën	Wageningen University
Prof. Dr. -Ing. Matthias Wessling	University of Twente
Prof. Dr. Ir. R.G.H. Lammertink	University of Twente

Cover design: Krzysztof Trzaskuś

Filtration of Engineered Nanoparticles using Porous Membranes
ISBN: 978-90-365-4045-2
DOI: 10.3990/9789036540452
URL: http://dx.doi.org/10.3990/1.9789036540452
Printed by Gildeprint Drukkerijen

FILTRATION OF ENGINEERED NANOPARTICLES USING POROUS MEMBRANES

DISSERTATION

to obtain
the degree of doctor at the University of Twente,
on the authority of the rector magnificus,
Prof. Dr. H. Brinksma
on account of the decision of the graduation committee,
to be publicly defended
on Friday the 5th of February 2016 at 16.45

by

Krzysztof Wojciech Trzaskuś
born on July 28th, 1987

in Dębica, Poland

This thesis has been approved by:

Prof. Dr. Ir. D.C. Nijmeijer (promotor)
Dr. Ir. A.J.B. Kemperman (assistant-promotor)

Contents

CHAPTER 1

Introduction

1.1. Engineered nanoparticles

The last two decades can be considered as the decades of the nanotechnology revolution [1]. Technological progress enabled the manipulation and characterization of atoms and molecules at the nanoscale resulting in a booming production and application of nanotechnology-based goods [2-4]. The nanoparticles intermediate size between the macroscopic and molecular level is responsible for their unique physical properties of nanomaterials [5] and allowed the development of novel and exciting products. Their high surface-area-to-volume ratio and especially quantum effects of the nanoparticles have a tremendous impact on the catalytic, optical, mechanical and electrical properties of such nanomaterials [6]. Furthermore, these properties may change with the size of the nanoparticles, and they can be considerably different than those observed on the macroscale.

The exact definition of nanoparticles is controversial; however, the most accurate seems to be the one which states that nanoparticles are particles with three dimensions in the size range between 1 nm and 100 nm [7]. According to this definition, a nanoparticle suspension is nothing else than a special and narrower group of colloids, for which the size is typically defined as between 1 nm and 1000 nm, as schematically illustrated in Fig. 1.

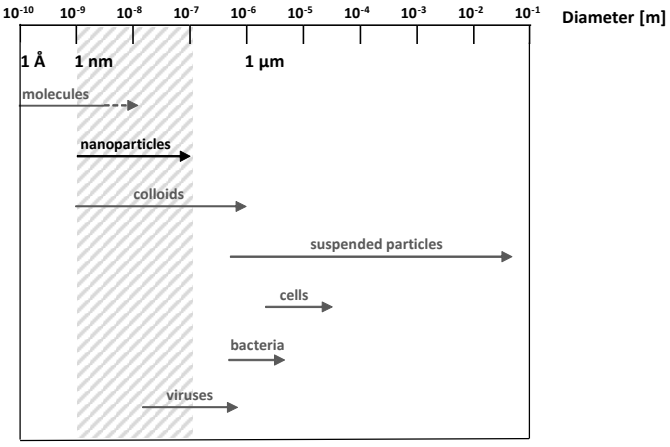

Fig. 1. Sizes of different particle suspensions (adapted from [8]).

Nanoparticles can be categorized into three main groups: natural, incidental and engineered nanoparticles [9]. Natural nanoparticles are nano-scale materials occurring in

nature, such as proteins, viruses, minerals, clays etc. [10]. Incidental nanoparticles originate from combustion processes and industrial emissions [11], whereas engineered nanoparticles are manufactured specifically for such application as cosmetics, drugs, paints, food, textiles etc. [12-14]. Engineered nanoparticles can be roughly classified into several groups according to their chemical composition, as summarized in Table 1.

Table 1. Classification of engineered nanoparticles according to their chemical composition (adapted from [15]).

Category	**Examples**
Metals	Silver (Ag), Iron (Fe), Gold (Au), Copper (Cu)
Oxides	Zinc oxide (ZnO), Titanium dioxide (TiO_2), Aluminum oxide (Al_2O_3), Iron oxides (FeO, Fe_2O_3)
Carbon based	Fullerene, Single-walled carbon nanotubes (SWCNT), Multi-walled carbon nanotubes (MWCNT)
Complex compounds	Quantum dots e.g. Cadmium-selenium (CdSe), Alloys e.g. Iron-nickel (Fe-Ni)
Polymers	Polystyrene (PS), Polyphenylene dendrimers

1.2. Nanoparticles in drinking water and their toxicity

Extensive application of engineered nanoparticles in commercial products results in their release into the environment and accumulation in various water sources [16-19]. The estimated concentration of engineered nanoparticles in surface waters is expected to vary from ng/L scale (e.g. for Ag NPs, CNT) to μg/L scale (e.g. for TiO_2) [20-22]. However, due to the continuously increasing production volume of nanoparticles, accumulation of nanoparticles in water sources is likely to increase in the coming years [23, 24]. Moreover, numerous researchers have suggested that some of the engineered nanoparticles are potentially toxic for aquatic life and human health. For example, a recently published review by Liu et al. [25] on nanoparticle toxicity in wastewaters has shown that fullerenes, some metal oxide nanoparticles, metal nanoparticles, quantum dots and CNTs are toxic towards aquatic organisms and the exposure to engineered nanoparticles leads to significantly higher mortality of various animal species. These

engineered nanoparticles can penetrate human cell membranes enabling interactions of the nanoparticles with cellular organelles, proteins and DNA chains [26]. Transport into the cell and the high redox activity of nanoparticles are mainly responsible for destruction of the cell functionality [27]. However, surface chemistry, size and surface charge of nanoparticles are found also to be equally important in defining their toxicity [25, 28]. Furthermore, various pollutants, heavy metals and dyes may easily adsorb onto the nanoparticle surface, thus allowing their synergistic uptake [29-31].

Due to the concerns related to nanoparticle toxicity, more and more the question is raised how to develop and use nanoparticle-based products in a sustainable way. As a result, attention has been drawn to technologies that can efficiently remove manufactured nanoparticles from e.g. drinking water sources or industrial waste streams [32-34].

1.3. Nanoparticle stability

Suspensions of engineered nanoparticles in water can be classified as lyophobic colloids that are thermodynamically unstable due to their very high surface energy [35]. Kinetically, however, their coagulation can be delayed and nanoparticles often appear to be stable in suspension due to the presence of an energy barrier for aggregation.

An example of kinetic stabilization is electrostatic stabilization. Here, nanoparticles maintain their dispersed state due the presence of charges on the surface of the nanoparticles. The most established theory describing the electrostatic stability of particles was developed by Derjaguin, Landau, Verwey and Overbeek, and is known as the DLVO theory. According to this theory, the overall potential energy of interactions V_t (J) between particles is the sum of the attractive V_a (J) and repulsive potentials V_r (J):

$$V_t = V_a + V_r \tag{1}$$

The attractive potentials arise from long-range van der Waals forces, which originate from dipolar interactions between the molecules in the particles. For identical spherical particles with radius r (m) and separation distance s (m), the potential energy of nanoparticle attraction is described by Eq. 2:

$$V_a = \frac{-Hr}{12s} \tag{2}$$

H is Hamaker constant (J), which accounts for London attraction of the molecules building two separate particles. In a liquid medium this is defined as an effective Hamaker constant according to Eq. 3:

$$H = (\sqrt{H_n} - \sqrt{H_l})^2 \tag{3}$$

where H_n and H_l are the Hamaker constants (J) of the particles and the liquid, respectively.

The repulsive potential arises from the electrical double layer surrounding the particles. The charged surface of the particles attracts oppositely charged ions, leading to the partial neutralization of the surface and the formation of an electrical potential. This potential decays exponentially with the distance from the surface of the particle to the bulk of the solution. The repulsive potential can by calculated according to the approximations given in Eq. 4 and Eq. 5:

$$V_r = 2\pi\varepsilon_0\varepsilon_r r\psi_0^2 \exp(-\kappa s) \qquad \text{for} \quad \kappa r << 1 \tag{4}$$

$$V_r = 2\pi\varepsilon_0\varepsilon_r r\psi_0^2 \ln(1-\exp(-\kappa s)) \qquad \text{for} \quad \kappa r >> 1 \tag{5}$$

where ε_0 is the dielectric constant of vacuum ($C^2/J{\cdot}m$), ε_r is the dielectric constant of the medium ($C^2/J{\cdot}m$), r is the radius of the particle (m), ψ_0 is the surface potential of the particle (V), s is the separation distance between two particles (m) and κ is the inverse of the Debye length (1/m) defined as:

$$\kappa = \sqrt{\frac{2e^2 N_A I}{\varepsilon_0\varepsilon_r kT}} \tag{6}$$

where e is the elemental charge (C), N_A is the Avogadro number (1/mol), k is the Boltzmann constant (J/K), T is the temperature (K) and I is the ionic strength (mol/m^3). Often, the overall total potential energy of interactions is plotted as a function of the separation distance between the particles, as illustrated in Fig. 2.

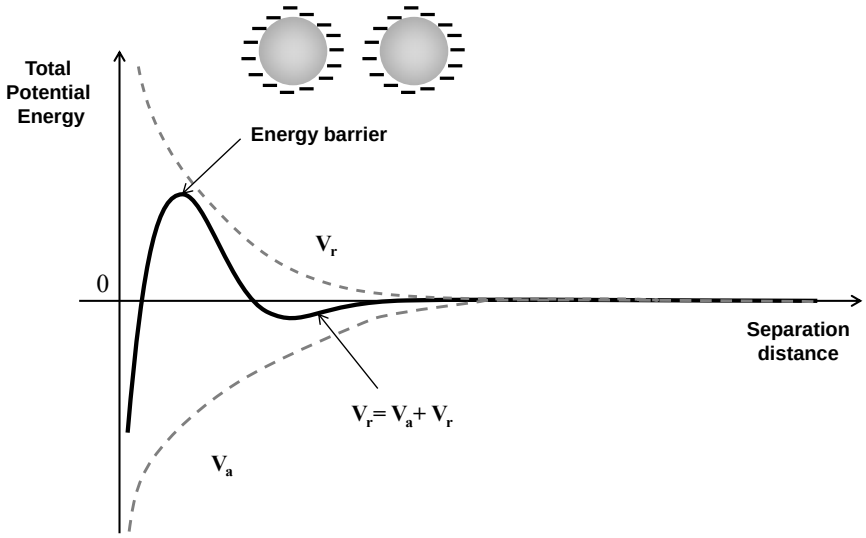

Fig. 2. Interaction energy between electrostatically stabilized particles in a suspension as a function of separation distance between the nanoparticles.

Generally speaking, stable colloidal suspensions exhibit an energy barrier higher than 10-15 kT, whereas unstable suspensions have an interaction energy below 3 kT. Suspensions with an energy barrier between 3 kT and 15 kT are semi-stable, meaning that their aggregation rate is strongly time- and concentration dependent [36]. Furthermore, electrostatically stabilized particles are very sensitive to the solution properties, such as pH, the presence of salt additives, and ionic strength.

Frequently, in order to improve nanoparticle stability, various types of stabilizers are added to nanoparticle suspensions. These stabilizers adsorb onto the nanoparticle surface, thereby enhancing the repulsive interactions between the nanoparticles. Low-molecular weight organic compounds such as carboxylic acids [37], alcohols [38], amines [39] or surfactants [40] are commonly used to enhance electrostatic interactions between particles [35].

In addition, also high-molecular weight compounds such as synthetic polymers [41], proteins [42] or polysaccharides [43] can be used to introduce steric stabilization of the nanoparticles. This type of particle stabilization is attributed to the thermodynamic penalty when particles that are coated by polymer chains come closer to each other. In this situation, polymer chains are confined to a smaller volume. This induces an entropy reduction and causes effective repulsive interactions between the particles. As it is in the

case for electrostatic stabilization (Fig. 2), also the total potential energy of interactions for steric stabilization has a typical pattern, as plotted in Fig. 3.

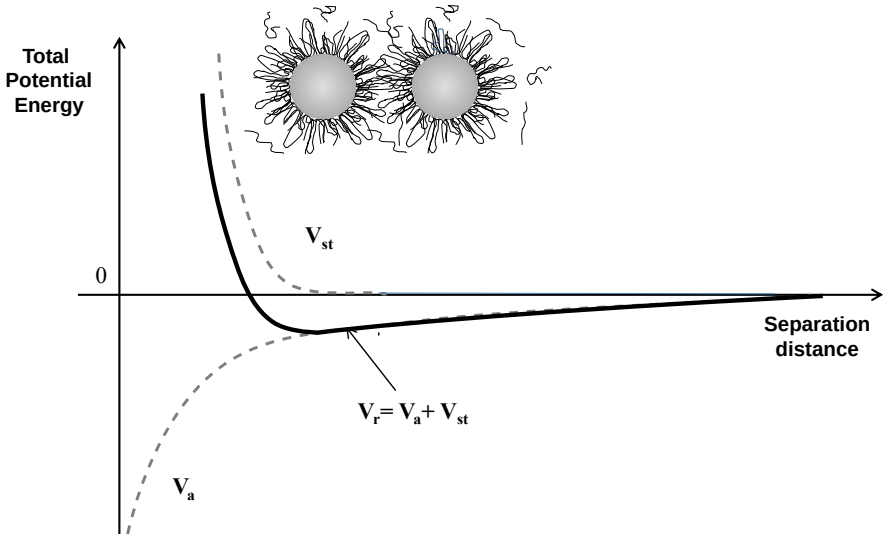

Fig. 3 Interaction energy between sterically stabilized particles in a suspension as a function of separation distance between the nanoparticles.

Engineered nanoparticles can also be stabilized by a third type of stabilization: depletion stabilization. In contrast to steric stabilization, in this type of particle stabilization the polymer does not adsorb onto the particle but it occupies the space between the particles, thus limiting collisions between particles. Nevertheless, there is no full agreement on the origin of depletion stabilization. According to the theory given by Feign and Napper [44] it has a kinetic nature, meaning that there exists an energy barrier that needs to be overcome before aggregation of the nanoparticles will occur. However, Fleer et al. [45] postulated that such a specific energy barrier does not exist and that depletion stabilization of nanoparticles has a purely thermodynamic origin.

In contrast, many additives present in nanoparticle suspensions can induce exactly the opposite behavior, i.e. destabilize the particles thus induce their agglomeration. As an example, neutralization of the nanoparticle surface charge leads to reduction of the electrostatic repulsion between nanoparticles and aggregation may occur [46-48]. Addition of high-molecular weight polymers to nanoparticles with a not fully saturated polymer layer may lead to so-called flocculation bridging [49] or depletion aggregation [50].

1.4. Membrane filtration of engineered nanoparticles

As a result of their size range, colloidal particles such as humic acids [51], proteins [52], polysaccharides [53] or inorganic clays [54] can be retained using membrane filtration. Since nanoparticles are a special group of colloids, the general mechanisms responsible for the filtration of colloidal particles are to a large extend also valid for engineered nanoparticles. Nevertheless, additional effects do play a role and systematic studies describing membrane filtration of engineered nanoparticles and (synergistic) fouling phenomena encountered are rarely reported.

From a macroscopic point of view, retention of nanoparticles by membranes mainly occurs due to size exclusion that is combined with the accumulation of mass on the membrane surface [55]. The inevitable consequence of membrane selectivity is flux decline, which originates from concentration polarization and/or fouling phenomena. Reversible accumulation of the solute on the membrane surface is referred to as concentration polarization. In this process, the retained solutes form a concentration gradient perpendicular to the membrane surface that creates a driving force for back diffusion of the particles towards the bulk of the solution [56]. Fouling is the built-up of material on the membrane surface due to adsorption, pore blockage, solute deposition or gel layer formation [56]. Both phenomena contribute to an increase of the hydraulic resistance. According to the resistance-in-series approach, the flux decline in a filtration process can be written as [57]:

$$J = \frac{\Delta P - \Delta \pi}{\mu(R_m + R_{cp} + R_a + R_{pb} + R_c)} \tag{7}$$

Where J is the volumetric flux ($m^3/m^2 \cdot s$), ΔP is the transmembrane pressure (Pa), $\Delta\pi$ is the osmotic pressure (Pa), η is the viscosity (Pa·s), R_m is the membrane resistance (1/m), R_{cp} is the resistance due to concentration polarization (1/m), R_a is the resistance due to adsorption (1/m), R_{pb} is the resistance due to pore blockage (1/m) and R_{cp} is the resistance due to cake filtration (1/m).

From a fundamental point of view, the transport of the solute towards the membrane surface is driven by the convective flux towards the membrane surface, back diffusion of the solute, membrane-solute and solute-solute surface interactions, and hydrodynamic conditions [56]. Together these contributions determine the net flux of solute towards the membrane and this flux can be described according to Eq. 8.

$$N = JC - D\frac{dC}{dy} + p(\zeta) + q(\tau) \tag{8}$$

where N is the flux of the solute towards the membrane (kg/m^2·s), J is the volumetric flux (m^3/m^2·s), and C is the concentration of the solute (kg/m^3). D is the Brownian diffusion coefficient (m^2/s) and dC/dy is the concentration gradient of solute accumulated on the membrane surface (kg/m^4), whose product describes back transport of the solute. $p(\zeta)$ stands for one or more functions describing the transport of the solute due to the surface interactions ζ. $p(\zeta)$ can be positive if the attractive interactions between the membrane surface and the solute dominate. If these interactions are repulsive (for example due to electrostatic or steric repulsions), this term becomes negative. After coverage of the membrane surface with a monolayer of a solute, membrane-solute interactions are substituted by solute-solute interactions [58]. The contribution of local hydrodynamics to the solute flux is described by the $q(\tau)$ term that accounts for the presence of shear-induced diffusion, internal lift, cake rolling and cake flowing, which are all induced by a shear rate τ [59]. In general, with decreasing solute size, the contribution of back diffusion and surface interactions becomes more important [56]. Consequently, due to the small size of the nanoparticles, these two terms are expected to be substantial for their filtration behavior.

The convective flux towards the surface membrane concentrates the nanoparticles at the membrane boundary layer. The separation distance between nanoparticles reduces and in an extreme case, the drag force originating from the convective flux overcomes the energy barrier against nanoparticle aggregation. As a result, an aggregate phase could be formed at the membrane surface [60]. Due to the larger size of the nanoparticle aggregates, their diffusion coefficient reduces and the contribution of back diffusion on the net flux towards the membrane vanishes. Hence, the aggregates deposit on the membrane surface, forming a fouling layer and the transition from concentration polarization (dispersed state of nanoparticles) to fouling (aggregate deposition) takes place [61]. The conditions at which this transition occurs, are the so-called critical conditions such as the critical nanoparticle concentration [62], the critical flux [63], the critical filtration volume [64] etc. These critical conditions depend strongly on the nanoparticle stability. The higher the stability of the nanoparticles, the higher the critical value will be and less pronounced fouling is observed. In that sense, stabilizers added to nanoparticle suspensions have the potential to decrease the fouling tendency of the nanoparticles. On the other hand, stabilizers also represents additional foulants. As such, when retained by the membrane, also the stabilizers themselves contribute to the hydraulic resistance. An inappropriate type of stabilizer or an inadequate concentration may destabilize the nanoparticle suspension at the membrane surface and enhance

fouling. Aggregation of nanoparticles into larger particles in the bulk of the solution (so before reaching the membrane surface), can however also lead to the formation of a more porous deposit, thus reducing the filtration resistance again.

1.5. Problem definition and scope of the thesis

As briefly described above, fouling behavior of engineered nanoparticles is a delicate balance between the dispersed and the aggregated phase of engineered nanoparticles at the membrane-feed interface. Obviously, due to an increase of the nanoparticle size, the aggregation process influences pore blockage and deposition of nanoparticles on the membrane surface, which inevitably influences nanoparticle rejection. Moreover, differences in retention of a porous membrane towards nanoparticles and stabilizers may additionally complicate accurate prediction of fouling development during the filtration of stabilized nanoparticles.

Although membrane filtration of colloidal particles in general is rather well described in the literature, not much is known about filtration and synergistic fouling of engineered nanoparticles in the presence of additional stabilizers. Therefore, this research investigates and elucidates mechanisms responsible for fouling and rejection development by porous membranes during filtration of model engineered nanoparticles. This work includes:

- A detailed description of fouling development during membrane dead-end filtration, which contains determination of fouling stages and parameters influencing the duration and severity of the fouling.
- Comparison of various types of nanoparticle stabilization and the investigation of their role in the formation of a nanoparticles deposit on the membrane surface and nanoparticle rejection during filtration.
- Description of the hydrodynamic parameters responsible for the uniformity of membrane fouling along a porous hollow fiber membrane.

1.6. Outline

This thesis describes the filtration of engineered nanoparticles using hollow fiber dead-end filtration with a main focus on nanoparticle stability and their role in fouling development.

Chapter 2 investigates the fouling mechanisms occurring during constant pressure dead-end microfiltration of electrostatically stabilized silica nanoparticles that are much smaller than the pores of the membrane. The proposed fouling mechanism consists of 5 stages: 1) nanoparticle adsorption onto the membrane; 2) transport of the nanoparticles through the membrane pores; 3) pore blocking; 4) cake filtration and 5) cake maturation. The role of nanoparticle stability on fouling severity is elucidated.

Chapter 3 studies the influence of silica nanoparticle size and polydispersity on fouling development and nanoparticle rejection.

Chapter 4 considers the filtration and synergistic fouling of sterically stabilized silica nanoparticles. The impact of molecular mass and concentration of the steric stabilizer on the nanoparticle stability upon nanoparticle rejection and permeate flux decay is investigated.

Chapter 5 describes the filtration behavior of the silica nanoparticles in a mixture with surfactants. The effect of the type of surfactant applied and its concentration on the nanoparticle stability and the filtration behavior of the nanoparticles is evaluated.

Chapter 6 investigates the axial dependency of fouling development and nanoparticle rejection along the hollow fiber membrane. This chapter investigates the uniformity of the nanoparticle deposition along the fiber length during hollow fiber dead-end filtration.

Finally, the main conclusions of this work are presented in **Chapter 7**. It also provides recommendations for future work on nanoparticle filtration.

References

[1] K. E. Drexler, Engines of Creation: The Coming Era of Nanotechnology. London: Fourth Estate Ltd., 1996.

[2] S. F. Hansen, E. S. Michelson, A. Kamper, P. Borling, F. Stuer-Lauridsen, A. Baun, Categorization framework to aid exposure assessment of nanomaterials in consumer products, Ecotoxicology 17 (2008) 438-47

[3] R. J. Aitken, M. Q. Chaudhry, A. B. A. Boxall, M. Hull, Manufacture and use of nanomaterials: current status in the UK and global trends, Occ. Med. 56 (2006) 300-306

[4] T. Tsuzuki, Commercial scale production of inorganic nanoparticles, Int. J. Nanotechnol. 6 (2009) 567-578

[5] Y. Ju-Nam, J. R. Lead, Manufactured nanoparticles: An overview of their chemistry, interactions and potential environmental implications, Sci. Total Environ. 400 (2008) 396-414

[6] E. Roduner, Size matters: why nanomaterials are different, Chem. Soci. Rev. 35 (2006) 583-592

[7] V. Stone, B. Nowack, A. Baun, N. van den Brink, F. von der Kammer, M. Dusinska, et al., Nanomaterials for environmental studies: Classification, reference material issues, and strategies for physico-chemical characterisation, Sci. Total Environ. 408 (2010) 1745-1754

[8] F. H. Frimmel, M. Delay, "Introducing the “Nano-world”," in Nanoparticles in the Water Cycle, F. H. Frimmel,R. Niessner, Eds., ed: Springer Berlin Heidelberg, 2010, pp. 1-11.

[9] M. Farré, J. Sanchís, D. Barceló, Analysis and assessment of the occurrence, the fate and the behavior of nanomaterials in the environment, Trends Anal. Chem. 30 (2011) 517-527

[10] M. S. Jiménez, M. T. Gómez, E. Bolea, F. Laborda, J. Castillo, An approach to the natural and engineered nanoparticles analysis in the environment by inductively coupled plasma mass spectrometry, Int. J. Mass Spectrom. 307 (2011) 99-104

[11] M. R. Wiesner, D. L. Plata, Environmental, health and safety issues: Incinerator filters nanoparticles, Nat. Nano. 7 (2012) 487-488

[12] A. Weir, P. Westerhoff, L. Fabricius, K. Hristovski, N. von Goetz, Titanium dioxide nanoparticles in food and personal care products, Environ. Sci. Technol. 46 (2012) 2242-2250

[13] J.-H. Lim, P. Sisco, T. K. Mudalige, G. Sánchez-Pomales, P. C. Howard, S. W. Linder, Detection and characterization of SiO2 and TiO2 nanostructures in dietary supplements, J. Agric. Food Chem. 63 (2015) 3144-3152

[14] R. B. Reed, J. J. Faust, Y. Yang, K. Doudrick, D. G. Capco, K. Hristovski, et al., Characterization of nanomaterials in metal colloid-containing dietary supplement drinks and assessment of their potential interactions after ingestion, ACS Sustainable Chem. Eng. 2 (2014) 1616-1624

[15] P. N. L. Lens, J. Virkutyte, V. Jegatheesan, S.-H. Kim, S. Al-Abed, Nanotechnology for water and wastewater treatment. London: IWA Publishing, 2013.

[16] A. P. Gondikas, F. von der Kammer, R. B. Reed, S. Wagner, J. s. F. Ranville, T. Hofmann, Release of TiO2 nanoparticles from sunscreens into surface waters: A one-year survey at the old danube recreational lake, Environ. Sci.Technol. 48 (2014) 5415-5422

[17] L. Windler, C. Lorenz, N. von Goetz, K. Hungerbühler, M. Amberg, M. Heuberger, et al., Release of titanium dioxide from textiles during washing, Environ. Sci. Technol. 46 (2012) 8181-8188

[18] T. V. Duncan, K. Pillai, Release of engineered nanomaterials from polymer nanocomposites: Diffusion, dissolution, and desorption, ACS Appl. Mater. Interfaces 7 (2015) 2-19

[19] N. von Goetz, C. Lorenz, L. Windler, B. Nowack, M. Heuberger, K. Hungerbühler, Migration of Ag- and TiO2-(Nano)particles from textiles into artificial sweat under physical stress: Experiments and exposure modeling, Environ. Sci. Technol. 47 (2013) 9979-9987

[20] F. Gottschalk, T. Sonderer, R. W. Scholz, B. Nowack, Modeled environmental concentrations of engineered nanomaterials (TiO2, ZnO, Ag, CNT, Fullerenes) for Different Regions, Environ. Sci. Technol. 43 (2009) 9216-9222

[21] N. C. Mueller, B. Nowack, Exposure modeling of engineered nanoparticles in the environment, Environ. Sci. Technol. 42 (2008) 4447-4453

[22] P. Westerhoff, G. Song, K. Hristovski, M. A. Kiser, Occurrence and removal of titanium at full scale wastewater treatment plants: implications for TiO2 nanomaterials, J. Environ. Monitor. 13 (2011) 1195-1203

[23] C. O. Hendren, X. Mesnard, J. Dröge, M. R. Wiesner, Estimating production data for five engineered nanomaterials as a basis for exposure assessment, Environ. Sci. Technol. 45 (2011) 2562-2569

[24] M. C. Roco, C. A. Mirkin, M. C. Hersam, Nanotechnology research directions for societal needs in 2020: summary of international study, J. Nanopart. Res. 13 (2011) 897-919

[25] Y. Liu, M. Tourbin, S. Lachaize, P. Guiraud, Nanoparticles in wastewaters: Hazards, fate and remediation, Powder Technol. 255 (2014) 149-156

[26] A. Elsaesser, C. V. Howard, Toxicology of nanoparticles, Adv. Drug Deliv. Rev. 64 (2012) 129-137

[27] W. H. De Jong, P. J. A. Borm, Drug delivery and nanoparticles: Applications and hazards, Int. J. Nanomedicine 3 (2008) 133-149

[28] S. Eduok, B. Martin, R. Villa, A. Nocker, B. Jefferson, F. Coulon, Evaluation of engineered nanoparticle toxic effect on wastewater microorganisms: Current status and challenges, Ecotoxicol. Environ. Saf. 95 (2013) 1-9

[29] P. Xu, G. M. Zeng, D. L. Huang, C. L. Feng, S. Hu, M. H. Zhao, et al., Use of iron oxide nanomaterials in wastewater treatment: A review, Sci. Total Environ. 424 (2012) 1-10

[30] M. Hua, S. Zhang, B. Pan, W. Zhang, L. Lv, Q. Zhang, Heavy metal removal from water/wastewater by nanosized metal oxides: A review, J. Hazard. Mater. 211–212 (2012) 317-331

[31] R. R. Rosenfeldt, F. Seitz, R. Schulz, M. Bundschuh, Heavy metal uptake and toxicity in the presence of titanium dioxide nanoparticles: A factorial approach using daphnia magna, Environ. Sci. Technol. 48 (2014) 6965-6972

[32] Y. Wang, P. Westerhoff, K. D. Hristovski, Fate and biological effects of silver, titanium dioxide, and C60 (fullerene) nanomaterials during simulated wastewater treatment processes, J. Hazard. Mat. 201–202 (2012) 16-22

[33] H. Hyung, J.-H. Kim, Dispersion of C60 in natural water and removal by conventional drinking water treatment processes, Water Research 43 (2009) 2463-2470

[34] M. R. Chang, D. J. Lee, J. Y. Lai, Nanoparticles in wastewater from a science-based industrial park—Coagulation using polyaluminum chloride, J. Environ. Manage. 85 (2007) 1009-1014

[35] A. D. Pomogailo, V. N. Kestelman, "Principles and mechanisms of nanoparticle stabilization by polymers," in Metallopolymer Nanocomposites. vol. 81, ed: Springer Berlin Heidelberg, 2005, pp. 65-113.

[36] P. Aimar, P. Bacchin, Slow colloidal aggregation and membrane fouling, J. Membr. Sci. 360 (2010) 70-76

[37] L. A. Thomas, L. Dekker, M. Kallumadil, P. Southern, M. Wilson, S. P. Nair, et al., Carboxylic acid-stabilised iron oxide nanoparticles for use in magnetic hyperthermia, J. Mater. Chem. 19 (2009) 6529-6535

[38] M. Günay, H. Erdemi, A. Baykal, H. Sözeri, M. S. Toprak, Triethylene glycol stabilized MnFe2O4 nanoparticle: Synthesis, magnetic and electrical characterization, Mater. Res. Bull. 48 (2013) 1057-1064

[39] M. Aslam, L. Fu, M. Su, K. Vijayamohanan, V. P. Dravid, Novel one-step synthesis of amine-stabilized aqueous colloidal gold nanoparticles, J. Mater. Chem. 14 (2004) 1795-1797

[40] V. L. Alexeev, P. Ilekti, J. Persello, J. Lambard, T. Gulik, B. Cabane, Dispersions of silica particles in surfactant phases, Langmuir 12 (1996) 2392-2401

[41] M. K. Corbierre, N. S. Cameron, R. B. Lennox, Polymer-stabilized gold nanoparticles with high grafting densities, Langmuir 20 (2004) 2867-2873

[42] A. Housni, M. Ahmed, S. Liu, R. Narain, Monodisperse protein stabilized gold nanoparticles via a simple photochemical process, J. Phys. Chem. C 112 (2008) 12282-12290

[43] H. Huang, X. Yang, Synthesis of polysaccharide-stabilized gold and silver nanoparticles: a green method, Carbohydr. Res. 339 (2004) 2627-2631

[44] R. I. Feigin, D. H. Napper, Depletion stabilization and depletion flocculation, J. Colloid Interface Sci. 75 (1980) 525-541

[45] G. J. Fleer, J. H. M. H. Scheutjens, B. Vincent, "The stability of dispersions of hard spherical particles in the presence of nonadsorbing polymer," in Polymer Adsorption and Dispersion Stability. vol. 240, ed: American Chemical Society, 1984, pp. 245-263.

[46] Y. Liu, M. Tourbin, S. Lachaize, P. Guiraud, Silica nanoparticles separation from water: Aggregation by cetyltrimethylammonium bromide (CTAB), Chemosphere 92 (2013) 681-687

[47] J. Zhang, J. Buffle, Kinetics of hematite aggregation by polyacrylicacid: Importance of charge neutralization, J. Colloid Interface Sci. 174 (1995) 500-509

[48] M. Baalousha, A. Manciulea, S. Cumberland, K. Kendall, J. R. Lead, Aggregation and surface properties of iron oxide nanoparticles: Influence of ph and natural organic matter, Environ. Toxicol. Chem. 27 (2008) 1875-1882

[49] K. Mühle, Particle adhesion in coagulation and bridging flocculation, Colloid Polym. Sci. 263 (1985) 660-672

[50] S. Ji, J. Y. Walz, Depletion flocculation induced by synergistic effects of nanoparticles and polymers, J. Phys. Chem. B 117 (2013) 16602-16609

[51] J. Shao, J. Hou, H. Song, Comparison of humic acid rejection and flux decline during filtration with negatively charged and uncharged ultrafiltration membranes, Water Research 45 (2011) 473-482

[52] M. Hashino, K. Hirami, T. Ishigami, Y. Ohmukai, T. Maruyama, N. Kubota, et al., Effect of kinds of membrane materials on membrane fouling with BSA, J. Membr. Sci. 384 (2011) 157-165

[53] W. J. C. van de Ven, K. v. t. Sant, I. G. M. Pünt, A. Zwijnenburg, A. J. B. Kemperman, W. G. J. van der Meer, et al., Hollow fiber dead-end ultrafiltration: Influence of ionic environment on filtration of alginates, J. Membr. Sci. 308 (2008) 218-229

[54] A. Grenier, M. Meireles, P. Aimar, P. Carvin, Analysing flux decline in dead-end filtration, Chem. Eng. Res. Des. 86 (2008) 1281-1293

[55] F. Wang, V. V. Tarabara, Pore blocking mechanisms during early stages of membrane fouling by colloids, J. Colloid Interface Sci. 328 (2008) 464-469

[56] P. Bacchin, P. Aimar, R. W. Field, Critical and sustainable fluxes: Theory, experiments and applications, J. Membr. Sci. 281 (2006) 42-69

[57] M. Mulder, Basic principles of membrane technology. Dordrecht; Boston: Kluwer Academic, 2003.

[58] C. Henry, J.-P. Minier, G. Lefèvre, Towards a description of particulate fouling: From single particle deposition to clogging, Adv. Colloid Interface Sci. 185–186 (2012) 34-76

[59] G. Belfort, R. H. Davis, A. L. Zydney, The behavior of suspensions and macromolecular solutions in crossflow microfiltration, J. Membr. Sci. 96 (1994) 1-58

[60] P. Harmant, P. Aimar, Coagulation of colloids retained by porous wall, AIChE J. 42 (1996) 3523-3532

[61] P. Bacchin, D. Si-Hassen, V. Starov, M. J. Clifton, P. Aimar, A unifying model for concentration polarization, gel-layer formation and particle deposition in cross-flow membrane filtration of colloidal suspensions, Chem. Eng.Sci. 57 (2002) 77-91

[62] M. R. Ivanov, H. R. Bednar, A. J. Haes, Investigations of the mechanism of gold nanoparticle stability and surface functionalization in capillary electrophoresis, ACS Nano 3 (2009) 386-394

[63] P. Harmant, P. Aimar, Coagulation of colloids in a boundary layer during cross-flow filtration, Colloids Surf., A 138 (1998) 217-230

[64] Y. Bessiere, N. Abidine, P. Bacchin, Low fouling conditions in dead-end filtration: Evidence for a critical filtered volume and interpretation using critical osmotic pressure, J. Membr. Sci. 264 (2005) 37-47

CHAPTER 2

Dead-end microfiltration of electrostatically stabilized nanoparticles – role of electrostatic interactions

This chapter has been published as:
Krzysztof W. Trzaskus, Wiebe M. de Vos, Antoine Kemperman, and Kitty Nijmeijer
Towards controlled fouling and rejection in dead-end microfiltration of nanoparticles – Role of electrostatic interactions.
Journal of Membrane Science, 496 (2015) 174–184

Abstract

Membrane technology proves to be effective in the removal of nano-sized contaminants from water. However, not much is known on the filtration and fouling behavior of manufactured nanoparticles.

The high surface-area-to-volume ratio of nanoparticles, significantly increases the effect of surface interactions on the stability of nanoparticle suspensions. Also, the stability of nanoparticle suspensions and their tendency to aggregate strongly affects the fouling mechanism during membrane filtration of nanoparticles. In this experimental study, fouling development and rejection mechanisms of model mono-disperse silica nanoparticles were investigated in great detail.

A microfiltration hollow fiber membrane was employed in dead-end filtration mode for the filtration of commercially available silica nanoparticles under constant pressure. By applying a low concentration of nanoparticles and a large difference between the membrane pore size (~200 nm) and the nominal size of the nanoparticles (22 nm), a detailed investigation of the fouling mechanisms was allowed. Five subsequent fouling stages were postulated: adsorption, unrestricted transport through pores, pore blocking, cake filtration and cake maturation. Higher concentrations of nanoparticles did not change the behavior of these fouling stages, but were found to lead to their acceleration. Fouling severity and occurrence of dynamic transitions between these fouling stages were quantitatively evaluated. The presence of salts, pH and valency of the cation strongly influenced nanoparticle properties and interactions and thus occurrence and character of the fouling stages. Lower repulsive interactions between the nanoparticles accelerate fouling by faster pore blockage and aggregation on the membrane surface. Porosity and permeability of the formed filtration cake layer are strongly dependent on the repulsive interactions between nanoparticles, with a lower repulsion leading to denser cake layers. This chapter clearly shows that fouling development and rejection of nanoparticles by microfiltration membranes easily can be adjusted by tuning the electrostatic interactions between the suspended nanoparticles.

2.1. Introduction

Over the recent decades, the unique properties of nanomaterials have led to an exponential growth in the development of nanotechnology and a rapid expansion of the nanotechnology industry. Of all nanomaterials, engineered nanoparticles are the most recognized and they are produced in the largest quantities. Today, nanoparticles can be found as additives in many common products such as cosmetics, paints and cleaning agents [1]. However, this increase in interest and possible applications of engineered nanoparticles will contribute to an increasing discharge of nanoparticles into aquatic systems with associated health and environmental consequences. Thus, effective methods for nanoparticle removal have to be developed. One of the most promising and reliable techniques in water purification is membrane technology, which has already proven to be effective in the removal of colloidal particles such as proteins, natural organic matter and inorganic particles (e.g. [2-5]).

However, not much is known about membrane filtration and the dynamics of fouling by engineered nanoparticles. Especially, the small size of nanoparticles makes their behavior different as it results in a high surface-area-to-volume ratio, which significantly increases the role of the surface interactions during membrane filtration. As a consequence, membrane filtration of nanoparticles will be not only driven by simple size exclusion of the membrane. Also other retention mechanisms such as adsorption, electrostatic repulsion or steric effects will play more dominant role in the separation of these engineered nanoparticles.

Membrane fouling has been intensively investigated over recent years in numerous studies and the factors responsible for fouling severity have been well defined [6]. Generally speaking, membrane fouling starts with foulant-membrane interactions, which cause an initial adsorption of a fouling layer. Then, while the initial foulant layer covers the membrane surface, the next fouling step is driven by foulant-foulant interactions. Further fouling development is promoted or diminished depending on whether the foulant-foulant interactions are more attractive or more repulsive in character, respectively. The electrostatic blocking effect, first reported by Vincent et al. [7] and later by Adamczyk et al. [8], is an example of repulsive interactions, which are caused by double-layer electrostatic repulsion between particles. Once a particle is already adsorbed on the surface, repulsive particle-particle interactions prevent further deposition near a previously settled particle. Therefore, in the case of membrane fouling and if the repulsive energy barrier is high enough, no further aggregation on the surface is possible and fouling can be suppressed. On the other hand, if the repulsion forces between the

particles are weak and can be overcome by a relative increase in kinetic energy by fluid motion towards the membrane, aggregation on the surface is facilitated and multilayer deposition can be promoted [9, 10]. This aggregation contributes to the formation of a thick fouling layer on top of the membrane or inside the porous membrane structure.
Porous membranes, especially ultra- and microfiltration, which can be applied for the removal or fractionation of engineered nanoparticles [11-16], are prone to fouling by particles smaller than the membrane pore size. In that case, pore blockage is the result of pore constriction and/or pore diameter narrowing at the membrane surface and inside the porous membrane structure [17-20]. This reduction in pore size of the membrane causes a change in the performance of the membrane in terms of rejection and filtration resistance.

According to the DLVO (Derjaguin-Landau-Verwey-Overbeek) theory and in line with many experimental studies, the stability of the nanoparticle significantly influences the filtration process [21-23]. During membrane filtration, the concentration of nanoparticles at the membrane surface increases depending on the flux during filtration and the level of nanoparticle rejection. For very stable colloidal suspensions, this local increase in nanoparticle concentration does not promote aggregation since particle stability is not very sensitive to concentration changes. Furthermore, a deposit formed by such a stable nanoparticle suspension would remain porous and easily permeable for water. However, for less stable nanoparticle suspensions, an increase in the nanoparticle concentration on the membrane surface can most likely result in local-near membrane surface clustering and aggregation of nanoparticles [24]. This lower nanoparticle stability promotes faster pore blockage, followed by the formation of a denser and less permeable cake layer. Therefore, to estimate the role of nanoparticle stability in a dynamically changing filtration process, it is essential to investigate the kinetics of fouling development and impact of surface interactions on each of the considered fouling stages. However, most of the studies on particle fouling of porous membranes ignore the dynamic character of the membrane fouling and focus on the dominant fouling mechanism [25, 26].

This chapter encompasses a detailed investigation into the dynamic development of membrane fouling and rejection of a series of silica nanoparticles, which are representative for a large group of electrostatically stabilized nanoparticles. Alteration of the nanoparticle stability by a change in pH, salt concentration or salt type enabled adjustment of the fouling evolution and nanoparticle rejection during the course of filtration. Large differences between membrane pore size and the diameter of the

nanoparticles allowed a detailed study of the different fouling stages that could occur during dead-end microfiltration of nanoparticles. The inclusion of the initial fouling stages is especially important as nanoparticles are typically present in very low concentrations where a slow evolution of fouling stages is expected. The impact of the nanoparticle stability on each fouling stage was analyzed quantitatively using available theory and experimental data. According to our knowledge, up to date, such a detailed and systematical study on fouling kinetics during dead-end microfiltration of electrostatically stabilized nanoparticles has not yet been reported.

2.2. Theory

Characteristic fouling stages and the transition points between them can be quantitatively evaluated by a detailed investigation of the obtained resistance vs. permeate volume (*R* vs. *V)* curves, combined with the classical filtration laws [27] described by the *dR/dV* vs. *R* relationship [28, 29] as:

$$\frac{dR}{dV} = k \cdot R^n \qquad (1)$$

where *R* is the filtration resistance (1/m), *V* is the volume of the permeate (m^3) and *n* is a dimensionless exponential factor representative for the specific fouling model for (a) complete blocking (*n* = 2), (b) standard blocking (*n* = 1.5), (c) intermediate blocking (*n* = 1) or (d) cake filtration (*n* = 0). This model and definition of fouling stages recently were applied by Xiao et al. to describe fouling evolution and gel layer growth during constant pressure stirred dead-end filtration [28, 29]. Fig. 1 schematically shows the fouling development (a) during constant pressure dead-end microfiltration and respective *dR/dV* vs. *R* curve (b).

For the possible occurrence of fouling, the foulant firstly always is adsorbed onto the membrane surface (stage 1 in Fig. 1) [10]. Due to membrane pore narrowing upon adsorption, this initial fouling step can lead to an increase of the filtration resistance. Consequently, the exponential factor *n* has a positive value. For systems where the membrane pore size is sufficiently larger than the nanoparticle size, pore narrowing does not reduce the pore size sufficiently to block the pore completely, and nanoparticles can still be transported through the pores. Therefore, in the second fouling stage (2), pore blockage does not occur, the resistance develops significantly slower and the exponential

factor n has a negative value ($n < 0$). The demarcation point between the adsorption stage and transport stage is referred to as the equilibrium point.

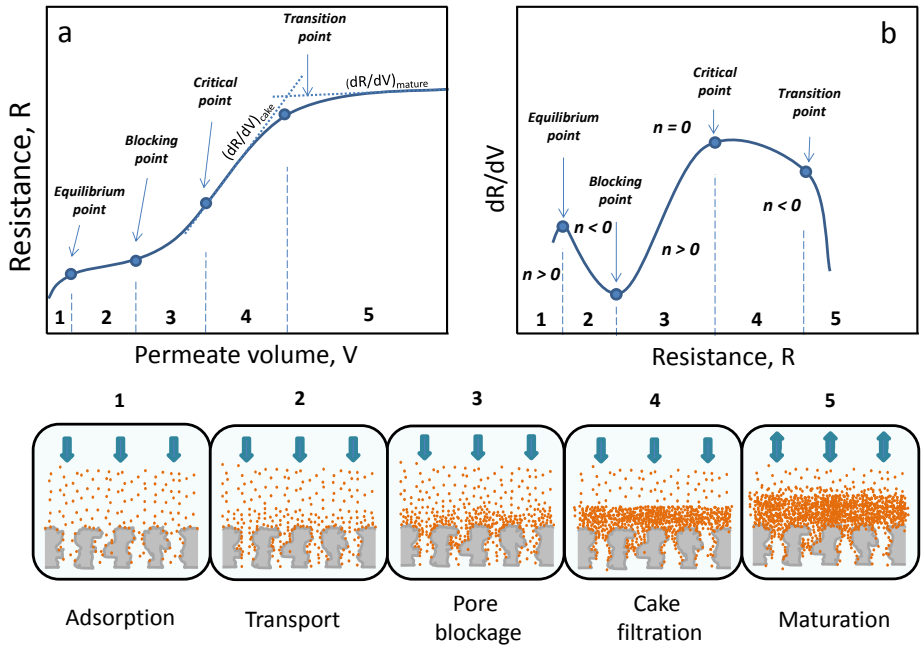

Fig. 1. Idealized fouling development scheme for dead-end microfiltration of silica nanoparticles. (a) Resistance as a function of the permeate volume; (b) dR/dV vs R curve and characteristic points indicating shift between fouling stages. Model extended from [28].

Subsequently, when pore blockage (stage 3 in Fig. 1) starts, a significant reduction of the pore sizes occurs and a drastic increase of the resistance is visible. The exponential factor n rises again to positive values ($n > 0$). The point at which the exponent n changes its sign to a positive value is referred to as the blocking point – the point at which pore blocking starts. As a natural continuity of pore blockage, cake filtration (stage 4 in Fig. 1) takes place. According to the classical filtration laws [27], in a pure cake filtration stage the resistance rises linearly with permeate volume, and hence in this stage the exponential factor n is equal to 0. The starting point of stage 4 – the critical point – is the most accurately described by a cake filtration model and is referred to as a demarcation point between pore blockage and cake filtration. The resistance increase rate around the critical point $(dR/dV)_{cake}$ normalized to the feed solution concentration is known as the specific cake resistance α. The higher the specific cake resistance, the more compact the

cake structure. In constant pressure filtration, a reduced permeate flux caused by the development of a cake layer may lead to maturation of the cake (stage 5 in Fig. 1). In that case, a decreasing permeate flux leads to a reduction of the drag force of particles towards the membrane surface, which at a certain point becomes equal to the back transport of the nanoparticles due to diffusion or/and the strong electrostatic repulsions between the nanoparticles. At this stage, filtration is carried out at a steady-state flux, which is equivalent to the critical flux in cross-flow filtration [28, 30]. As a consequence, the cake layer growth is reduced, the resistance develops slower and a negative value of exponent n is obtained. For infinitely long filtration times, resistance approaches asymptotically a stable value and the exponent n is infinitely negative. The transition point – the established point between the cake filtration stage and the maturation stage – we defined as the intersection point of the tangents describing the fouling development in the cake filtration stage and the fully developed maturation stage (see Fig. 1a). In order to quantitatively describe fouling development in the maturation stage, the resistance increase rate in the maturation stage $(dR/dV)_{mature}$ is calculated. The lower the $(dR/dV)_{mature}$ value is, the closer it is to the plateau indicating filtration under steady-state flux [30].

In this study, in order to quantitatively and in great details describe fouling development in microfiltration of electrostatically stabilized nanoparticles, characteristic points were calculated. The equilibrium point, blocking point and critical point were calculated by investigation of the exponent n change in sign. Transition point was estimated as a intersection point of the tangents describing the resistance increase in the cake filtration stage and maturation stage.

2.3. Experimental

2.3.1. Materials

Commercially available colloidal silica Ludox TM-50 . supplied in the form of aqueous suspensions containing 50% silica nanoparticles (Sigma Aldrich) were used as model silica nanoparticles. All solutions were prepared using ultrapure water (Milli-Q, >18.2 MOhm). ACS grade NaCl, HCl, NaOH, KCl and $CaCl_2$ were purchased from Sigma Aldrich and used in aqueous solutions in order to adjust the pH and ionic strength of the nanoparticle solutions. All chemicals were used without further purification.

2.3.2. Membrane and membrane characterization

The membranes used in the experiments were commercially available inside-out PES-PVP microfiltration (MF) membranes (Pentair X-Flow 1.5MF02) supplied by Pentair X-Flow BV (The Netherlands). To prepare a filtration module, one MF-hollow fiber membrane (length 53 mm and inner diameter 1.5 mm) was potted in a PVC tube (outer diameter 8 mm) with two-component polyurethane glue 2K Expert (Bison International B.V., The Netherlands) to give a final filtration area of 2.5 cm^2. The membrane was characterized in terms of pure water permeability, scanning electron microscopy analysis (SEM), inner surface charge, and pore size distribution. For SEM analysis, small pieces of both the dry native membrane and the fouled membrane were sputtered with a thin platinum layer using a Jeol JFC-1300 fine coater. The SEM images were taken using a high-resolution SEM microscope (Jeol JSM-6000F). The pore size distribution of the membrane was measured using the capillary flow porometry (CFP) technique. The measurements were conducted using a Porolux™ 1000 device (POROMETER NV) and Porefil Wetting Fluid (supplied by POROMETER NV) was used as pore-filling liquid. The zeta potential of the inner surface of the membrane was measured using a SurPASS electrokinetic analyzer (Anton Paar GmbH). A module for the zeta potential measurements was prepared by potting a single hollow fiber in 8 mm PE tube by filling the tube completely with two component epoxy resin. The streaming potential of the inner surface of the membrane was evaluated by flushing 5 mM KCl through the fiber lumen. The pH was adjusted using aqueous 0.1 M NaOH and 0.1 M HCl solutions. The zeta potential was calculated according to the Fairbrother-Mastin equation.

2.3.3. Permeation setup

All filtration experiments were performed in dead-end filtration mode using the setup shown schematically in Fig. 2. Pressurized nitrogen was connected to two vessels and the outlets of both vessels were connected to the single fiber filtration module. Before filtration of the nanoparticle solution, 50 mL of ultrapure water was filtered through the membrane to obtain a stable pure water flux. Due to the potting procedure, small difference in membrane surface area between individual modules were obtained, hence pure water fluxes varied to a small extent. Only the modules with about uniform pure water fluxes were chosen for further filtration with silica nanoparticles. A deviation of about 10% from the average pure water permeability was accepted. In the second step,

after determination of the ultrapure water flux, the nanoparticle solution vessel was connected to the membrane by opening the valve. This procedure and setup design enabled us to observe adsorption phenomenon already from the beginning of the filtration process. Permeate was collected during the experiment and the mass increase over time was monitored continuously by an analytical balance connected to a computer. Permeability was calculated according to Eq. 2:

$$L_P = \frac{J}{\Delta P} \tag{2}$$

Where L_P is the liquid permeability (L/m^2·h·bar), J is the flux (L/m^2·h) and ΔP is the transmembrane pressure (bar). Every 50 mL of permeate was collected for ICP-MS analysis. Rejection of the silica nanoparticles was calculated according to Eq. 3:

$$\sigma = 1 - \frac{C_P}{C_f} \tag{3}$$

where σ is the rejection (-), C_P is the concentration of the nanoparticles in the permeate sample (mg/L), C_f is the concentration of the nanoparticles in the feed solution (mg/L). The experiments were stopped when 400 mL of nanoparticle solution was filtered. All the experiments were performed at a transmembrane pressure of 0.20 ± 0.02 bar at a temperature of 22 ± 1°C. Each set of experiments was repeated three times and the filtration curves achieved were averaged.

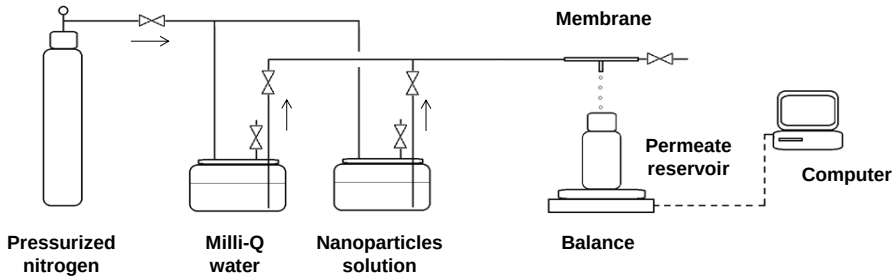

Fig. 2. Flow sheet of the experimental constant pressure filtration setup.

2.3.4. Filtration experiment

To investigate the influence of the nanoparticle concentration on the fouling behavior, Milli-Q water solutions containing 1 mM NaCl and 1 mg/L to 10 mg/L of silica nanoparticles were prepared at pH 8. The role of the stability of the nanoparticle solution on the fouling mechanism was studied using feed solutions with the same nanoparticle concentration (2 mg/L of silica nanoparticles) but higher ionic strength or lower pH. The influence of the valency of the cation of the salt on the fouling behavior of the silica nanoparticles was evaluated using $CaCl_2$. Philips CM300ST-FEG Transmission Electron Microscope (TEM) was used to image the silica nanoparticles, and their size distribution was determined from TEM images using ImageJ 1.48v software (National Institute of Health). Hydrodynamic diameter and surface zeta potential of the nanoparticles were measured by dynamic light scattering (DLS) and electrophoretic mobility measurements using a Malvern ZetaSizer 3000HSa. The measurements were conducted using approx. 0.5 g/L nanoparticle solutions prepared by dilution of commercial suspensions in ultrapure water. The nanoparticle concentration in the feed and permeate solutions was measured by ICP-MS (Thermo Fisher Xseries 2), by evaluating the total silicon content. The detection limit of Si by the applied ICP-MS technique was 0.05 mg/L, which is more or less equivalent to 0.01 mg/L SiO_2. Thus, using 2 mg/L of SiO_2 in the feed solution, the maximum measurable rejection could not be higher than 95%.

4. Results and discussion

4.1. Membrane and particles characterization

The pore size distribution of the investigated microfiltration (MF) PES-PVP membrane is presented in Fig. 3a. The capillary flow porometry (CFP) measurements show that the pore diameters vary between 160 and 240 nm, while the mean pore diameter is found to be 200 nm. The SEM images in Fig. 3c and Fig. 3d reveal that the pores are far from cylindrical in shape: they are tortuous, their diameter is broadly distributed and difficult to define. The membrane has a highly asymmetric structure (Fig. 3d) with a selective layer of several hundreds of nanometers thick at the inside of the fiber. As a consequence, pore blockage phenomena will take place only at this thin and selective interface or at the surface of the membrane. The zeta potential of the inner membrane surface as a function of the pH is shown in Fig. 3b. The inner membrane

surface has its isoelectric point at pH 4.3. The clean water permeability of the membrane is in the range of $11 \cdot 10^3$-$12 \cdot 10^3$ L/m^2·h·bar.

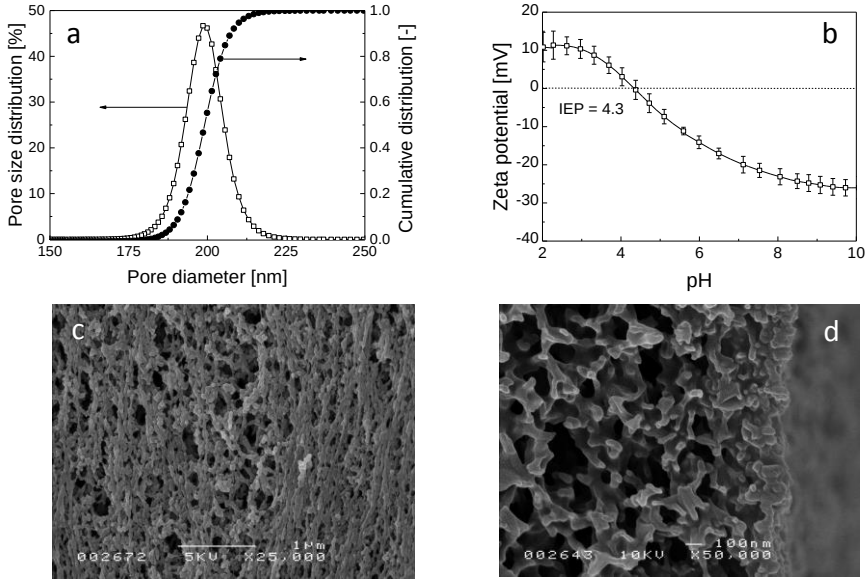

Fig. 3. (a) Pore size distribution of the investigated MF membrane according to capillary flow porometry (CFP) measurements; (b) Zeta potential as a function of pH at the inner surface of the investigated MF membrane; SEM images of the applied native MF membrane (c) inner surface and (d) cross-section of the native membrane.

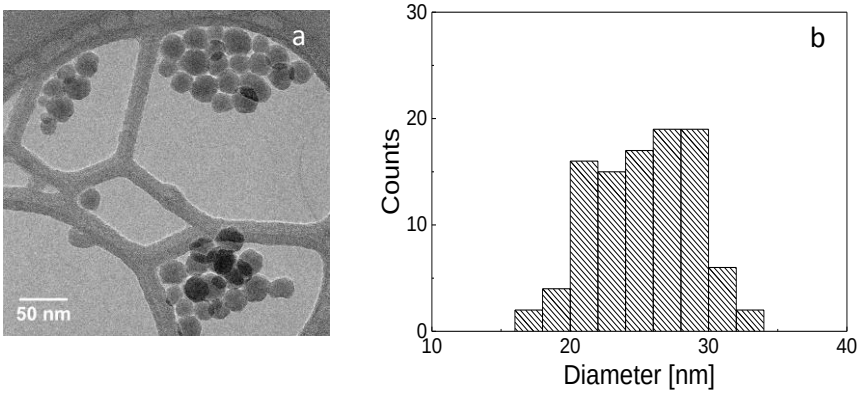

Fig. 4. (a) TEM image of silica nanoparticles Ludox TM-50 and (b) size distribution obtained from TEM image analysis

As shown in Fig. 4, silica nanoparticles were analyzed by TEM microscopy. The size of the nanoparticles varied between 17 and 34 nm. The mean diameter of the nanoparticles was estimated as 25.5 ± 5.2 nm, which is slightly larger than the value given by manufacturer (22 nm). The difference between pore size of the membrane (see Fig. 3) and nanoparticle diameter is about a factor 8.

Correspondingly, the zeta potential and Z-average diameter of the silica nanoparticles used in this study as a function of pH are presented in Fig. 5.Over the whole pH range measured, the silica nanoparticles are negatively charged. With increasing pH, the nanoparticle surface becomes strongly charged as reflected in the more negative zeta potential, which is due to deprotonation of the silanol groups on the surface of the nanoparticles [21]. The Z-average diameter as calculated from DLS measurements – representing an average hydrodynamic diameter of the nanoparticles – varies from about 23 nm to 33 nm (Fig. 4). The hydrodynamic diameter of the silica nanoparticles increases in line with the decrease of the zeta potential. The increasing Z-average size with increasing pH is quite surprising, and we attribute it to artifacts of the DLS measurements caused by compaction of electrical double layer when HCl is added during pH adjustment.

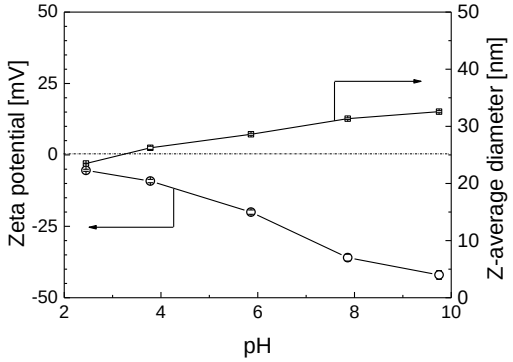

Fig. 5. Zeta potential and Z-average diameter of Ludox TM-50 silica nanoparticles as a function of pH.

2.4.2. Filtration experiments

2.4.2.1. Influence of nanoparticle concentration

Due to a high surface-area-to-volume ratio of nanoparticles, thus more pronounced role of surface interactions, rejection and fouling development during nanoparticle microfiltration is not only driven by a simple size exclusion but also by surface interactions. For electrostatically stabilized nanoparticles, interactions between nanoparticles and between membrane and nanoparticles can significantly influence rejection and fouling.

The influence of nanoparticle concentration on the fouling behavior during membrane filtration at pH 8 was investigated. The permeability and rejection as a function of the specific permeate volume for various nanoparticle concentrations are shown in Fig. 6a and Fig. 6b, respectively. As expected, fouling develops faster and is more pronounced at higher nanoparticle concentrations. In order to quantitatively describe fouling evolution and shifts between the different fouling stages, the characteristic parameters as discussed in Fig. 1 were calculated and are summarized in Table 1.

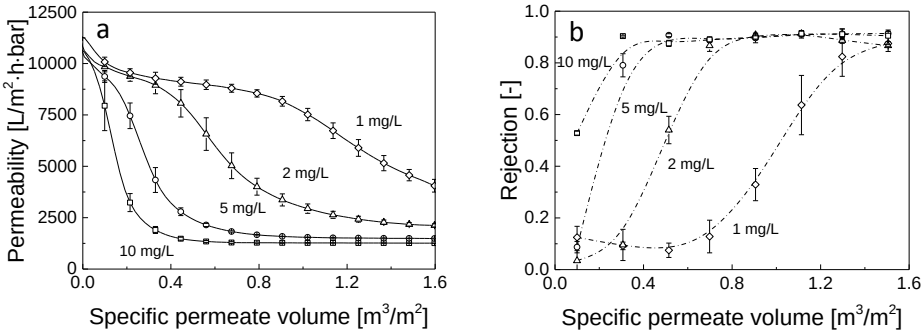

Fig. 6. (a) Permeability and (b) rejection as a function of specific permeate volume for various concentrations of Ludox TM-50 silica nanoparticles during dead-end microfiltration at pH 8.

As shown in Fig. 6a, when using 1 mg/L of nanoparticles directly at the beginning of the filtration process, the permeability reduces to approximately 90% of the initial permeability value. Subsequently, it stabilizes and finally declines again at the end of the filtration. This first and immediate decrease of the permeability occurs for all applied concentrations and can be explained by blockage of the smallest pores due to surface adsorption or concentration polarization, which occurs directly after introduction of the nanoparticles to the membrane module. Fig. 6b confirms the occurrence of an additional

rejection mechanism (adsorption) at the very beginning of the filtration process. It shows a slightly higher rejection for silica nanoparticles (1 mg/L) in the first measured permeate sample than in the following two samples. However, this initially higher rejection is not observed during filtration of solutions containing higher concentrations of silica nanoparticles (apart from 10 mg/L but this is due to different a mechanism, as at this concentration the membrane is immediately blocked). Probably, due to the low adsorptive capacity of the membrane surface or the low surface area available, only a small number of nanoparticles can be adsorbed or entrapped inside the membrane structure. At higher concentrations, this amount of adsorbed nanoparticles, in comparison to the total number of nanoparticles in the feed solution, is negligible and no improvement in terms of the rejection is observed. Adsorption is possible by the formation of hydrogen bonds between the PVP molecules in the membrane structure and the silica nanoparticles [31]. Secondly, the tortuosity of the pores may facilitate entrapment of the nanoparticles, which consequently results in a lower permeability.

For the 1 mg/L feed solution, for the immediate entrapment of the nanoparticle on the membrane surface and the initial decrease in permeability, the permeability becomes more stable (Fig. 6a). The same stabilization of the permeability occurs for 2 mg/L and, less pronounced, for 5 mg/L. Since in this stage fouling development slows down, the exponential factor *n* has a negative value (see Equation 1). The point at which the sign of the exponential factor *n* shifts from a negative (in the adsorption stage) to a positive (in the transport stage) value is referred to as the equilibrium point. At this point, the second filtration stage (see Fig. 1) – nanoparticle transport across the membrane – is initiated. Furthermore, the rejection of nanoparticles at this stage is only about 10% (Fig. 6b) suggesting transport of nanoparticles through the open membrane pores. Similar fouling behavior with an initially stable flux and low fouling was observed e.g. by Tracey et al. [32] and by Xiao et al. [28] during protein microfiltration. The large difference between the pore size of the membrane and the nanoparticle diameter allows transport of nanoparticles without rejection. Moreover, electrostatic repulsion induced by the negative surface charges of the membrane (Fig. 3b) and the negatively charged nanoparticles (Fig. 5) – and the even stronger electrostatic repulsion between already adsorbed nanoparticles and freshly transported nanoparticles from the bulk – further reduces particle deposition on the surface and inside the pores. As a result, clogging of the pores inside the membrane structure is not observed and nanoparticle rejection stays low while permeability is relatively constant.

However, after longer filtration time a second decrease in permeability is observed (Fig. 6a). The point at which permeability starts to reduce significantly faster and as a result the exponential factor *n* changes its sign to positive we marked as the blocking point (see Fig. 1). The corresponding rejection data in Fig. 6b show that from this point on, rejection increases from about 10% up to about 90%. The sudden fouling acceleration can have several reasons, such as cake compaction [33, 34], aggregation of nanoparticles due to concentration polarization [35] or pore blockage [28]. Firstly, a low rejection of the nanoparticles (see Fig. 6b) before the blocking point excludes cake compaction as cause. Cake compaction needs to be preceded by a cake filtration stage, which would definitely contribute to a higher nanoparticle rejection, and this is not the case here. Secondly, internal pore blockage is limited by an asymmetric structure of the membrane used (see Fig. 3d). Therefore, pore blockage can only occur in the very thin and selective top layer of the membrane. Thirdly, due to the difference between membrane pore size (Fig. 3a) and nanoparticle diameter (Fig. 4), pore blocking due to pore constriction is rather unlikely. However, such self-accelerating fouling development was theoretically predicted by Wessling [36] and later by Chen and Kim [17] for a dead-end filtration of the solute much smaller than the membrane pores. They showed that membrane pores can be clogged by deposition of nanoparticles on the membrane surface and subsequent pore closure by formation of a nanoparticle deposit, which will act as a secondary and dynamic membrane enhancing rejection. Therefore, we suggest external nanoparticle deposition followed by pore closure as the most probable for the fouling acceleration after transport stage of nanoparticles.

As summarized in Table 1, the specific permeate volume needed to reach the blocking point (V_{block}) is inversely proportional to the concentration of the nanoparticles in the feed solution. In other words, by increasing the concentration of nanoparticles, the blocking point was reached faster but always the same total amount of nanoparticles was transported towards the membrane surface before pore blockage was initiated. Therefore, if the interactions between nanoparticles in various feed solutions are the same but the concentration of nanoparticles varies widely, we can always expect the same fouling evolution of nanoparticles, which will be only a function of the number of nanoparticles.

Table 1. Characteristic parameters describing fouling development during dead-end microfiltration for various concentrations of Ludox TM-50 silica nanoparticle suspension at pH 8. V_{eq}, V_{block}, V_{crit} and V_{mat} are specific permeate volume at the equilibrium point, blocking point, critical point and transition point, respectively; R_{eq}, R_{block}, R_{crit} and R_{mat} are the resistance at the equilibrium point, blocking point, critical point and transition point, respectively; α is specific cake resistance; $(dR/dV)_{mat}$ is resistance development in maturation stage; na (not available due to too slow or too fast fouling development).

Nanoparticle concentration [mg/L]		**1**	**2**	**5**	**10**
Equilibrium point	V_{eq} **[m^3/m^2]**	0.05±0.01	0.04±0.01	na	na
	R_{eq} **[10^{10} 1/m]**	3.3±0.1	3.4±0.1	na	na
Blocking point	V_{block} **[m^3/m^2]**	0.48±0.06	0.23±0.02	0.10±0.01	na
	R_{block} **[10^{10} 1/m]**	4.0±0.1	3.9±0.1	3.8±0.1	na
Critical point	V_{crit} **[m^3/m^2]**	1.45±0.08	0.65±0.02	0.33±0.02	0.21±0.02
	R_{crit} **[10^{10} 1/m]**	7.2±0.2	7.5±0.4	8.8±0.3	11.2±0.2
	α **[10^{13} m/kg]**	7.2±0.4	7.2±0.2	7.1±0.3	7.0±0.1
Transition point	V_{mat} **[m^3/m^2]**	na	1.22±0.01	0.70±0.03	0.43±0.02
	R_{mat} **[10^{10} 1/m^2]**	na	14.6±0.7	19.3±0.1	24.7±0.8
	$(dR/dV)_{mat}$ **[10^{10} 1/m^2]**	na	5.2±0.8	2.8±0.1	1.0±0.1

The fourth stage of the silica nanoparticle filtration process can be attributed to cake filtration (Fig. 1, stage 4) as the logical continuation of complete blockage of the pores. The calculated critical points (listed in the Table 1) quantify the transition between the pore blockage stage and the cake filtration stage. Likewise to the blocking point, the critical point is reached faster when higher nanoparticle concentrations are applied. Also for this critical point, the specific permeate volume at the critical point (V_{crit}) is inversely proportional to the nanoparticle concentration (see Table 1). Moreover, the filtration resistance at the end of the pore blockage stage – the critical point – rises with nanoparticle concentration in the feed solution, suggesting not only faster but also more severe pore blockage at higher nanoparticle concentrations. This behavior, where the magnitude of pore blockage increases with concentration, can be explained by a faster nanoparticle aggregation rate near the membrane surface.

The fouling evolution in the cake filtration stage is described by the cake specific resistance α, which is the same for all investigated concentrations (see Table 1). An

equal specific cake resistance indicates equal packing density of the filtration cake. Due to identical electrostatic interactions between nanoparticles and the same acting drag force (same size of nanoparticles, same applied pressure), the separation distance between nanoparticles in the filtration cake formed is constant. This is visualized in Fig. 7 that the resistance and rejection increase as a function of the particle load. The data of all concentrations coincide and the steepest slope of the resistance increase is defined as the specific cake resistance. From the beginning of this filtration stage, the observed rejection of nanoparticles is constant and equals about 90%. Lower nanoparticle rejection than 100% is commonly observed in membrane technology and mostly originates from the polydispersity of the membrane pores [37].

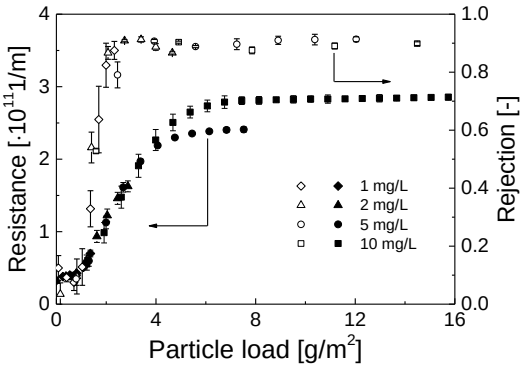

Fig. 7. Filtration resistances and rejection as a function of particle load for various feed concentrations of Ludox TM-50 silica nanoparticles during dead-end filtration at pH 8.

An arbitrarily defined transition point initiates the last stage, the maturation stage (stage 5, Fig. 1). The transition point is defined as the point at which the slope of the resistance development in the cake filtration stage crosses the tangent of the asymptotical resistance development in the maturation stage (see Fig. 1). At this last stage, the permeability stabilizes (Fig. 6a) and rejection is still maintained at about 90% (Fig. 6b). Aimar et al. [24] attributed this flux stabilization to the filtration under critical flux. At this flux, back transport of nanoparticles due to diffusion and electrostatic repulsion between nanoparticles is equal to convective transport towards the membrane surface. For a stable nanoparticle suspension, at this flux, near membrane surface aggregation of nanoparticles is terminated and freshly deposited nanoparticles only form concentration polarization layer on top of the filtration cake. Since the filtration resistance comes mainly from the layer of aggregated nanoparticles (forming a compact filtration cake),

further transport of the nanoparticles towards the membrane surface (occurring without nanoparticle aggregation), does not result in higher resistances (Fig. 7). As before, the final filtration stage was achieved faster at higher nanoparticle concentrations (Table 1) and is inversely proportional to the nanoparticle concentration. However, as shown in Fig. 7, by applying a higher nanoparticle concentration, a higher particle load is needed to complete the cake filtration stage and initiate the maturation stage at which the resistance stabilizes. As a result, the resistance at the transition point is also higher at higher nanoparticle concentrations (Table 1). It is well known that with higher solute concentrations in the feed, the critical flux is lower. Consequently, for higher feed concentrations, in order to reach lower critical flux value, thicker cake layers need to be formed thus increasing the filtration resistance. For higher nanoparticle concentrations, the reduced convective transport of the nanoparticles towards the membrane surface will also contribute to a slower fouling development in the maturation stage. This is quantitatively described by $(dR/dV)_{mat}$ in Table 1. For higher nanoparticle concentrations, $(dR/dV)_{mat}$ is lower, which can be attributed to the lower drag force in the maturation stage or to a not fully developed maturation stage (e.g. at 2 mg/L).

2.4.2.2. Influence of the feed pH

The effect of the feed solution pH on the filtration behavior of silica nanoparticles is shown in Fig 8. As expected, at lower pH of the feed solution, permeability decreases faster (Fig. 8a). A lower pH increases the degree of protonation of the silanol groups that are present on the surface of the silica nanoparticles. As a result, the zeta potential of the silica nanoparticles becomes less negative with lower pH, as was shown in Fig. 4. A less negative zeta potential reduces the repulsive interaction energy between the nanoparticles leading to a lower stability of the suspension. Furthermore, a lower pH also reduces the surface charge of the membrane (Fig. 3b) thereby diminishing the repulsive interactions between the membrane and the transported nanoparticles. This reduced electrostatic repulsion significantly affects the shape of the filtration curve, as is visible in Fig. 8a. All characteristic points (equilibrium point, blocking point, critical point and transition point) occur earlier when a lower pH is applied (compare Table 2 to Table 1.). A shorter transport stage and an earlier initiation of pore blockage at lower pH is caused by lower repulsive interactions between membrane and nanoparticles. On the other hand, due to lower repulsive interactions between nanoparticles, their aggregation rate can be enhanced, promoting faster pore blockage. As a consequence of more rapid pore

blockage, cake filtration establishes faster when pH is lower. In this stage, an increase of the cake specific resistance α with reduction of the pH (see Table 3) suggests a lower porosity of the filtration cake, which can be easily explained from the reduced repulsive interactions between the nanoparticles at lower pH.

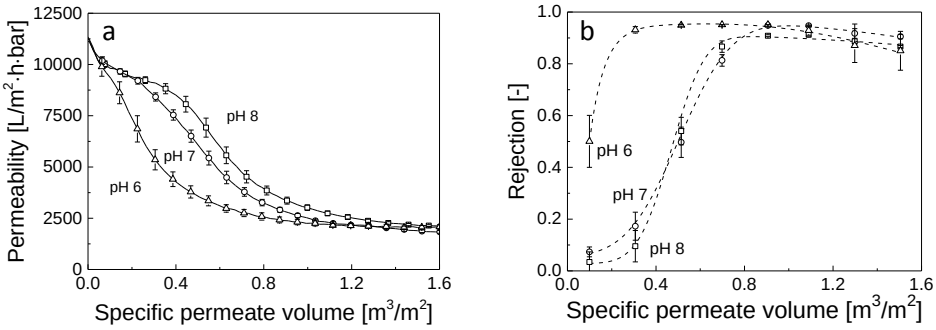

Fig. 8. (a) Permeability and (b) rejection as a function of the specific permeate volume at various pH of a 2 mg/L Ludox TM-50 silica nanoparticle feed solution.

Table 2. Characteristic parameters describing fouling development during dead-end microfiltration at various pH of a 2 mg/L Ludox TM-50 silica nanoparticle solution.

	pH	8	7	6
Blocking point	V_{block} [m^3/m^2]	0.27±0.03	0.27±0.03	0.07±0.01
	R_{block} [10^{10} 1/m]	3.9±0.1	3.9±0.1	3.6±0.1
Critical point	V_{crit} [m^3/m^2]	0.67±0.02	0.49±0.04	0.29±0.03
	R_{crit} [10^{10} 1/m]	7.1±0.6	7.1±0.6	6.3±0.05
	α [10^{13} kg/m^2]	7.2±0.2	7.4±0.3	8.2±0.4
Transition point	V_{mat} [m^3/m^2]	1.22±0.01	1.08±0.05	0.85±0.03
	R_{mat} [10^{10} 1/m]	14.6±0.7	14.6±0.7	14.5±0.9
	$(dR/dV)_{mat}$ [10^{10} 1/m^2]	5.2±0.8	2.70±0.3	1.4±0.5

Rejection data shown in Fig. 8b are in agreement with the permeability data shown in Fig. 8a. Decrease of the permeability coincides with an increase in nanoparticle rejection. Reduction of the pH from pH 8 to pH 7 and further down to pH 6 increases the rejection of silica nanoparticles. For pH 7, rejection in the first two permeate samples is improved just slightly, but for pH 6, the first permeate sample already shows a rejection of 50%. After pore blockage during the subsequent cake filtration stage, rejection

reached about 95% and then slightly dropped down to 91% at the end of the filtration at pH 7. Similarly, for pH 6 rejection during the early cake filtration stage is about 95% and drops slightly to 85% at the end of the filtration. The rejection drop at the end of the filtration is a result of increased particle concentration inside the membrane fiber. Similar observations for dead-end filtration, where an initially high rejection reduces with filtration time, were reported by van de Ven et. al [38].

2.4.2.3. Influence of the ionic strength and cation valency

An increase of the ionic strength of the nanoparticle solution causes contraction of the electrical double layer of the nanoparticles [21]. Consequently, the lower repulsive interaction energy between the nanoparticles leads to reduced stability of the nanoparticle. At the same time, during filtration of a solution with a higher ionic strength, the thickness electrical double layer thickness of the membrane surface is also reduced, facilitating foulant adsorption. With an increase in salt concentration from 1 mM to 10 mM and 50 mM NaCl, fouling is more severe and occurs faster, as shown in Fig. 9a. Similarly to filtration at lower pH (section 2.4.2.2.), each of the four characteristic points describing the shift to a next fouling stage are reached earlier at higher salt concentrations (see Table 3). Furthermore, the resistance at each of these points increases with salt concentration. Rejection data for the feed solution containing higher salt concentrations are shown in Fig. 9b. A higher salt concentration in the feed solution promotes a faster increase in silica nanoparticle rejection since pore blockage occurs earlier at higher ionic strength (Table 3).

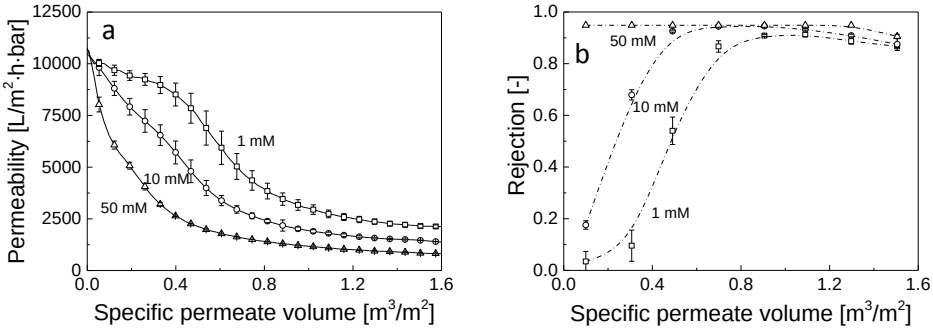

Fig. 9. (a) Permeability and (b) rejection as a function of the specific permeate volume for a 2 mg/L Ludox TM-50 silica nanoparticle solution at various NaCl concentrations at pH 8.

Table 3. Characteristic parameters describing fouling development during dead-end microfiltration for 2 mg/L Ludox TM-50 silica nanoparticles at various salt concentrations for two salts at pH 8.

Salt		**NaCl**			**$CaCl_2$**
Salt Concentration [mM]		**1**	**10**	**50**	**10**
Blocking point	V_{block} **[m^3/m^2]**	0.27±0.03	0.16±0.03	0.11±0.03	0.12±0.03
	R_{block} **[10^{10} 1/m]**	3.9±0.1	4.5±0.1	5.0±0.3	5.0±0.3
Critical point	V_{crit} **[m^3/m^2]**	0.67±0.02	0.52±0.02	0.35±0.04	0.31±0.03
	R_{crit} **[10^{10} 1/m]**	7.1±0.6	8.97±0.4	11.9±0.1	10.3±0.1
	α **[10^{13} m/kg]**	7.2±0.4	10.0±0.1	15.0±0.1	13.4±0.1
Transition point	V_{mat} **[m^3/m^2]**	1.22±0.01	1.10±0.03	0.82±0.02	0.98±0.02
	R_{mat} **[10^{10} 1/m]**	14.6±0.7	20.6±0.3	26.0±5.5	28.8±1.4
	$(dR/dV)_{mat}$ **[10^{10} 1/m^2]**	5.2±0.8	11.0±0.5	22.1±0.6	18.4±1.3

During the cake filtration stage, solutions of 10 mM and 50 mM NaCl result in higher rejections (about 95%) than the reference solution containing 1 mM NaCl (about 90%). Due to contraction of the electrical double layer, the distance between the nanoparticles in the formed filtration cake is lowered. As a consequence, the specific cake resistance α rises with salt concentration (see Table 3). Furthermore, a decreased energy barrier against nanoparticle aggregation facilitates a more homogenous

deposition of nanoparticles on the membrane surface. The SEM images in Fig. 10a, c, and e visually show that there is a strong relation between the salt concentration in the feed solution, the density of the filtration cake and the filtration cake homogeneity. A more homogenous nanoparticle deposition and more uniform coverage the membrane pores was obtained at higher salt concentrations. Therefore, the morphology of the formed nanoparticle deposit, and consequently also the rejection of colloidal silica during the cake filtration stage (Fig. 9b) is determined by the reduced repulsive interactions between the nanoparticles.

The last maturation stage, initiated at the transition point, occurs faster for higher salt concentrations as a result of a facilitated fouling development and shorter duration of the initial fouling stages. Resistance increment in the maturation stage $(dR/dV)_{mat}$ rises with salt concentration (Table 3) indicating severe fouling development and filtration under conditions which are far from critical flux conditions. This continuous increase of resistance in the final filtration stage reveals the important role of the salt concentration on nanoparticle destabilization [21] and fouling promotion, which is more pronounced than role of pH (see Fig. 8a).

The influence of the cation valency of the added salt in the feed solution on the fouling and rejection of silica nanoparticles is shown in Fig. 11a and Fig 11b, respectively. Like in the previous cases, in order to quantitatively determine the role of the cation valency, characteristic points were calculated and listed in Table 3. Fig. 11 clearly shows that addition of bivalent $CaCl_2$ to the feed solution induces more severe fouling than the addition of the monovalent counterpart (NaCl). A higher valency of the ions more effectively reduces the stability of the nanoparticle suspension. This phenomenon can be attributed to contraction of the electrical double layer, which increases with ion valency. Thus, for the same cation concentration of the mono – and divalent salt, fouling develops faster for the divalent salt, as shown in Fig. 11a and listed in Table 3. As before, easier destabilization of the colloidal suspension results in easier and more severe pore blockage, which significantly improves nanoparticle rejection (Fig.11b).

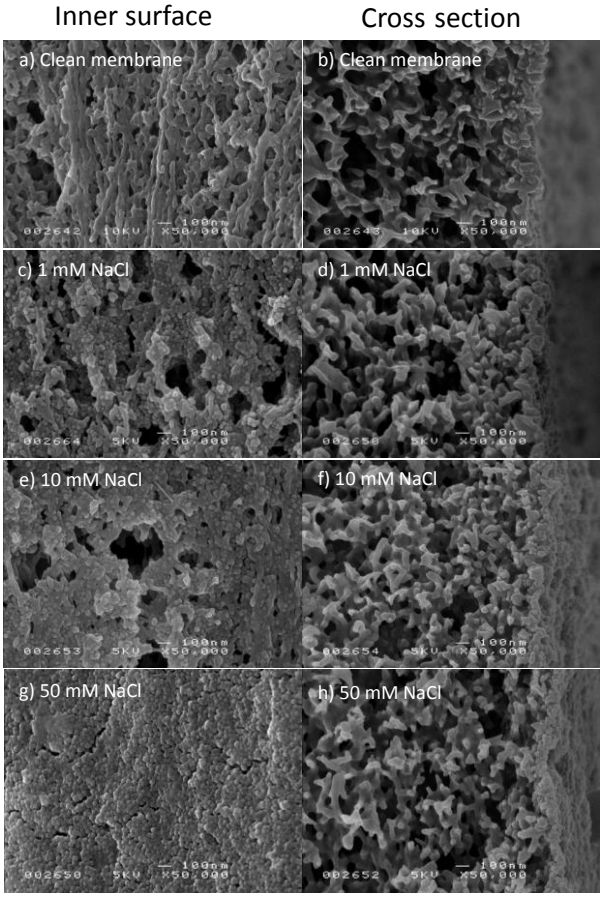

Fig. 10. SEM images of a clean MF PES/PVP membrane and the membrane fouled with Ludox TM-50 silica nanoparticles filtered using solutions with various ionic strengths; nanoparticle concentration 2 mg/L; pH 8; (a) inner surface, clean membrane, (b) cross section, clean membrane (c) inner surface, 1 mM NaCl, (d) cross-section; 1mM NaCl; (e) inner surface, 10 mM NaCl, (f) cross section*, 10 mM NaCl; (g) inner surface, 50 mM NaCl, (h) cross section, 50 mM NaCl.*

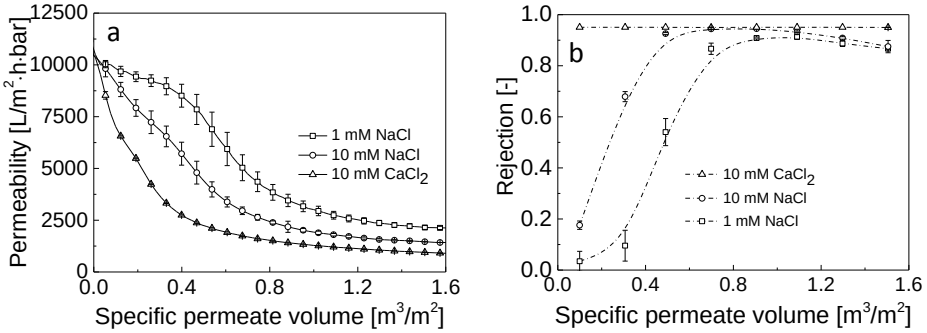

Fig. 11. (a) Permeability and (b) rejection as a function of the specific permeate volume during dead-end filtration of 2 mg/L Ludox HT-50 silica nanoparticles at pH 8 with addition of NaCl or $CaCl_2$.

2.5. Conclusions

This chapter clearly shows that by applying microfiltration membranes in dead-end filtration mode, rejection of electrostatically stabilized nanoparticles having a much smaller size than membrane pores is possible. Rejection and fouling development can be easily controlled since fouling behavior of silica nanoparticles is strongly related to both particle-particle and membrane-particle surface interactions. In this chapter, we distinguished five fouling stages during constant pressure dead-end microfiltration of stable silica nanoparticle suspensions: solute adsorption, transport through the membrane pores, pore blockage, cake filtration and cake maturation. Due to the moderate filtration conditions and high stability of nanoparticles, even higher concentrations of nanoparticles do not change the behavior of the initial fouling steps (adsorption and transport through pores) but just lead to their acceleration. A high stability of the nanoparticles allows filtration under critical flux conditions, where a relatively lower filtration resistance and rejection of about 90% were obtained. Fouling and rejection development can be accelerated by the addition of components that reduce the stability of the nanoparticle suspension (e.g. salts). These reduce the total repulsive interaction energy. A lower surface charge of both particles and membrane, which is achieved by a lower pH, also reduces the stability of the silica nanoparticles and in that way promotes fouling. Divalent salts are more effective in promoting fouling than monovalent salts. This chapter clearly shows great potential of porous membranes, which have pore size much bigger than the nanoparticle size, to remove electrostatically stabilized nanoparticles in dead-end filtration by formation of secondary dynamic membrane.

References

[1] S. F. Hansen, E. S. Michelson, A. Kamper, P. Borling, F. Stuer-Lauridsen, A. Baun, Categorization framework to aid exposure assessment of nanomaterials in consumer products, Ecotoxicology 17 (2008) 438-447

[2] A. H. Taheri, L. N. Sim, C. T. Haur, E. Akhondi, A. G. Fane, The fouling potential of colloidal silica and humic acid and their mixtures, J. Membr. Sci. 433 (2013) 112-120

[3] G. Orts-Gil, K. Natte, D. Drescher, H. Bresch, A. Mantion, J. Kneipp, et al., Characterisation of silica nanoparticles prior to in vitro studies: from primary particles to agglomerates, J. Nanopart. Res. 13 (2010) 1593-1604

[4] A. E. Contreras, A. Kim, Q. Li, Combined fouling of nanofiltration membranes: Mechanisms and effect of organic matter, J. Membr. Sci. 327 (2009) 87-95

[5] S. Surawanvijit, H. H. Liu, M. Kim, Y. Cohen, Removal of metal oxide nanoparticles from aqueous suspensions, Separ. Sci. Technol. 49 (2014) 161-170

[6] C. Y. Tang, T. H. Chong, A. G. Fane, Colloidal interactions and fouling of NF and RO membranes: a review, Adv. Colloid Interface Sci. 164 (2011) 126-43

[7] H. Weinberg, A. Galyean, M. Leopold, Evaluating engineered nanoparticles in natural waters, Trends. Anal. Chem. 30 (2011) 72-83

[8] J. Wang, J. Guan, S. R. Santiwong, T. D. Waite, Effect of aggregate characteristics under different coagulation mechanisms on microfiltration membrane fouling, Desalination 258 (2010) 19-27

[9] A. S. Kim, A. E. Contreras, Q. Li, R. Yuan, Fundamental mechanisms of three-component combined fouling with experimental verification, Langmuir 25 (2009) 7815-7827

[10] C. Henry, J.-P. Minier, G. Lefèvre, Towards a description of particulate fouling: From single particle deposition to clogging, Adv. Colloid Interface Sci. 185–186 (2012) 34-76

[11] E. M. Tracey, R. H. Davis, Protein fouling of track-etched polycarbonate microfiltration membrane, J. Colloid Interface Sci. 167 (1994) 104-116

[12] G. Dalwadi, H. A. E. Benson, Y. Chen, Comparison of diafiltration and tangential flow filtration for purification of nanoparticle suspensions, Pharmaceut. Res. 22 (2005) 2152-2162

[13] C. Henry, J. A. Brant, Mechanistic analysis of microfiltration membrane fouling by buckminsterfullerene (C60) nanoparticles, J. Membr. Sci. 415-416 (2012) 546-557

[14] D. Jassby, S. R. Chae, Z. Hendren, M. Wiesner, Membrane filtration of fullerene nanoparticle suspensions: effects of derivatization, pressure, electrolyte species and concentration, J. Colloid Interface Sci. 346 (2010) 296-302

[15] S. F. Sweeney, G. H. Woehrle, J. E. Hutchison, Rapid purification and size separation of gold nanoparticles via diafiltration, J. Am. Chem. Soc. 128 (2006) 3190-3197

[16] T. Yin, H. W. Walker, D. Chen, Q. Yang, Influence of pH and ionic strength on the deposition of silver nanoparticles on microfiltration membranes, J. Membr. Sci. 449 (2014) 9-14

[17] Y. Chen, H. Kim, Monte Carlo simulation of pore blocking and cake formation by interfacial interactions during membrane filtration, Desalination 233 (2008) 258-266

[18] S. F. Sweeney, G. H. Woehrle, E. Hutchison, Rapid Purification and Size Separation of Gold Nanoparticles via Diafiltration, J. Am. Chem. Soc. 128 (2006) 3190-3197

[19] Y. S. Polyakov, A. L. Zydney, Ultrafiltration membrane performance: Effects of pore blockage/constriction, J. Membr. Sci. 434 (2013) 106-120

[20] P. Bacchin, A. Marty, P. Duru, M. Meireles, P. Aimar, Colloidal surface interactions and membrane fouling: Investigations at pore scale, Adv. Colloid Interface Sci. 164 (2011) 2-11

[21] C. Metin, L. Lake, C. Miranda, Q. Nguyen, Stability of aqueous silica nanoparticle dispersions, J. Nanopart. Res. 13 (2011) 839-850

[22] Y. Zhang, Y. Chen, P. Westerhoff, K. Hristovski, J. C. Crittenden, Stability of commercial metal oxide nanoparticles in water, Water Res. 42 (2008) 2204-2212

[23] K. A. Huynh, K. L. Chen, Aggregation Kinetics of citrate and polyvinylpyrrolidone coated silver nanoparticles in monovalent and divalent electrolyte solutions, Environ. Sci. Technol. 45 (2011) 5564-5571

[24] P. Aimar, P. Bacchin, Slow colloidal aggregation and membrane fouling, J. Membr. Sci. 360 (2010) 70-76

[25] G. Bolton, D. Lacasse, R. Kuriyel, Combined models of membrane fouling: Development and application to microfiltration and ultrafiltration of biological fluids, J. Membr. Sci. 277 (2006) 75-84

[26] A. Grenier, M. Meireles, P. Aimar, P. Carvin, Analysing flux decline in dead-end filtration, Chem. Eng. Res. Des. 86 (2008) 1281-1293

[27] J. Hermia, Constant Pressure Blocking Filtration Laws – Application to Power-law Non Newtonian Fluids, Trans. IChemE. 60 (1982) 111-120

[28] K. Xiao, Y. Shen, X. Huang, An analytical model for membrane fouling evolution associated with gel layer growth during constant pressure stirred dead-end filtration, J. Membr. Sci. 427 (2013) 139-149

[29] K. Xiao, Y. Shen, S. Liang, P. Liang, X. Wang, X. Huang, A systematic analysis of fouling evolution and irreversibility behaviors of MBR supernatant hydrophilic/hydrophobic fractions during microfiltration, J. Membr. Sci. 467 (2014) 206-216

[30] L. Palacio, C.-C. Ho, A. L. Zydney, Application of a pore-blockage—cake-filtration model to protein fouling during microfiltration, Biotechnol. Bioeng. 79 (2002) 260-270

[31] G. P. Van der Beek, M. A. C. Stuart, T. Cosgrove, Polymer adsorption and desorption studies via proton NMR relaxation of the solvent, Langmuir 7 (1991) 327-334

[32] A. I. Schäfer, A. Pihlajamäki, A. G. Fane, T. D. Waite, M. Nyström, Natural organic matter removal by nanofiltration: effects of solution chemistry on retention of low molar mass acids versus bulk organic matter, J. Membr. Sci. 242 (2004) 73-85

[33] G. Belfort, R. H. Davis, A. L. Zydney, The behavior of suspensions and macromolecular solutions in crossflow microfiltration, J. Membr. Sci. 96 (1994) 1-58

[34] S. Chellam, X. W., Blocking laws analysis of dead-end constant flux microfiltration of compressible cakes, J. Colloid Interface Sci. 301 (2006) 248-257

[35] S. T. V. Sim, A. H. Taheri, T. H. Chong, W. B. Krantz, A. G. Fane, Colloidal metastability and membrane fouling – effects of crossflow velocity, flux, salinity and colloid concentration, J. Membr. Sci. 469 (2014) 174-187

[36] M. Wessling, Two-dimensional stochastic modeling of membrane fouling, Sep. Purif. Technol. 24 (2001) 375–387

[37] S. Mochizuki, A. L. Zydney, Theoretical analysis of pore size distribution effects on membrane transport, J. Mem. Sci. 82 (1993) 211-227

[38] W. J. C. van de Ven, K. van't Sant, I. G. M. Pünt, A. Zwijnenburg, A. J. B. Kemperman, W. G. J. van der Meer, et al., Hollow fiber dead-end ultrafiltration: Axial transport variations during humic acid filtration, J. Mem. Sci. 314 (2008) 112-122

CHAPTER 3

Size and polydispersity in fouling development during dead-end microfiltration of engineered nanoparticles

This chapter has submitted as:
Krzysztof W. Trzaskus, Antoine Kemperman and Kitty Nijmeijer
Understanding role of nanoparticle size and polydispersity in fouling development during dead-end microfiltration
Journal of Membrane Science

Abstract

The recent exponential growth of nanotechnology and numerous applications of nanotechnology-based products resulted in water pollution by engineered nanoparticles. Over the last few decades, membrane technology has emerged as one of the most promising and reliable techniques in water purification. Therefore, it is an obvious candidate to remove manufactured nano-sized contaminants and to purify the water. Nanoparticle properties play a crucial role in the performance and effectiveness of membrane filtration.

This experimental study investigates the role of nanoparticle size and polydispersity on fouling and rejection development during dead-end microfiltration of electrostatically stabilized silica nanoparticles. Our studies on 11 nm, 25 nm and 92 nm monodisperse silica nanoparticles demonstrates that with bigger nanoparticle diameter, membrane pore (~200 nm) blockage is accelerated and cake filtration develops faster. The specific cake resistance of the filtration cake formed decreases with increasing nanoparticle diameter. Filtration of polydisperse nanoparticles (obtained by mixing monodisperse suspensions in various ratios) shows that increasing the fraction of smaller nanoparticles results in delayed pore blockage, and cake filtration occurring at a later stage. The specific cake resistance of the polydisperse nanoparticles is always found to be in between that obtained for the monodisperse nanoparticle suspensions. An increasing weight fraction of larger nanoparticles results in faster development of nanoparticle rejection due to accelerated pore blockage. However, because of the highly porous structure of the filtration cake originating from strong surface charges, the moderate transmembrane pressure applied and cake imperfections, the smallest (11 nm) nanoparticles were rejected only to a low extent, even during the cake filtration stage. An increase in applied transmembrane pressure during filtration of the polydisperse suspension resulted in faster pore blockage and higher specific cake resistance. Nevertheless, rejection of the nanoparticles in the cake filtration stage improved only slightly with increasing transmembrane pressure.

3.1. Introduction

Increasing production of engineered nanoparticles results in their accumulation in drinking water sources [1-4]. Due to their size range, nanoparticles are classified as colloidal particles, which can be effectively removed by membranes [5-7]. However, to date inevitable fouling phenomena reducing membrane performance limits the widespread usage of membrane technology in water purification [8, 9]. Even though the backgrounds of fouling phenomena are rather well understood, the various kinds of feed solutions, membranes and filtration modes make an accurate prediction of the fouling behavior in the case of nanoparticles challenging yet.

Nanoparticle rejection is not only determined by the ratio between the membrane pore size and the nanoparticle size, but also electrostatic or steric repulsion effects between solute and membrane material determine to a large extent the retention [10]. Furthermore, pore blocking and/or concentration polarization phenomena occurring during the filtration may change nanoparticle rejection [11, 12]. Due to a combination of those effects, as shown in our previous chapter [13], membranes with much bigger pores than the nanoparticle diameter can still reject nanoparticles. We have shown that during dead-end filtration of a stable nanoparticle suspension with membrane pores much bigger than the nanoparticle diameter, fouling develops in five stages: 1) nanoparticle adsorption onto the membrane, 2) transport through the membrane pores, 3) pore blocking, 4) cake filtration, and 5) cake maturation (see Fig. 1a). Due to pore blockage and formation of a nanoparticle deposit on the membrane surface acting as a dynamic secondary membrane, further transport of the nanoparticles through the membrane is limited. As a result, nanoparticle rejection also increases significantly during the course of the filtration, as shown in Fig. 1b.

Although our previous chapter describes filtration of a monodisperse model nanoparticles suspension, in practice real feed waters contain nanoparticles of various sizes resulting in a more complex filtration behavior. This justifies the further investigation of the role of nanoparticle polydispersity on membrane filtration performance and fouling behavior.

Several studies proved that the resistance of the filtration cake formed by polydisperse suspensions is different from that obtained for monodisperse solutions [14, 15]. McDonogh et al. [16] studied the influence of nanoparticle polydispersity on the formation of the nanoparticle deposit. They showed that increasing polydispersity of the charged nanoparticles resulted in a more porous and less ordered cake structure. Kim and

Ng [17] showed that polydisperse nanoparticles form a denser filtration cake when a greater number of smaller nanoparticles was present in the feed solution.

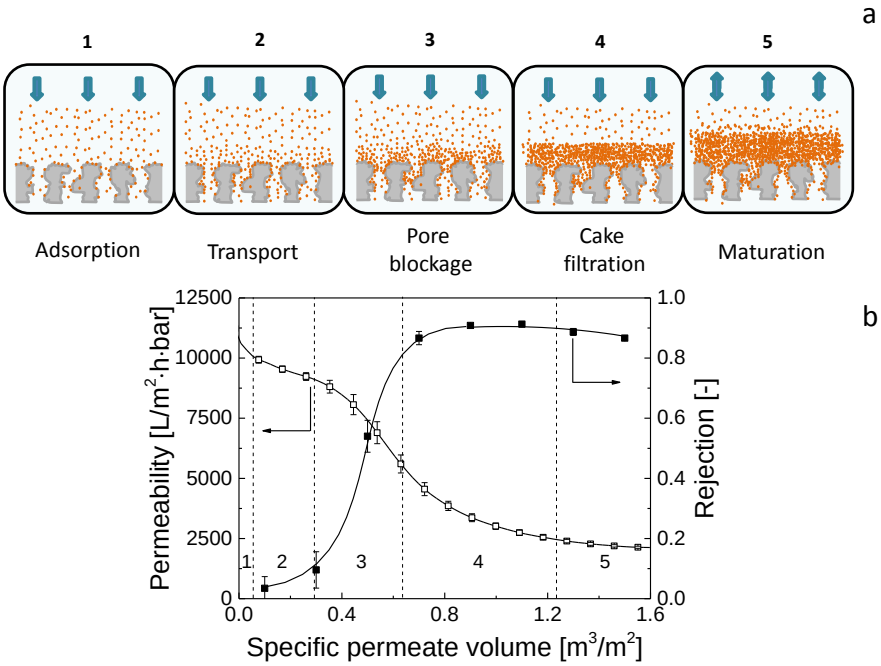

Fig. 1. (a) Fouling mechanism of the membrane during dead-end microfiltration of nanoparticles much smaller than the membrane pore size; (b) Permeability and rejection of silica nanoparticles as a function of the specific permeate volume during dead-end microfiltration of 2 mg/L Ludox TM-50 silica nanoparticles (adapted from [13]).

To the best of our knowledge, there are no systematic studies carried out on the determination of the role of nanoparticle polydispersity in fouling development resulting in pore blockage and subsequent cake filtration. In this chapter, the effect of nanoparticle size and size distribution on fouling and rejection development is investigated. The use of a controlled size distribution of nanoparticles in the feed solution, combined with extensive filtration data, allow the determination of the mechanisms responsible for fouling and nanoparticle rejection of polydisperse nanoparticles in dead-end microfiltration.

3.2. Experimental

3.2.1. Materials

Colloidal silica Ludox TM-50 (50% w/w), Ludox SM (30% w/w) (both from Sigma Aldrich) and Levasil 30/50 (50% w/w) (AkzoNobel), which vary in average nanoparticle size, were provided as a water suspension. ACS grade NH_4HCO_3, $(NH_4)_2CO_3$, HCl and NaOH (Sigma Aldrich) were applied to adjust the pH and ionic strength of the colloidal suspensions used. All chemicals were used without further purification; all solutions were prepared using ultrapure Milli-Q water (resistivity >18.2 MΩ·cm).

3.2.2. Feed and permeate characterization

The surface zeta potential of the silica nanoparticles were measured by electrophoretic mobility measurements using a Malvern ZetaSizer 3000Hsa. The measurements were carried out with a 0.5 g/L nanoparticles suspension with pH 8, prepared by dilution of the commercial suspensions in Milli-Q water. Transmission Electron Microscope (TEM) images of silica nanoparticles in the stock suspensions were obtained using a Philips CM300ST-FEG microscope. The number size distribution of each nanoparticle type was determined from the TEM images using ImageJ 1.48v software (National Institute of Health). We used a Scanning Mobility Particle Sizer (SMPS) model 3936 to measure the particle size distribution in the feed and permeate samples. The SMPS consisted of an electrostatic classifier model 3080, a neutralizer model 3077 with a Krypton-85 source (370MBq), a nano DMA model 3085 and a butanol based Condensation Particle Counter (CPC) model 3025A, all from TSI Incorporated (USA). The SMPS combined particle size classification according to the particle mobility diameter with measurement of the concentration using a CPC [18]. Briefly, nanoparticles firstly were aerosolized with Electrospray Aerosol Generator model 3480. Electrical mobility of the nanoparticles in air is size dependent, and this mobility was measured by SMPS model 3936. The system was adjusted to a size range between 10 nm and 100 nm, a scan time of 95 seconds, a retrace time of 15 seconds, and a two minute recurrence interval.

3.2.3. Membrane and membrane characterization

We used a commercial Pentair X-Flow 1.5MF02 inside/out hollow fiber membrane (OD 2.4 mm, ID 1.5 mm, kindly provided by Pentair X-Flow BV, the Netherlands), in all filtration experiments. The membrane was characterized in terms of pore size distribution (with capillary flow porometry), surface zeta potential (using streaming potential measurements) and clean water permeability. Detailed description of the filtration module preparation and membrane characterization was described in details elsewhere [13].

The properties of the MF membrane used are shown in Table 1. These data are taken from our previous study [13]. The clean water permeability of the membrane was about 11500 ± 500L/m^2·h·bar. The average mean flow pore diameter measured with capillary flow porometry was found to be 200 ± 15 nm. The inside (lumen) surface of the membrane is negatively charged at pH 8 with zeta potential of -23.1 ± 2.1 mV.

Table 1. Properties of the hollow fiber MF membrane used [13].

Membrane				
Type	Material	Clean water permeability [L/m^2·h·bar]	Pore size[nm]	Zeta potential at pH 8 [mV]
Pentair X-Flow 1.5MF02	PES/PVP	11500 ± 500	200 ± 15	-23.1 ± 2.1

3.2.4. Filtration experiments and data processing

We conducted all filtration experiments in a constant pressure filtration setup, assembled according to Fig. 2.

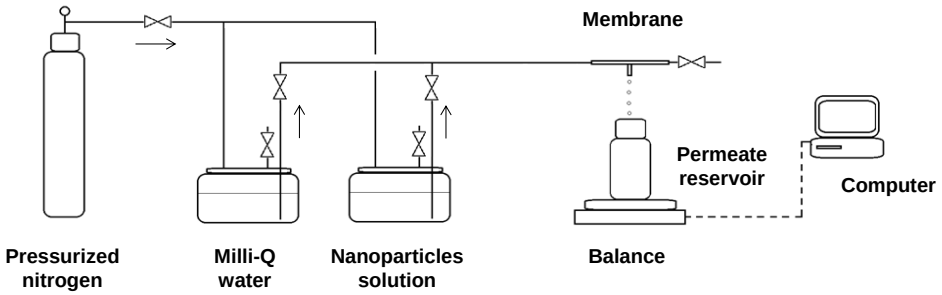

Fig. 2. Flow sheet of the constant pressure filtration setup used.

A detailed description of the experimental procedure was given in our previous study [13]. Briefly, a single filtration experiment consists of Milli-Q water filtration (50 mL) followed by nanoparticle filtration (400 mL of the feed solution). Continuous cumulative mass increment was recorded by an analytical balance connected to the computer. The permeability was calculated according to Eq. (1):

$$L_P = \frac{J}{\Delta P} \tag{1}$$

where L_p is the liquid permeability (L/m^2·h·bar), J is the flux (L/m^2·h), and ΔP is the transmembrane pressure (bar). Every 50 mL, permeate samples were collected and the silicon content in the samples was analyzed by ICP-MS (Inductively Coupled Plasma Mass Spectrometry, Thermo Fisher Xseries 2). Rejection of the silica nanoparticles was calculated according to Eq. (2):

$$\sigma = 1 - \frac{C_P}{C_f} \tag{2}$$

where σ is the rejection (-), C_P is the concentration of the nanoparticles in the permeate sample (mg/L), and C_f is the concentration of the nanoparticles in the feed solution (mg/L).

Due to the asymmetric structure of the membrane applied, pore blockage occurred only in a thin selective layer of the membrane. As a result, contribution of the pore blockage to the filtration resistance was limited [13]. Therefore, the filtration resistance originated mainly from the nanoparticle deposition on the membrane surface in form of a filtration cake. Formation of this cake leads to a reduction of the permeate flux and can be described using Eq. (3):

$$J = \frac{\Delta P}{\eta \cdot (R_m + R_c)} \tag{3}$$

where η is the viscosity (Pa·s), R_m is the membrane resistance (1/m) and R_c is the additional resistance caused by deposition of nanoparticles on the membrane (1/m) as a cake, defined as:

$$R_c = \alpha \frac{m_P}{A} \tag{4}$$

Here, α is the specific cake resistance (m/kg), m_p is the mass of the filtration cake deposited on the membrane surface (kg), and A is the membrane area (m^2). The specific cake resistance α quantitatively describes compaction of the cake layer. The cake

compression increases with applied transmembrane pressure, often estimated in terms of empirical power-law function as [19]:

$$\alpha = \alpha_0 (\Delta P)^s \quad (5)$$

where α_0 is a constant related to the size and shape of the particles (m/kg)/(Pa)^s, and s is the compressibility coefficient (-), which varies from 0 for an incompressible cake to a value near 1 for a highly compressible cake.

To investigate the role of the nanoparticle size and polydispersity in dead-end microfiltration, we prepared and filtered Milli-Q water solutions containing 1mM ammonium bicarbonate buffer and 2 mg/L of silica nanoparticles with pH 8. Firstly, to evaluate the effect of nanoparticle size in fouling development, we used feed solutions containing monodisperse Ludox TM-50, Ludox SM or Levasil 30/50 nanoparticles. Secondly, the role of nanoparticle polydispersity was investigated by the filtration of a nanoparticle suspension containing 2 mg/L of binary mixtures of Ludox SM, Ludox TM-50 or Levasil 30/50 nanoparticles in weight ratios 5:1, 1:1 or 1:5. For simplicity, we refer to these mixtures of Ludox SM, Ludox TM-50 and Levasil 30/50 according to the average size of the nanoparticles. Therefore, in the result and discussion section we refer to the mixture of Ludox SM and Ludox TM-50 as 11:25 mixture, to the mixture of Ludox SM and Levasil 30/50 as 11:92 mixture, and to the mixture of Ludox SM and Ludox TM-50 as 25:92 mixture.

Initially, we carried out all filtration experiments at a transmembrane pressure of 0.2 bar and at room temperature. The role of transmembrane pressure on fouling and rejection development was investigated by applying lower (0.1 bar) or higher (0.4 bar) transmembrane pressures for filtration of the polydisperse nanoparticle suspensions.

3.3. Results and discussion

3.3.1. Nanoparticles

The silica nanoparticles used were analyzed by TEM microscopy. As shown in Fig. 3, the silica nanoparticles in the commercial suspensions vary significantly in their size. From the TEM measurements, for each commercial suspension the size distribution was analyzed. The calculated number average size diameters of the silica nanoparticles are 10.9 ± 1.9 nm, 25.5 ± 5.2 nm and 92.3 ± 14.2 nm for Ludox SM, Ludox TM-50 and Levasil 30/50, respectively. The ratio between the pore size of the membrane (see Table 1) and the nanoparticle diameter is about 18, 8, and 2 for Ludox SM, Ludox TM-50 and Levasil 30/50, respectively.

The characteristics of the nanoparticles used are listed in Table 2. Due to the same surface chemistry and presence of silanol groups [20], the surface of all three nanoparticle types is negatively charged at pH 8 (about -39.9 ± 3.4 mV, -37.7 ± 3.9 mV and -48.7 ± 1.2 mV for Ludox SM, Ludox TM-50 and Levasil 30/50, respectively).

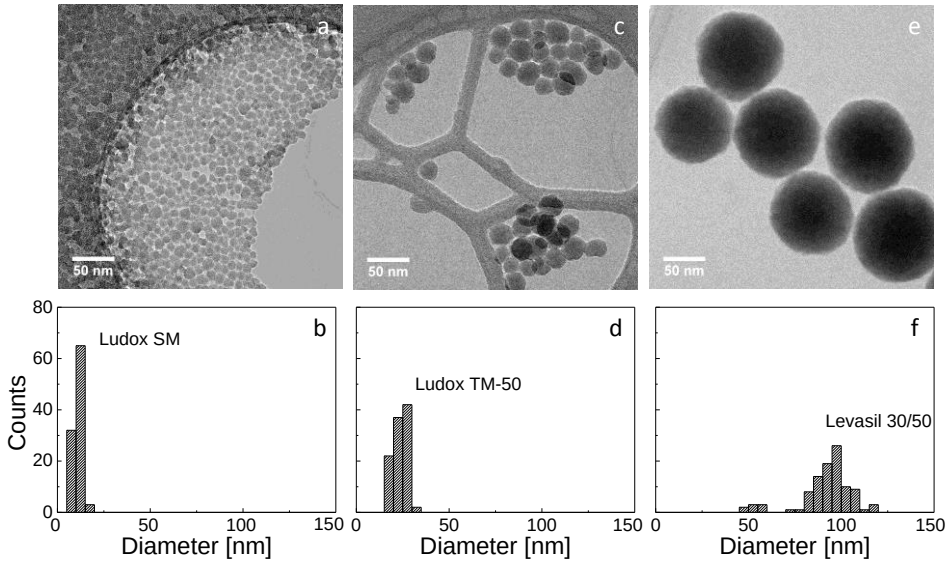

Fig.3. (a) TEM image and (b) number size distribution of Ludox SM silica nanoparticles, (c) TEM image and (d) number size distribution of Ludox TM-50 silica nanoparticles, (e) TEM image and (f) number size distribution of Levasil 30/50 silica nanoparticles.

Table 2. Measured properties of the used silica nanoparticles.

Nanoparticles		
Type	Average diameter [nm]	Zeta potential at pH 8 [mV]
Ludox SM	10.9 ± 1.9	-39.9 ± 3.4
Ludox TM-50	25.5 ± 5.2	-37.7 ± 3.9
Levasil 30/50	92.3 ± 14.2	-48.7 ± 1.2

3.3.2 Filtration experiments

3.3.2.1. Monodisperse nanoparticle suspensions

The influence of nanoparticle size on fouling development was investigated during constant pressure dead-end microfiltration at pH 8. Feed solutions containing 2 mg/L of silica nanoparticles were prepared by dilution of the commercial nanoparticle suspensions Ludox SM, Ludox TM-50 and Levasil 30/50, which all vary in nanoparticle size (Fig. 3 and Table 2). Fig. 4 shows permeability and rejection data of the investigated silica nanoparticles as a function of the specific permeate volume.

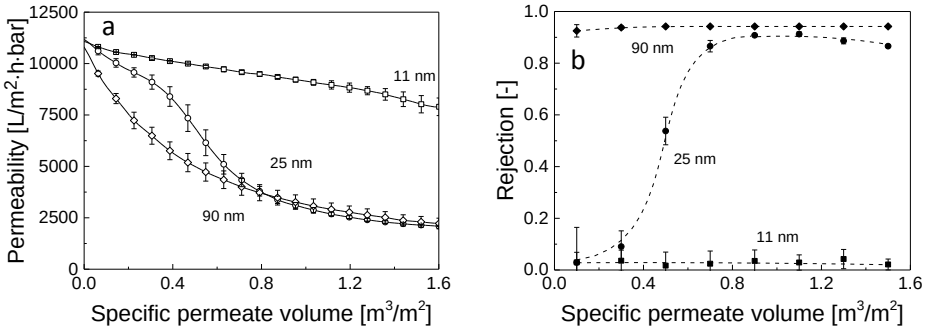

Fig. 4. (a) Permeability and (b) rejection as a function of specific permeate volume for various silica nanoparticle sizes during dead-end microfiltration of 2 mg/L silica nanoparticle suspensions at pH 8.

For all three nanoparticle sizes investigated, a decrease in permeability was observed after the introduction of the nanoparticles into the membrane module, as shown in Fig. 4a. However, the shape of the filtration curve, and therefore the fouling development, varies significantly for each nanoparticle size.

In the case of the smallest (11 nm) Ludox SM nanoparticles, permeability decreases only slightly (about 30%) during the filtration course. A much smaller nanoparticle diameter (see Table 2) than the membrane pore size (see Table 1) allows nanoparticle transport through the membrane without rejection, as shown in Fig. 4b. For the bigger Ludox TM-50 nanoparticles, having an average diameter of 25 nm (see Table 2), directly at the beginning of the filtration the permeability reduces to 90% of the initial pure water permeability (Fig. 4a). Later on, the permeability decreases slowly up to a specific permeate volume of 0.4 m^3/m^2, after which it drastically declines up to about 0.8 m^3/m^2. In the final filtration phase, the decrease in permeability once again slows down. In the same period, the rejection of the 25 nm nanoparticles increases from about 5% to 90%

(see Fig. 4b). Pore clogging and nanoparticle deposition later on leads to the formation of a secondary membrane, which limits nanoparticle transport across the membrane. As described in our previous chapter [13], the transition from nanoparticle transport to pore blockage is responsible for the concave part of the filtration curve, whereas the evolution from the cake filtration stage to the cake maturation stage is revealed as a convex part of the filtration curve. Such fouling development is characteristic for stable suspensions of nanoparticles having a diameter much smaller than the membrane pore diameter but large enough to be able to block membrane pores. For 92 nm Levasil 30/50 silica nanoparticles (see Table 2), immediately at the beginning of the filtration a fast decline in permeability is observed, as shown in Fig. 4a. Due to the size of the nanoparticles, which is closer to the membrane pore size, immediate pore blockage occurs resulting in almost 95% nanoparticle rejection already from the beginning of the filtration (see Fig. 4b). Interestingly, for 25 nm and 92 nm nanoparticles similar permeabilities and rejections are obtained at the end of the filtration course. These findings suggest that the filtration resistance for both 25 nm and 92 nm nanoparticles is identical, regardless of the size of the particles. However, this is misleading, as different amounts of nanoparticles accumulated on the membrane surface during a single filtration course of both particle sizes. In order to normalize the obtained filtration resistance for the amount of the nanoparticles deposited, in Fig. 5 the filtration resistance is plotted as a function of the accumulated nanoparticle mass. The accumulated nanoparticle mass was calculated from the mass balance using the nanoparticle concentrations in the feed solution and in the permeate samples.

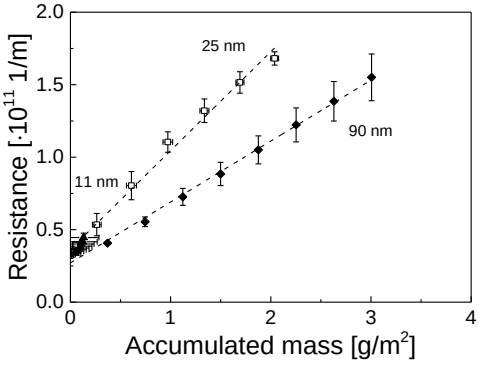

Fig. 5. Filtration resistance as a function of accumulated mass of silica nanoparticles on the membrane for three different nanoparticle sizes (▲– 11 nm, □ – 25 nm, ♦ – 92 nm).

For the 92 nm nanoparticles, due to the high nanoparticle rejection (95%) already from the beginning of the filtration (see Fig. 4b) on, a large amount of nanoparticles accumulated on the membrane surface (about 3 g/m^2). In the case of the 25 nm nanoparticles, pore blockage was delayed, which postponed the development of the filtration cake and delayed the increase of the nanoparticle rejection to about 90%. Thus, the final accumulated mass of the 25 nm nanoparticles is lower (about 2.3 g/m^2) than that obtained for the 92 nm nanoparticles (about 3 g/m^2). The smallest 11 nm nanoparticles do not clog the pores, and only a very limited amount of the nanoparticles is retained by the membrane and accumulated on the membrane. The slope of the resistance development versus accumulated nanoparticle mass (Fig. 5) is the specific cake resistance α (according to Eq. 4), which quantitatively represents the compaction of the filtration cake. Since the filtration resistance develops much faster with accumulated nanoparticle mass for 25 nm than for 92 nm nanoparticles (see Fig. 5.), the specific cake resistance α is greater for the smaller 25 nm nanoparticles, as listed in Table 3.

Table 3. Specific cake resistances obtained during dead-end filtration of monodisperse silica nanoparticles calculated using Eq. 4; na – not available.

Monodisperse nanoparticles	**Diameter [nm]**	**Specific cake resistance α [10^{13} m/kg]**
Ludox SM	11	na
Ludox TM-50	25	6.8±0.2
Levasil 30/50	92	4.3±0.7

The difference in specific cake resistance between the two nanoparticle sizes can be explained by the Kozeny–Carman equation [21], which describes the filtration resistance in a porous medium consisting of monodisperse and spherical particles:

$$R_c = 180 \cdot \frac{m_p}{d_p^2 \cdot A \cdot \rho_p} \frac{(1-\varepsilon)}{\varepsilon^3} \qquad (6)$$

where R_c is the filtration cake resistance (1/m), m_p is the mass of the filtration cake (kg), A is the membrane area (m^2), ρ_P is the density of the solute (kg/m^2), d_p the diameter of the spherical particle (m) and ε the porosity of the filtration cake (-).

According to Eq. 6, the filtration resistance of the filtration cake is inversely proportional to the square of the particle diameter. Therefore, by assuming the same packing, and thus porosity, of the filtration cake (due to the almost similar repulsive interactions), we can expect a much larger filtration resistance for smaller nanoparticles. This is also in line

with the results listed in Table 3, where the specific cake resistances are $6.8 \pm 0.2 \cdot 10^{13}$ m/kg and $4.3 \pm 0.7 \cdot 10^{13}$ m/kg for 25 nm and 92 nm nanoparticles, respectively.

3.3.2.2. Role of nanoparticle polydispersity: 11 and 25 nm particles

In this part, we discuss the role of nanoparticle polydispersity on permeability and rejection using 2 mg/L nanoparticle suspensions containing various ratios of 11 nm and 25 nm nanoparticles as an example. For that purpose, feed solutions containing Ludox SM and Ludox TM-50 silica nanoparticles in different ratios were prepared and filtered using the previously described procedure. Permeability decay and corresponding rejection developments are shown in Fig. 6.

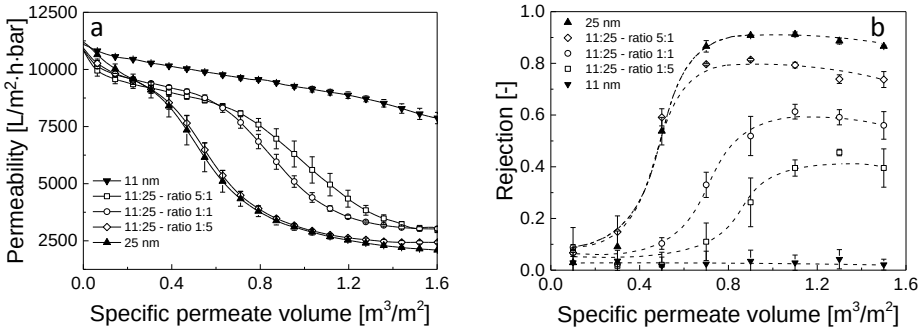

Fig. 6. (a) Permeability and (b) rejection of silica nanoparticles as a function of specific permeate volume for mixtures of 11 nm and 25 nm silica nanoparticles during dead-end microfiltration of 2 mg/L silica nanoparticle suspensions.

Figure 6a shows that the permeability decays obtained for the suspensions containing mixtures of 11 nm and 25 nm nanoparticles lay exactly in between the two filtration curves obtained for the monodisperse nanoparticle suspensions. With increasing concentration of bigger 25 nm nanoparticles, permeability decrease occurs faster due to easier pore blockage. This easier pore blockage at higher 25 nm nanoparticle concentrations results in a faster increase of the nanoparticle rejection, as shown in Fig. 6b. However, after this sudden rejection increase, for all polydisperse suspensions investigated the rejection stabilizes at a certain maximum level. For feed solutions containing Ludox SM and Ludox TM-50 in ratios 5:1, 1:1 and 1:5, nanoparticle rejection stabilizes at approx. 40%, 60% and 80%, respectively. McDonogh et al. [16] reported that for charged particles of different sizes, the packing order of the particles is looser and less ordered than for monodisperse nanoparticles. This more porous and less ordered

structure of the nanoparticle deposit facilitates nanoparticle diffusion through the filtration cake. Consequently, significantly lower nanoparticle rejections are obtained for polydisperse suspensions than for monodisperse 25 nm nanoparticles. Nevertheless, it is not clear whether the lower rejection is caused by diffusion of smaller nanoparticles through the filtration cake or whether it originates from defects in the filtration cake causing both 11 nm and 25 nm nanoparticles to be rejected to a lower extent. To investigate this in more detail, we performed Scanning Mobility Particle Sizer (SMPS) analysis. SMPS of the feed and permeate shows that the nanoparticle size distribution in the feed solutions is different than that of the permeate samples (see Fig. 7a). To quantify these differences, we took the separate data from the fraction of the smaller particles and the separate data from the fraction of the bigger particles, and calculated the rejection for both according to Eq. 2. Although TEM imaging shows that the average particle size of the smaller particles is around 11 and 25 nm, these data stem from particles in the dry state. SMPS data show slightly bigger particle sizes [22]. Therefore, in order to evaluate the rejection of smaller Ludox SM nanoparticles from the data obtained by SMPS, we arbitrary chose a fraction of nanoparticles with sizes between 12-16 nm. For the larger Ludox TM-50, we considered a representative fraction consists of nanoparticles having a size range between 25 nm and 37 nm. As shown in Fig. 7b, the fraction of bigger nanoparticles (25-37 nm) is retained much easier than the fraction of the smaller nanoparticles (12-16 nm).

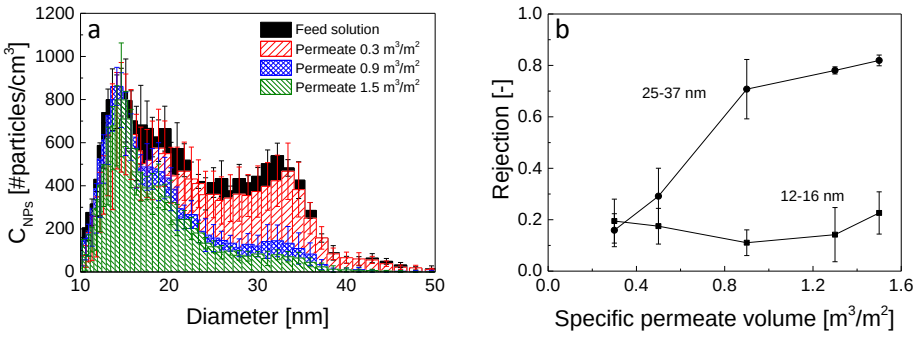

Fig. 7. (a) SMPS size distribution of feed and permeate samples (at three specific permeate volumes) obtained after filtration of a polydisperse suspension of silica nanoparticles; (b) Rejection development of two silica nanoparticle fractions as a function of the specific permeate volume. The 2 mg/L total feed solution was prepared by mixing Ludox SM and Ludox TM-50 in a mass ratio 1:1.

On the one hand, the lower retention of smaller nanoparticles was expected since filtration of monodisperse Ludox SM nanoparticles resulted in a rejection below 10% (see Fig. 4b). On the other hand, the deposition of Ludox TM-50 nanoparticles and the pore clogging should form a secondary membrane, which was expected to be less permeable for the small nanoparticles than the original unfouled membrane. We speculate that due to the surface charge of nanoparticles, application of a moderate transmembrane pressure and reduced packing order the filtration cake is highly porous; the distance between nanoparticles in the filtration cake allows preferential transport of smaller nanoparticles through the filtration cake. As a result, overall nanoparticle rejection reduces with a higher concentration of the smaller Ludox SM nanoparticles (Fig. 6b). Thus, the higher the concentration of smaller nanoparticles in the mixture, the fewer nanoparticles accumulate on the membrane surface and form the filtration cake. However, regardless of the reduced rejection of the fraction containing smaller nanoparticles (see Fig. 7b) their contribution to the reduction of the filtration cake porosity is clear. The specific cake resistance increases with concentration of 11 nm nanoparticles in feed solution, as listed in Table 4. We think that the smaller retained 11 nm nanoparticles can more effectively fill the voids between bigger 25 nm nanoparticles, and by this reduce the porosity of the filtration cake. Consequently, the specific cake resistance increases.

Table 4. Specific cake resistances obtained during dead-end filtration of polydisperse silica nanoparticle suspensions.

Polydisperse nanoparticle mixtures		**Specific cake resistance α [10^{13} m/kg]**		
Mixture	**Ratio**	**5:1**	**1:1**	**1:5**
11:25		12.5 ± 1.0	8.0 ± 0.7	6.7 ± 0.3
11:92		6.7 ± 0.2	4.7 ± 0.2	4.9 ± 0.1
25:92		6.2 ± 0.3	6.3 ± 0.4	5.3 ± 0.3

3.3.2.3. Role of nanoparticle polydispersity: larger particles

The difference between membrane pore size and nanoparticle diameter determines rejection and fouling evolution during dead-end filtration, as described before in section 3.3.2.1. In general, the bigger the nanoparticles are, the faster the rejection develops due to accelerated pore blockage, and the lower the filtration resistance of the filtration cake is.

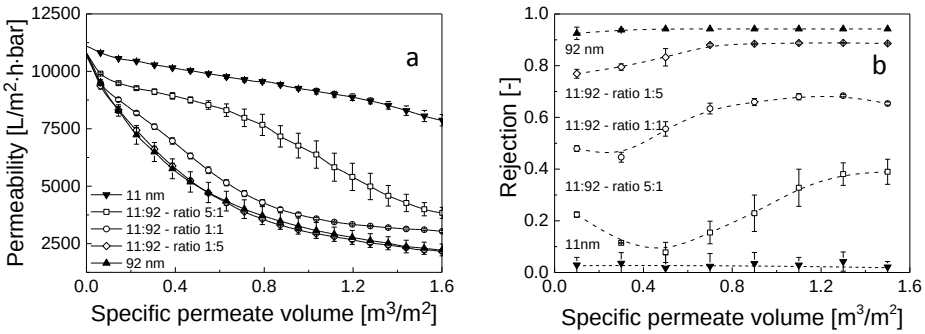

Fig. 8. (a) Permeability and (b) rejection of silica nanoparticles as a function of specific permeate volume for mixtures of 11 nm and 92 nm silica nanoparticles during dead-end microfiltration of 2 mg/L silica nanoparticle feed suspensions.

Similarly to the results discussed in section 3.3.2.2, Fig. 8a shows that permeability declines faster when a higher concentration of the larger Levasil 30/50 nanoparticles is used in the feed solution. The filtration curve changes gradually from a concave (for 11 nm nanoparticles) to a convex shape with increasing concentration of 92 nm nanoparticles. The transition to the convex shape indicates easier pore blockage of the membrane when a higher concentration of 92 nm nanoparticles is applied. In contrast to the results obtained for mixtures of smaller nanoparticles (11 nm and 25 nm in section 3.3.2.2), initial nanoparticle rejection (in the first permeate sample) was more or less proportional to the concentration of 92 nm nanoparticles in the feed solution, as shown in Fig. 8b. Quantitatively, the measured rejections of silica nanoparticles in the first permeate samples were approx. 22%, 48% and 77% for mass ratios 5:1, 1:1 and 1:5 of 11 nm and 92 nm nanoparticles in the feed solution, respectively. For 11:92 mixtures, the 92 nm nanoparticles immediately blocked the pores (as it is in the case of monodisperse 92 nm in Fig. 4) forming a filtration cake, whereas for the 11:25 mixtures both nanoparticle fractions initially could still be transported freely through the membrane pores. Furthermore, for the 11:92 mixture, the rejection did not develop that fast and

sharp as it was for the 11:25 mixtures. Bigger (92 nm) nanoparticles are retained already from the beginning of the filtration, but smaller (11 nm) nanoparticles can still be transported through the filtration cake, in agreement with the mechanism described for the 11:25 mixture in section 3.3.2.2. The low retention for 11 nm nanoparticles results only in a slight increase of the overall rejection, as shown in Fig. 8b. Nevertheless, the cake specific resistance increases with concentration of 11 nm nanoparticles (Table 4). This can only happen when smaller nanoparticles are retained and deposited in the structure of the filtration cake.

The filtration results obtained during dead-end filtration of mixtures containing 25 nm and 90 nm nanoparticles are given in Fig. 9.

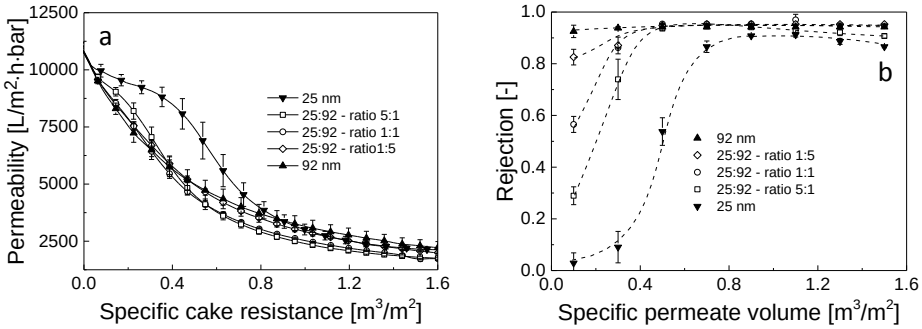

Fig. 9. (a) Permeability and (b) rejection of silica nanoparticles as a function of specific permeate volume for mixtures of 25 nm and 92 nm silica nanoparticles during dead-end microfiltration of 2 mg/L silica nanoparticle suspensions at pH 8.

Similarly to the previous cases, an increased concentration of 92 nm nanoparticles in a feed solution containing also 25 nm nanoparticles results in a faster transition of the concave filtration curve to a convex filtration curve, indicating that pore blockage becomes easier. Moreover, as in the case of 11:92 mixtures, initial rejection of nanoparticles is proportional to the concentration of 92 nm nanoparticles. However, in contrast to the 11:92 mixtures, nanoparticle rejection reached about 90-95% at the end of the filtration for all 25:92 ratios. This high nanoparticle rejection is due to the higher retention of the 25 nm nanoparticles by the filtration cake formed than is the case for the 11 nm particles. As expected also in this case, a higher concentration of 25 nm nanoparticles resulted in densification of the filtration cake, which is expressed as a higher specific cake resistance (Table 4).

3.3.2.4. Role of transmembrane pressure

The applied transmembrane pressure influences the distance between the deposited nanoparticles in the filtration cake formed, and thus the density of the filtration cake. Repulsive electrostatic interactions between the silica nanoparticles are acting against compaction of the filtration cake by the oppositely directed convective drag force. The applied transmembrane pressure determines the permeate flux, which on its turn determines the magnitude of the convective drag force. The role of the transmembrane pressure in fouling and rejection development during filtration of polydisperse nanoparticle suspension was investigated as well. For that purpose, dead-end filtrations of polydisperse silica nanoparticle suspensions were carried out at higher (0.4 bar) and lower (0.1 bar) transmembrane pressures than the reference 0.2 bar used so far. Figs. 10a and 10b show permeability and rejection development of the silica nanoparticle suspensions for different transmembrane pressures, respectively. The feed solution used in these experiments contained a 1:1 mixture of Ludox SM (11 nm) and Ludox TM-50 (25 nm) silica nanoparticles.

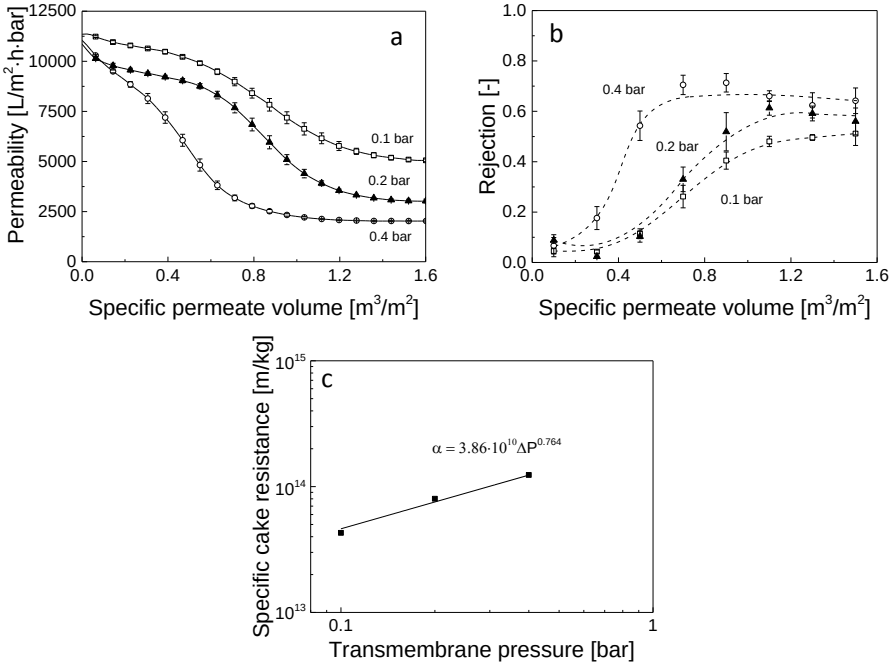

Fig. 10. (a) Permeability and (b) rejection of silica nanoparticles as a function of specific permeate volume and (c) specific cake resistance as a function of transmembrane pressure. Feed solution contained 2 mg/L of 11 nm and 25 nm nanoparticles at mass ratio 1:1 at pH 8.

As expected, an increase of the transmembrane pressure leads to a faster and more severe fouling development. A greater convective drag force at higher transmembrane pressures facilitates nanoparticle aggregation, accelerating pore blockage. This is responsible for the sharp permeability decline in Fig. 10a [13]. As a consequence, an increased transmembrane pressure enhances nanoparticle rejection, as shown in Fig. 10b. Especially, at 0.4 bar this rejection development is much faster than observed for the other two transmembrane pressures used (0.1 bar and 0.2 bar). Already visible from the third permeate sample (0.5 m^3/m^2), Fig. 10b shows that due to easier pore blockage, the rejection at 0.4 bar is about 54% in comparison to 10% at 0.1 and 0.2 bar.

Table 5. Specific cake resistances obtained during dead-end filtration of a feed suspension containing 2 mg/L of 11 nm and 25 nm silica nanoparticles at mass ratio 1:1 at various transmembrane pressures.

Transmembrane pressure [bar]	**Specific cake resistance α [10^{13} m/kg]**
0.1	4.3 ± 0.2
0.2	8.0 ± 0.7
0.4	12.4 ± 1.3

After pore blockage, a filtration cake formed on the membrane surface [13]. An indication for its compaction, and thus its contribution to the filtration resistance, is the permeability obtained at the end of the filtration process. As listed in Table 5, for all three transmembrane pressures investigated, the specific cake resistance increases with transmembrane pressure indicating cake compaction. We fitted the obtained specific cake resistances to a power-law function (Eq. 5), as shown in Fig. 10c. The estimated compressibility coefficient s was about 0.764, proving that the obtained filtration cake is highly compressible [23].

However, as shown in Fig. 10b, the absolute nanoparticle rejection at the end of the filtration when cake filtration is established [13], increases only slightly with the applied transmembrane pressure. In our case, the nanoparticle rejections measured for the last permeate samples were about 51%, 56% and 64% for 0.1 bar, 0.2 bar and 0.4 bar, respectively. These results clearly show that during cake filtration, nanoparticle rejection increases with the applied transmembrane pressure. However, irrespective of the reduced porosity, nanoparticles could still diffuse through the filtration cake, even at 0.4 bar.

5. Conclusions

In this experimental study we investigated fouling and rejection during dead-end microfiltration of mono- and polydisperse silica nanoparticles. The fouling development of electrostatically stabilized silica nanoparticles is strongly related to the size of the nanoparticles. The bigger the nanoparticles are, the faster pore blockage followed by the cake filtration occurs. When pore blockage happens earlier, a faster increase in nanoparticle rejection is observed. Therefore, an increasing concentration of bigger nanoparticles in a polydisperse suspension results in faster fouling and higher rejections. Nevertheless, the smallest 11 nm nanoparticles were retained only to a low extent in mixtures with bigger nanoparticles, even after formation of the filtration cake. Strong repulsive interactions and moderate transmembrane pressures allow diffusion of the smallest silica nanoparticles through the porous filtration cake. An increase in the transmembrane pressure resulted only in a slight improvement of nanoparticle rejection. The specific cake resistance increases with increasing transmembrane pressure and higher concentrations of smaller nanoparticles in the feed solution.

References

[1] T. E. Abbott Chalew, G. S. Ajmani, H. Huang, K. J. Schwab, Evaluating nanoparticle breakthrough during drinking water treatment, Environ. Health. Perspect. 121 (2013) 1161-1166

[2] S. F. Hansen, E. S. Michelson, A. Kamper, P. Borling, F. Stuer-Lauridsen, A. Baun, Categorization framework to aid exposure assessment of nanomaterials in consumer products, Ecotoxicology 17 (2008) 438-47

[3] H. Weinberg, A. Galyean, M. Leopold, Evaluating engineered nanoparticles in natural waters, Trends. Anal. Chem. 30 (2011) 72-83

[4] P. Westerhoff, G. Song, K. Hristovski, M. A. Kiser, Occurrence and removal of titanium at full scale wastewater treatment plants: implications for TiO2 nanomaterials, J. Environ. Monitor. 13 (2011) 1195-203

[5] K. M. Persson, G. Trägardt, G. Dejmek, Fouling behaviour of silica on four different microfiltration membranes, J. Membr. Sci. 76 (1993) 151-172

[6] A. I. Schäfer, U. Schwicker, M. M. Fischer, A. G. Fane, T. D. Waite, Microfiltration of colloids and natural organic matter, J. Membr. Sci. 171 (2000) 151-172

[7] S. Surawanvijit, M. Kim, Y. Cohen, Analysis of membrane filtration efficiency in removal of metal oxide nanoparticles from aqueous nanoparticle suspension in the presence of coagulation pretreatment, Clean Technology (2010) 343-345

[8] A. Grenier, M. Meireles, P. Aimar, P. Carvin, Analysing flux decline in dead-end filtration, Chem. Eng. Res. Des. 86 (2008) 1281-1293

[9] W. Guo, H.-H. Ngo, J. Li, A mini-review on membrane fouling, Bioresource Technol. 122 (2012) 27-34

[10] Y. S. Polyakov, A. L. Zydney, Ultrafiltration membrane performance: Effects of pore blockage/constriction, J. Membr. Sci. 434 (2013) 106-120

[11] E. M. Tracey, R. H. Davis, Protein fouling of track-etched polycarbonate microfiltration membranes, J. Coll. Interf. Sci. 167 (1994) 104-116

[12] K. Xiao, Y. Shen, X. Huang, An analytical model for membrane fouling evolution associated with gel layer growth during constant pressure stirred dead-end filtration, J. Membr. Sci. 427 (2013) 139-149

[13] K. W. Trzaskus, W. M. de Vos, A. Kemperman, K. Nijmeijer, Towards controlled fouling and rejection in dead-end microfiltration of nanoparticles – role of electrostatic interactions, J. Membr. Sci. 496 (2015) 174–184

[14] G. Foley, D. M. Malone, F. MacLoughlin, Modelling the effects of particle polydispersity in crossflow filtration, J. Membr. Sci. 99 (1995) 77-88

[15] A. E. Contreras, A. S. Kim, Q. Li, Combined fouling of nanofiltration membranes: Mechanisms and effect of organic matter, J. Membr. Sci. 327 (2009) 87-95

[16] R. M. McDonogh, A. G. Fane, C. J. D. Fell, H.-C. Flemming, The influence of polydispersity on the hydraulic behaviour of colloidal fouling layers on membranes: Perturbations on the behaviour of the "ideal" colloidal layer, Colloids Surf., A 138 (1998) 231–244

[17] A. S. Kim, A. N. L. Ng, Hydraulic permeability of polydispersed cake layers: an analytic approach, Desalination 207 (2007) 144-152

[18] I. W. Lenggoro, B. Xia, K. Okuyama, J. F. de la Mora, Sizing of colloidal nanoparticles by electrospray and differential mobility analyzer methods, Langmuir 18 (2002) 4584-4591

[19] S. Chellam, W. Xu, Blocking laws analysis of dead-end constant flux microfiltration of compressible cakes, J. Colloid Interface Sci. 301 (2006) 248-257

[20] C. Metin, L. Lake, C. Miranda, Q. Nguyen, Stability of aqueous silica nanoparticle dispersions, J. Nanopart. Res. 13 (2011) 839-850

[21] M. Mulder, Basic principles of membrane technology, 2nd ed., Dordrecht, Boston: Kluwer Academic, 2003

[22] G. Orts-Gil, K. Natte, D. Drescher, H. Bresch, A. Mantion, J. Kneipp, et al., Characterisation of silica nanoparticles prior to in vitro studies: from primary particles to agglomerates, J. Nanopart. Res. 13 (2011) 1593-1604

[23] S. Chellam, J. Jacangelo, Existence of critical recovery and impacts of operational mode on potable water microfiltration, J. Environ. Eng. 124 (1998) 1211-1219

CHAPTER 4

Membrane filtration of silica nanoparticles and polymeric stabilizers

This chapter has submitted as:
Krzysztof W. Trzaskus, Wiebe M. de Vos, Antoine Kemperman and Kitty Nijmeijer
Fouling behavior during microfiltration of silica nanoparticles and polymeric stabilizers
Journal of Membrane Science

Abstract

Nanotechnology applications give rise to new forms of water pollution, resulting in a need for reliable technologies that can remove nanoparticles from water. Membrane filtration is an obvious candidate. The tendency of nanoparticles to become instable in suspension and form aggregates strongly influences their filtration behavior. This experimental study investigated fouling and rejection during dead-end microfiltration of sterically stabilized nanoparticles. Polyvinylpyrrolidone (PVP) with different molecular weights at different concentrations was used as model steric stabilizer. The large difference between membrane pore size (~200 nm) and the size of the silica nanoparticles (25 nm) allowed a detailed investigation of the filtration process and fouling development. We characterized the feed solution with optical reflectometry, dynamic light scattering, zeta potential measurements and asymmetric flow field flow fractionation (AF4) combined with static light scattering. Subsequently, we looked at the influence of the steric stabilizer (PVP) on nanoparticle fouling development during pore blocking and cake filtration stages.

Our work demonstrates that molecular mass, concentration of the steric stabilizer (PVP) and filtration pressure applied significantly influence pore blockage and cake filtration. Using a stabilizer with a lower molecular mass generally led to better stabilization of the nanoparticles and the stabilizer contributed less to the fouling. While higher concentrations of the stabilizer enhanced the stability of the nanoparticles, they also caused faster fouling development due to the higher total solute load. Stabilizer with a higher molecular mass was found to contribute more to pore blockage and lead to faster fouling development. Use of a higher transmembrane pressure resulted in compression of the filtration cake, resulting in improved nanoparticle rejection at the expense of permeability.

4.1. Introduction

The exponential growth of nanotechnology creates new sources of water pollution because engineered nanoparticles occur in many common products, such as pigments, coatings and cosmetics, nowadays and are eventually released into the aqueous environment [1-3]. Water pollution with nanoparticles is therefore expected to become an increasingly serious problem [4]. Although the number of studies into the effect of nanoparticles on living organisms is still low relative to their wide range of application, most researchers suggest that nanoparticles are toxic [5, 6] and that their small size allows easy penetration into organs and cells [7]. Therefore, reliable technologies for nanoparticle removal from water sources are needed.

Membrane technology is effective in the removal of much larger colloidal particles, but not much is known about the filtration of engineered nanoparticles yet [8, 9]. Up-to-date the application of membrane technology is limited by fouling [10] causing pore constriction and internal fouling; this usually necessitates the use of sophisticated cleaning procedures [11-13]. Therefore, it is important to determine the mechanisms, factors and parameters that influence nanoparticle fouling in the initial fouling stage to enable the development of filtration strategies that minimize fouling.

Key factor in the development of fouling is the tendency of the nanoparticles to aggregate [14-16]. The stability of aqueous suspensions of nanoparticles depends on the nanoparticles' surface chemistry, the aquatic environment (pH, ionic strength), and on interactions with other compounds present in the solution [17]. Often, steric or electrostatic stabilizers are added to nanoparticle suspensions to keep the nanoparticles dispersed [18]. Steric stabilization is one of the most commonly used and studied forms of stabilization. Steric repulsion occurs after adsorption of a neutral polymer such as polyvinylpyrrolidone or polyethylene oxide onto the nanoparticle surface and prevents aggregation of nanoparticles. Other organic macromolecules, like humic substances, proteins or saccharides, which are present in many water sources, can also act as steric stabilizers [19-21]. As adsorption of such natural macromolecules leads to transformation of the nanoparticles' surface characteristics and the resulting change in aggregation kinetics, it can facilitate their transport through porous media [22].

The interactions in such feed solutions containing macromolecules and nanoparticles are diverse and simple superposition of the individual fouling contributions cannot be used to describe membrane fouling development in such cases [22]. On the one hand, the higher stability due to steric stabilizers reduces near-membrane surface aggregation as a result of concentration polarization of the rejected nanoparticles [23]. This reduced

aggregation of nanoparticles facilitates their transport through the porous membrane structure as individual particles and fouling decreases as the result of the formation of a porous cake [24, 25]. On the other hand, the stabilizers themselves can be foulants; they can be retained by the membrane, increasing the thickness of the fouling layer, meanwhile also reducing the porosity of the formed filtration cake by filling the voids between the nanoparticles in the cake [26-28]. Furthermore, polymeric stabilizers may lead to more severe pore clogging due to flocculation bridging, which increases the size of the nanoparticles. Moreover, steric stabilization may not prevent nanoparticles from depositing on the membrane surface either [29]. Therefore, the presence of stabilizers may well result in a higher filtration resistance.

To date, however, there have been no systematic studies of the role of polymeric steric stabilizers during membrane filtration of engineered nanoparticles as far as we know. Therefore, the aim of the research we report here was to determine the effect of steric stabilizers (in this case, polyvinylpyrrolidone (PVP)) on fouling and rejection during microfiltration of nanoparticles. The emphasis of the study was on concentration and chain length (molecular weight) of the PVP and on applied filtration pressure. Whether the stability of the suspension becomes increased or reduced is a function of stabilizer type, concentration and molecular mass (in addition to pH and ionic strength). These properties can therefore strongly affect filtration behavior. The idea behind our work was that combining rejection and permeability data with mixture properties would allow us to identify mechanisms involved in fouling and rejection during microfiltration of sterically stabilized nanoparticle suspensions.

4.2. Theory

4.2.1. Steric stabilization and flocculation

Steric stabilization of nanoparticle suspensions is a matter of finding and maintaining a delicate balance. Adsorption of the stabilizer onto the surface of nanoparticles changes their surface properties. At high enough polymer concentrations, this leads to the nanoparticles being covered with a dense polymer layer. Steric repulsion between polymer chains on the particle surfaces (Fig. 1a) prevents particle aggregation. On the other hand, at low polymer concentrations or with very long polymer chains (high molecular weight), a single polymer can adsorb onto more than one single nanoparticle. This so-called flocculation bridging (Fig. 1b) leads to the formation of

clusters of polymer chains and nanoparticles, effectively promoting the aggregation of the nanoparticles [30, 31].

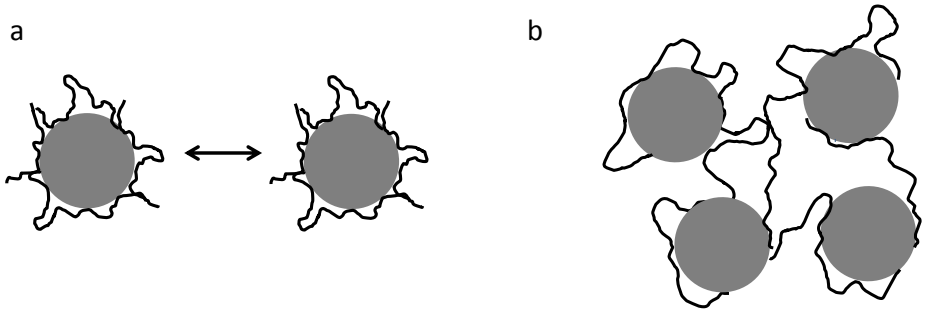

Fig. 1. Schematic representation of a) steric stabilization and b) flocculation bridging.

In solutions, there is always an equilibrium between the amount of adsorbed stabilizer and the bulk concentration of the stabilizer [32-34]. At increased concentrations of polymer in the bulk, more polymer chains adsorb onto the nanoparticles. As a result, the conformation of the adsorbed polymer chains changes, as schematically shown in Fig. 2. The trains conformation that occurs at lower polymer concentrations changes to a loops and tails conformation at higher polymer concentrations. The adsorbed polymer chains become more elongated and the nanoparticle size increment as a result of stabilizer adsorption is greater.

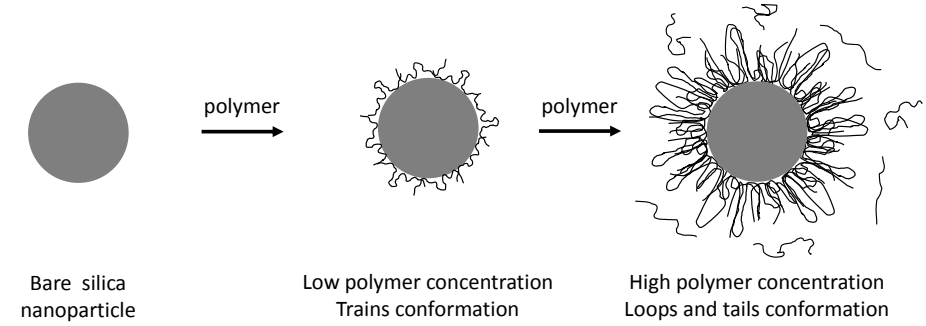

Fig. 2. Schematic representation of concentration-dependent conformation change of adsorbed polymer molecules (such as PVP) onto a silica nanoparticle surface (adapted from [34]).

4.2.2. Dead-end microfiltration of nanoparticles

In previous work [10], we found that constant pressure dead-end microfiltration of electrostatically stabilized suspensions of nanoparticles much smaller than the membrane pores takes place in the following stages: 1) adsorption, 2) free transport of the nanoparticles through pores, 3) pore blockage, 4) cake filtration, and 5) maturation of the cake. Since these filtration stages can only occur in a specific order and permeability decays at a different rate during each of these stages, they can be easily recognized in the filtration curve (Fig. 3a). Pore blockage and formation of the filtration cake, which acts as a secondary membrane, lead to a final nanoparticle rejection to about 90%, as visible in Fig. 3b.

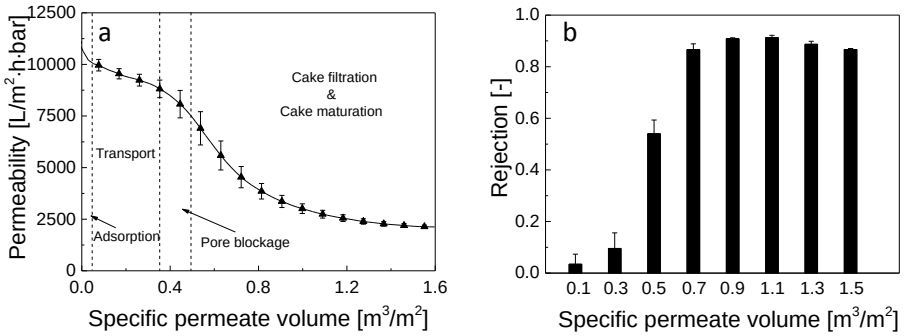

Fig. 3 (a) Permeability and (b) rejection of silica nanoparticles as a function of specific permeate volume during microfiltration of 2 mg/L of bare silica nanoparticles [10].

4.3. Experimental

4.3.1. Materials

Colloidal silica nanoparticles Ludox TM-50 with a diameter of about 25 nm [10] were used as model nanoparticles. We purchased three types of polyvinylpyrrolidone (PVP), each with a different molecular mass; their average molecular masses were 10 kDa, 40 kDa and 360 kDa (Sigma Aldrich supplier data). Aqueous solutions of ACS grade HCl or NaOH, and NaCl, (Sigma Aldrich) were used to adjust the pH and ionic strength of the solutions, respectively. All solutions were prepared with ultrapure water (Milli-Q, resistivity >18.2 MΩ·cm); all chemicals were used without further purification.

4.3.2. Feed solution characterization

The surface zeta potential of the nanoparticles and their mixtures with PVP were obtained by electrophoretic mobility measurements (Malvern ZetaSizer 3000Hsa). The measurements were carried out with a 50±1 mg/L nanoparticle suspension with pH 8, prepared by dilution of the stock silica suspension in Milli-Q water. The hydrodynamic diameter of the nanoparticles in the mixture with PVP was determined in batch mode with a DAWN-Heleos-8 Multi-Angle static Light Scattering (MALS) detector placed at an angle of 108°; a dynamic light scattering (DLS) apparatus (NanoStar, Wyatt Technology Corporation, USA) was connected via a glass fiber cord.

We used a fixed angle optical reflectometer equipped with a stagnant point flow cell to obtain information on the adsorption of PVP molecules to the silica surface [35]. For this purpose, we prepared 0.1 g/L PVP suspensions at 1 mM NaCl ionic strength and pH 8 and let them adsorb onto a piranha-treated silicon wafer with a ~75 nm SiO_2 top layer. A polarized light beam generated by a He-Ne laser (628 nm) hitting the wafer was reflected around the Brewster angle ($\theta = 71°$) to the detector. The detector measured the intensity of the parallel (R_p) and perpendicular (R_s) components of the light after the reflection from the surface. The ratio between R_p and R_s gives the measurement signal value S (-), which is directly proportional to the adsorbed amount Γ (mg/m^2) according to Eq. 1:

$$\Gamma = \frac{S - S_0}{S_0} \cdot Q \qquad (1)$$

where S_0 (-) is the baseline signal, and Q (mg/m^2) is an instrument- and material-dependent sensitivity factor. In order to estimate the sensitivity factor Q, we used an optical model, which was calculated with the aid of "Professor Huygens" software (Dullware Software). The input parameters for the model were the following: $\theta = 71°$, $n_{SiO2} = 1.46$, $n_{Si} = 3.85$, $n_{H2O} = 1.3327$,$d_{SiO2} = 75$ nm, $dn/dc = 0.175$ mL/g [36]. The calculated sensitivity factor Q was 27 mg/m^2 for all experiments. We repeated the reflectometry measurements three times for each molecular mass of PVP.

Asymmetric flow field flow fractionation (AF4) in combination with light scattering (LS) and differential refractive index measurements (dRI) enabled us to extract detailed information about the composition of the feed solutions. The AF4 setup separates colloidal suspensions into fractions, and directly measures the concentration and size of the species in each fraction [37]. Fig. 4 shows a schematic diagram of our AF4 setup.

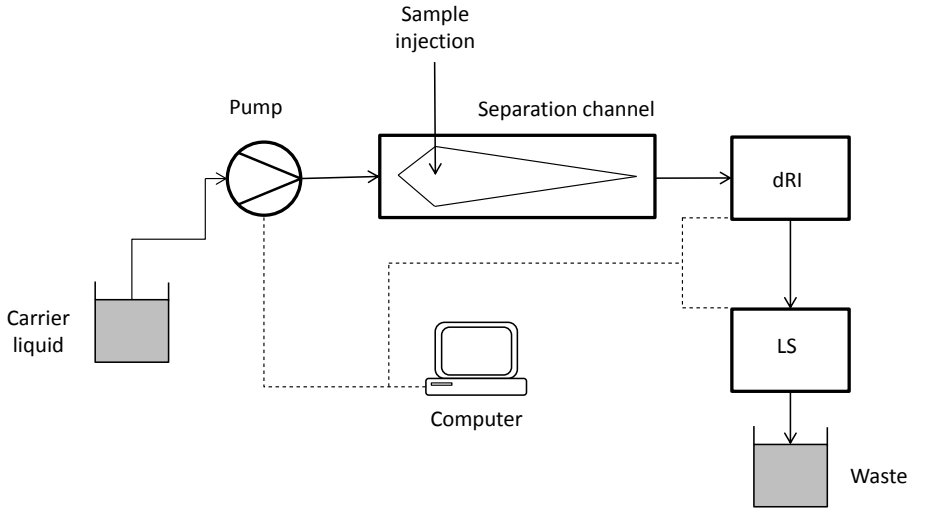

Fig. 4. Schematic representation of the asymmetric flow field flow fractionation setup used in the fractionation and subsequent characterization of PVP-silica nanoparticle mixtures in terms of size and concentration (dRI = differential refractive index; LS = light scattering).

A detailed explanation of the principles behind this method can be found elsewhere [37]. Briefly, the AF4 channel fractionates particles according to their size as described by Eq. 2:

$$t_r = \frac{\pi \eta t_v w^2 \phi_x}{kTV_c} \cdot r_h \qquad (2)$$

Here, t_r is retention time (s), t_v is the retention time of the void peak (s), w is the height of the channel (m), ϕ_x is the applied cross-flow (m^3/s), V_c is the volume of the channel (m^3), η is the viscosity (Pa·s), T is the temperature (K), k is the Boltzmann constant ($1.38 \cdot 10^{-23}$ J/K), and r_h is the hydrodynamic radius (m). Eq. 2 means that in the ideal case, i.e. in the absence of particle-membrane interactions, the nanoparticle elution time is proportional to nanoparticle size.

After fractionation, the nanoparticles were further characterized with the aid of a light scattering detector and dRI detector, which measured size and concentration of the fractions, respectively. Scattering of light is due to the optical inhomogeneity of suspensions. The intensity of the scattered light is given by the Rayleigh equation:

$$i_\theta = I_0 (n_d^2 - n_m^2) \frac{2\pi^2 N v^2}{l^2 \lambda_0^4} \qquad (3)$$

Here, i_θ is the light scattering intensity at angle θ (W/m^2), I_0 is the intensity of the incoming light (W/m^2), n_d and n_m are the refractive index of particle and medium, respectively, l is the detector distance from the beam (m), N is the number of particles per cubic meter of scattering volume (particles/m^2), where each particle has a volume v (m^3), and λ_0 is the wavelength (nm). The Rayleigh equation predicts that light scattering depends strongly on particle radius r as $v^2 \sim r^6$. We report our light scattering data in terms of the Rayleigh ratio R_θ (1/cm):

$$R_\theta = \frac{i_\theta}{I_0} l^2 \qquad (4)$$

This can be regarded as the relative light scattering per steradian.

For the AF4 experiments, the Eclipse 2 AF4 system (Wyatt Technology Europe GmbH, Germany) was connected to an Agilent 1100 HPLC isocratic pump and a micro-vacuum degasser (Agilent Technologies, Inc.). The fractionation of the nanoparticle mixtures took place in a short fractionation channel (channel length = 152 mm; maximal channel width = 11.5 mm) equipped with a 5 kDa regenerated-cellulose flat sheet membrane (Microdyn-Nadir GmbH, Germany) and a laser-cut spacer with a thickness of 350 µm. The AF4 system was connected in-line with an Optilab rEX variable differential RI (dRI) detector (Wyatt Technology Corporation, USA) and a DAWN Heleos-8 multi-angle light scattering (MALS) instrument (Wyatt Technology Corporation, USA). The DAWN-Heleos-8 instrument was placed at an angle of 108°, where a dynamic light scattering (DLS) apparatus (NanoStar, Wyatt Technology Corporation, USA) was connected via a glass fiber cord. We operated the MALS and dRI detectors at a laser wavelength of 658 nm. All data logging and calculations were performed by Astra 6.1 software (Wyatt Technology Corporation, USA).

Table 1 details our AF4 operating procedure for fractionating mixtures of silica nanoparticles and PVP molecules. We used a channel flow of 1 mL/min and an injection flow of 0.2 mL/min. To obtain reasonable retention times and because of the different molecular weights of the PVP, we had to apply different cross-flow rates V_x; for 10 kDa and 40 kDa PVP, we used a cross-flow of 0.8 mL/min, whereas a cross-flow of 0.2 mL/min was chosen for 360 kDa PVP. Because of the AF4 detection limits, the concentrations of silica nanoparticles and PVP were higher in the AF4 experiments than in the filtration experiments, but the concentration ratios were the same.

Table 1. AF4 fractionation method for characterization of the silica nanoparticles and PVP solutions, where t is time of the experiment (min), Δt is duration of the step (min), V_{x0} is initial cross-flow (mL/min), and V_{xe} is final cross-flow. Inj. = injection and between brackets is the cross-flow rate for 360 kDa PVP.

Step	t [min]	Δt [min]	Mode	V_{x0} [mL/min]	V_{xe} [mL/min]	Focus flow [mL/min]
1	0	2	Elution	0.8 (0.2)	0.8 (0.2)	-
2	2	1	Focus	-	-	1.5
3	3	4	Focus+Inj.	-	-	1.5
4	7	1	Focus	-	-	1.5
5	8	50	Elution	0.8 (0.2)	0.8 (0.2)	-

4.3.3. Membrane and membrane characterization

We used commercially available inside-out PES-PVP microfiltration (MF) hollow-fiber membranes Pentair X-Flow 1.5MF02 (Pentair X-Flow BV, the Netherlands). One membrane fiber was potted in a PVC tube with two component polyurethane glue 2K Expert (Bison International B.V., the Netherlands) to give a final filtration area of 2.5 cm^2. The clean-water permeability of the membrane was determined as $11 \cdot 10^3$-$12 \cdot 10^3$ $L/m^2 \cdot h \cdot bar$. The average pore diameter of the membrane was measured with a Porolux™ 1000 (POROMETER nv) using Porefil Wetting Fluid (supplied by POROMETER nv) as pore-filling liquid. A SurPASS electrokinetic analyzer (Anton Paar GmbH) was used to determine the zeta potential of the inner surface of the membrane, with a 5 mM KCl solution as electrolyte. The zeta potential was calculated according to the Fairbrother-Mastin equation.

4.3.4. Filtration experiments and data processing

All filtration experiments were carried out in a constant pressure filtration setup as depicted in Fig. 5.

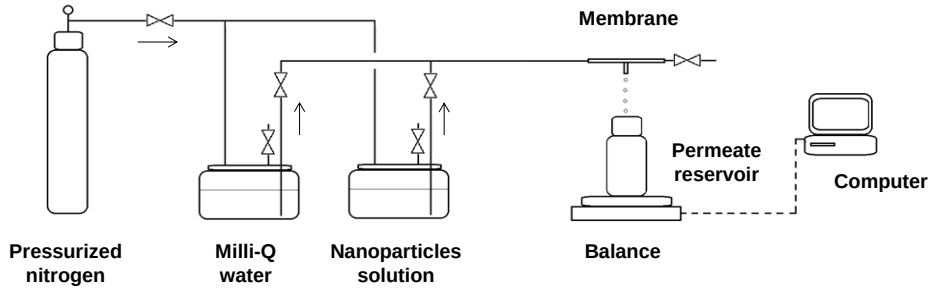

Fig. 5. Flow sheet of the used constant pressure filtration setup.

A constant pressure of either 0.1 bar, 0.2 bar or 0.4 bar was applied as driving force in the filtration experiments, using pressurized nitrogen. Each filtration experiment consisted of two steps. Firstly, 50 mL of Milli-Q water was filtered through the membrane module to obtain a stable clean-water flux. Secondly, after filtration of 50 mL of Milli-Q water, we connected the nanoparticles solution vessel to the membrane module by opening the valve. During each filtration experiment, 400 mL of a feed solution was filtered. The cumulative mass increment of the permeate was monitored continuously by an analytical balance connected to the computer. The permeability was calculated according to Eq. 5:

$$L_P = \frac{J}{\Delta P} \tag{5}$$

where L_P is the liquid permeability (L/m^2·h·bar), J is the flux (L/m^2·h) and ΔP is the transmembrane pressure (bar). Permeate samples were collected every 50 mL for ICP-MS analysis (Thermo Fisher Xseries 2). We calculated rejection of the silica nanoparticles according to Eq. 6:

$$\sigma = 1 - \frac{C_p}{C_f} \tag{6}$$

where σ is the rejection (-), C_P is the concentration of the nanoparticles in the permeate sample (mg/L), and C_f is the concentration of the nanoparticles in the feed solution (mg/L).

We prepared Milli-Q water solutions with pH 8 and containing 1 mM NaCl, 2 mg/L of silica nanoparticles and different concentrations of PVP. Three types of PVP,

each with a different molecular mass (10 kDa, 40 kDa and 360 kDa), were used in this study to evaluate the effect of PVP chain length on filtration and fouling during filtration of silica nanoparticle suspensions. To determine the role of the PVP concentration in the fouling behavior, we also used different concentrations of PVP in the feed solution for each molecular mass of the polymer (1 mg/L, 2 mg/L and 4 mg/L). The effect of transmembrane pressure on filtration performance was evaluated by application of lower (0.1 bar) and higher (0.4 bar) transmembrane pressures, in addition to the standard 0.2 bar.

4.4. Results and discussion

The results and discussion section consists of two subsections. In the first subsection, we describe the detailed characterization of the membrane and the feed solutions. With regard to the feed solutions, it is especially important to understand how the presence of the stabilizing polymer influences the stability of the nanoparticle suspension. In the second subsection, we discuss the filtration experiments performed with the described feed solutions. The observations described in the first subsection enable the interpretation of the results reported in the second subsection.

4.4.1. Characterization of membrane and feed solutions

4.4.1.1. Membrane

Table 2 lists the experimentally obtained properties of the MF membrane. The average pore diameter of this membrane as measured with capillary flow porometry (CFP) is 200 ± 15 nm. Streaming potential measurements showed that the inner surface of the membrane was negatively charged at pH 8 and had a zeta potential of -23.1 ± 2.1 mV.

Table 2. Properties of the used membrane.

Membrane				
Type	Material	Clean water permeability [$L/m^2 \cdot h \cdot bar$]	Pore size [nm]	Zeta potential at pH 8 [mV]
Pentair X-Flow 1.5MF02	PES/PVP	11500 ± 500	200 ± 15	-23.1 ± 2.1

4.4.1.2. Stabilizers and nanoparticles

Table 3 lists the characteristics of the nanoparticles and PVP stabilizers. Similar to the membrane surface, the surface of the nanoparticles also is negatively charged at pH 8 (-36 ± 1.2 mV) because of the silanol groups of these silica particles [38].

Table 3. Properties of the used silica nanoparticles and PVP stabilizers.

Nanoparticles			
Type	Diameter [nm]	Surface area * [m^2/L]	Zeta potential at pH 8 ** [mV]
Ludox TM-50	25 ± 5.2 [10]	0.28	-36 ± 1.2
Stabilizers			
Type	M_w * [kDa]	Hydrodynamic diameter [nm]	Adsorption to silica ** [mg/m^2]
PVP10	10	4.3 [39]	0.64 ± 0.1
PVP40	40	10.2 [39]	0.62 ± 0.09
PVP360	360	39.9 [39]	0.67 ± 0.1

*Manufacturer's data
**Experimental data

PVP molecules are able to adsorb onto a silica surface via the formation of hydrogen bonds between the silanol groups and the PVP monomers [36, 40]. The reflectometer data in Table 3 confirm the adsorption of PVP onto the silica surface for the pH and ionic strength used in this investigation. Fig. 6a shows the zeta potential of the nanoparticles as a function of the PVP concentration. For all three used molecular masses of PVP, the zeta potential becomes less negative with increasing PVP concentration. As a layer of polymer forms on the nanoparticles, the shear plane at which the zeta potential is measured moves away from the particle interface. Although the actual surface charge of the particle remains unchanged, adsorption of the PVP molecules screens strong negative surface charge of the silanol groups on the nanoparticle surface. Furthermore, the greater distance to the shear plane means a less negative zeta potential. The higher the molecular mass of the PVP, the smaller the zeta potential, indicating the presence of a thicker polymer layer on the nanoparticle surface [41]. Fig. 6b shows a similar trend for the change in hydrodynamic diameter of the nanoparticles with PVP concentration. The diameter increases with increasing PVP concentration, and this is more pronounced for higher molecular masses of PVP.

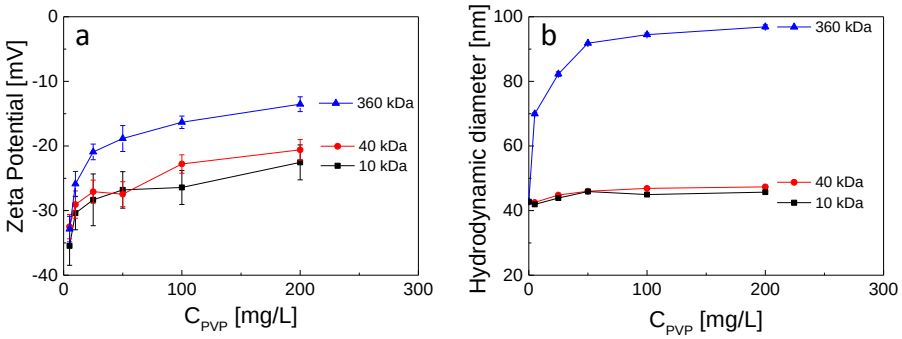

Fig. 6. (a) Zeta potential and (b) hydrodynamic diameter of silica nanoparticles as a function of PVP concentration and PVP molecular mass.

4.4.1.3. Asymmetric flow field flow fractionation of the feed solutions

The properties of the stabilizer adsorbed onto the silica nanoparticles determine the stability of the nanoparticles in the suspension, and hence the nanoparticles' filtration behavior. As Fig. 6 illustrates, molecular mass and concentration of the PVP stabilizer change the nanoparticles' properties, and as a result can alter fouling development. However, measurements of zeta potential and hydrodynamic diameter in the bulk do not give complete information about the number of solute fractions present in the solution, their sizes and their concentrations. In view of the importance of nanoparticle size, size distribution and stability and to be able to correlate the filtration behavior of silica nanoparticles with the role of the PVP stabilizer, obtaining detailed information about concentration and size of the solute fractions is essential. For that reason, we fractionated the silica-PVP mixtures by using the AF4 technique, followed by a detailed characterization of the obtained fractions.

Fig. 7 displays chromatograms for the fractionated solutions containing 50 mg/L of silica nanoparticles and PVP. Figs. 7a and 7b give results for mixtures with 10 kDa PVP; Figs. 7c and 7d show results for mixtures with 40 kDa PVP. For the solutions containing 360 kDa PVP (Figs. 7e and 7f), we reduced the applied cross-flow velocity to 0.2 mL/min (see Table 1) to obtain reasonable elution times. For this reason, we cannot compare these chromatograms directly with those for 10 kDa and 40 kDa PVP solutions, so we discuss the results for 360 kDa PVP separately.

The Rayleigh ratio, which is plotted in Fig. 7a, increased after the addition of 10 kDa PVP to the nanoparticle suspension, suggesting an increase of the nanoparticles' diameter. However, the shape of the chromatogram peaks for bare nanoparticles is the same as for nanoparticles coated with 10 kDa PVP molecules, which implies that both

solutions had a comparable size distribution. Furthermore, as Fig. 7a shows, increasing the 10 kDa PVP concentration only led to a slight increase of the elution time (linearly related to nanoparticle size; see Eq. 2). This suggests that the nanoparticle size barely increased and that nanoparticle aggregation remained very limited when 10 kDa PVP was added. These findings are supported by Fig. 6b, which shows that adsorption of 10 kDa PVP led only to a slight increase of the hydrodynamic diameter.

On the other hand, Fig. 7c clearly demonstrates that the elution time for silica nanoparticles increased with increasing amount of added 40 kDa PVP. Adsorption of 40 kDa PVP molecules resulted in a marked increase of the radius of the nanoparticles, and this increase was larger with increasing polymer concentration. When comparing Figs. 7a and 7c, we can see that the hydrodynamic radius of the nanoparticles (as deduced from the nanoparticle elution time) increased more with increasing concentration when longer polymer chains were added. The static light scattering results obtained for 10 kDa PVP and 40 kDa PVP (Figs. 7a and 7c), dRI chromatograms (Figs. 7b and 7d) and dynamic light scattering results (Fig. 6b) suggest the conformational change of adsorbed PVP chains as described in Section 4. 2.1 and Fig. 2. As a result, slightly longer elution times were needed for a higher concentration and higher molecular mass of the polymer.

In Figs. 7b and 7d, the differential refractive index is plotted as a function of elution time for mixtures of silica nanoparticles and 10 kDa and 40 kDa PVP, respectively. For each PVP-silica nanoparticle mixture, not one but two distinct peaks are visible. This is in contrast with the light scattering chromatograms (Figs. 7a and 7c), which show only one peak. The second, less intensive peaks in the two dRI chromatograms overlay the light-scattering peaks (Figs. 7a and 7c), which can be attributed to the silica nanoparticles. Similarly to LS peaks (Figs. 7a and 7c), elution time of this second peak increases with increasing PVP concertation (Figs. 7b and 7d). The first dRI peaks in Figs. 7b and 7d, which increase significantly with increasing concentration of PVP, represent unadsorbed PVP molecules since these peaks eluted at the same time as pure PVP. Furthermore, the area of these peak scales up linearly with increasing PVP concentration in the suspension. The presence of the two distinct peaks for mixtures of 10 kDa or 40 kDa PVP and silica nanoparticles proves the coexistence of two fractions: silica nanoparticles coated by PVP molecules and free, unadsorbed PVP molecules.

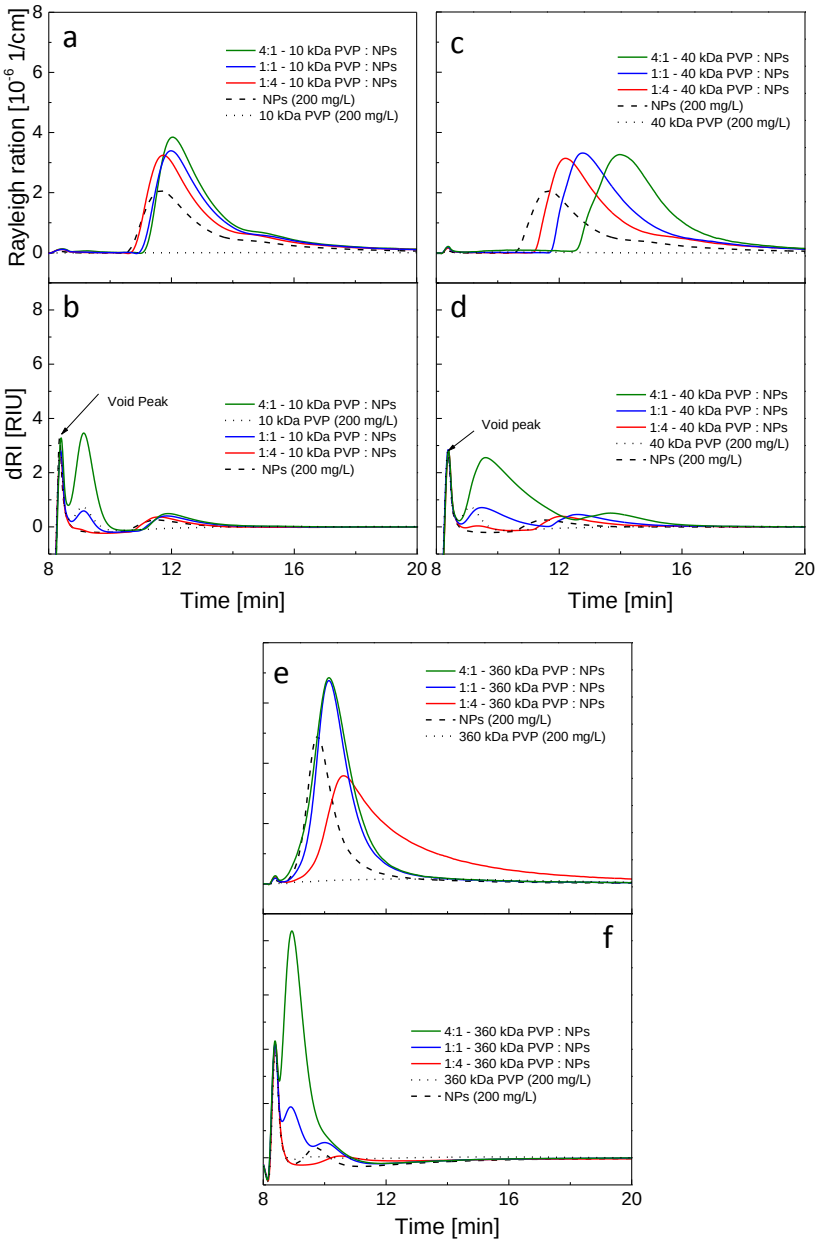

Fig. 7. Rayleigh ratio and differential refractive index (dRI) obtained for asymmetric flow field flow fractionation of silica nanoparticle – PVP mixtures. (a) Rayleigh ratio and (b) differential refractive index for 10 kDa PVP; (c) Rayleigh ratio and (d) differential refractive index for 40 kDa PVP; (e) Rayleigh ratio and (f) differential refractive index for 360 kDa PVP

In the case of 360 kDa PVP, a clear distinction between the nanoparticle and PVP peaks is only possible for the 1:1 concentration ratio. For the lowest concentration of 360 kDa PVP (50 mg/L, 1:4 ratio), the nanoparticle peak shifts to a longer elution time (Figs. 7e and 7f), suggesting the presence of larger nanoparticles. For a greater 360 kDa PVP concentration (200 mg/L, 1:1 ratio), two distinct peaks can be observed: first the polymer peak and then the nanoparticle peak. Furthermore, the mixture of nanoparticles and PVP molecules starts to elute faster with increasing concentration (Fig. 7e), the intensity of the peaks is higher, and the peaks are less broad than for the lowest concentration of PVP. We attribute this to a slight restabilization of the silica nanoparticles at the higher 360 kDa PVP concentrations. At lower 360 kDa PVP concentrations, the long polymer chains caused reversible flocculation bridging between the nanoparticles, which resulted in longer elution times. With further increased concentrations of 360 kDa PVP, more polymer was adsorbed to the nanoparticles and they became restabilized. In addition, as observed for 10 kDa and 40 kDa PVP, increased concentrations of 360 kDa PVP led to the first dRI peak becoming larger, indicating a higher concentration of free polymers (Fig. 7f).

To summarize, the AF4 results clearly show that our PVP-silica nanoparticle mixtures consisted of two fractions, namely PVP-coated nanoparticles and free unadsorbed polymer chains. With increased PVP concentrations, more polymer adsorbed on the surface of the nanoparticles, resulting in an increase in nanoparticle size (hydrodynamic diameter). This increase was greater for higher molecular masses of the PVP. Furthermore, higher PVP concentrations led to a higher concentration of unadsorbed polymer chains. No aggregation of nanoparticles was observed for all used concentrations of 10 kDa PVP and 40 kDa PVP. In the case of 360 kDa PVP, flocculation bridging appeared to occur when the concentration was 50 mg/L of PVP (1:4 ratio).

In view of the limited aggregation and only slight increase of the nanoparticle diameter in the mixtures with 10 kDa PVP and 40 kDa PVP, we do not expect increased pore blockage and nanoparticle rejection to occur during filtration of those mixtures. On the other hand, at higher PVP concentrations, the presence of free PVP polymer chains might contribute to pore blockage and densification of the cake layer. For 360 kDa PVP, pore blockage might occur faster due to flocculation bridging and the higher molecular mass of the polymer.

4.4.2. Filtration experiments

4.4.2.2. Filtration of nanoparticles and low-molecular-weight PVP stabilizer

We first investigated the influence of the concentration of 10 kDa PVP stabilizer on dead-end microfiltration of the silica nanoparticles. Fig. 8 summarizes the filtration results. Fig. 8a shows that for bare nanoparticles without added PVP (the lowest line), the permeability decreased significantly during the course of filtration. Fouling developed in the five stages as described in Section 4.2. The general shape of the filtration curves obtained with addition of 10 kDa PVP is comparable to this for bare silica nanoparticles. After adding 4 mg/L 10 kDa PVP without nanoparticles, the permeability decreased by about 20% compared with the initial permeability and distinct fouling stages could no longer be observed. This difference in fouling behavior of silica nanoparticles and 10 kDa PVP is related to their size difference (see Table 3).

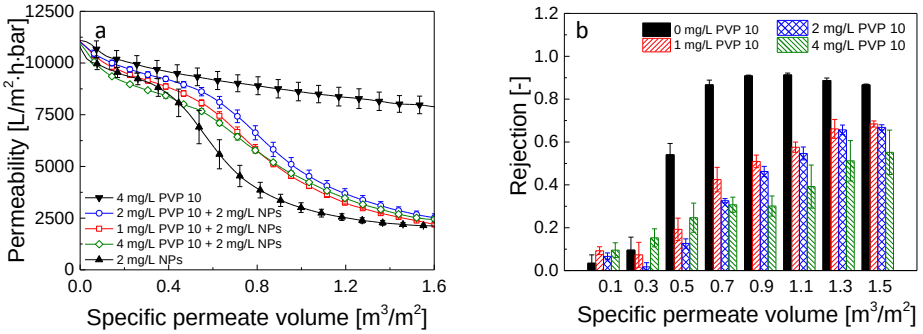

Fig. 8. (a) Permeability and (b) nanoparticle rejection as a function of specific permeate volume during filtration of 2 mg/L of silica nanoparticles with various concentrations of 10 kDa PVP at a transmembrane pressure of 0.2 bar.

However, as also visible in Fig. 8a, even the addition of a small amount of 10 kDa PVP (1 mg/L) to the nanoparticle suspension already extended the duration of nanoparticle transport through the membrane pores (stage 2), and pore blockage was initiated later. As Table 4 shows, the estimated blocking point (point at which pore blocking starts) [10] for 1 mg/L of 10 kDa PVP occurred after about 0.31 ± 0.01 m^3/m^2. For bare nanoparticles, this was 0.23 ± 0.03 m^3/m^2. The duration of the nanoparticle transport stage was even longer for 2 mg/L of 10 kDa PVP (0.35 ± 0.02 m^3/m^2). However, it shortened when the concentration of 10 kDa PVP stabilizer increased to 4 mg/L; pore blocking then started after about 0.23 ± 0.02 m^3/m^2.

Table 4. Blocking points (V_{block}) describing transition between transport stage and pore blockage stages for bare and PVP coated nanoparticles (na = not available due to instantaneous pore blocking).

PVP Concentration [mg/L]		0	1	2	4
V_{block} [m^3/m^2]	10 kDa	0.23 ± 0.03	0.31 ± 0.01	0.35 ± 0.02	0.23 ± 0.02
	40 kDa		0.21 ± 0.01	0.31 ± 0.02	0.25 ± 0.04
	360 kDa		*na*	*na*	*na*

The longer transport stage observed with a higher specific permeate volume at the blocking point V_{block} for 1 mg/L and 2 mg/L 10 kDa PVP coated nanoparticles can be explained by enhanced nanoparticle stabilization caused by adsorption of the short PVP chains. High stability of the nanoparticles reduces their near-membrane-surface aggregation induced by the convective drag force, so maintaining a dispersed state of nanoparticles and consequently it takes longer before pore blocking sets in. The stabilization effect of the polymer molecules increases with PVP concentration since coverage of the nanoparticle surface is higher [41]. During filtration, however, the free PVP molecules can also cause membrane fouling. In the case of 4 mg/L of 10 kDa PVP, the free PVP chains (detected by AF4; see Fig. 7b) clearly contributed to pore blockage; hence, the duration of the nanoparticle transport decreased to 0.23 ± 0.05 m^3/m^2.

During the pore blockage stage, rejection of the bare nanoparticles rose sharply from approx. 10% to approx. 90% for pure nanoparticles (see Fig. 8b, black columns). However, when 10 kDa PVP was present in the feed solution, rejection of the nanoparticles became significantly reduced and developed continuously to approx. 70% at the end of the filtration. The increased nanoparticle transport through the membrane pores and delayed pore blockage (see Table 4) with 10 kDa PVP addition led to lower nanoparticle rejection. This caused less accumulation of nanoparticles on the membrane; hence, assuming equal cake layer porosity, the cake layer was thinner. In addition, the presence of free 10 kDa PVP chains (see Fig. 7b) may have changed the packing order of the cake. McDonogh et al. [42] demonstrated that polydispersed suspensions of charged nanoparticles can form filtration cakes in which nanoparticle packing is not uniform. The voids, defects and channels in the filtration cake structure allow transport of nanoparticles through the cake, resulting in less nanoparticle rejection. In our case as well, the feed solution consisted of solutes, which differed in size (free polymer 10 kDa PVP chains and nanoparticles coated with 10 kDa PVP). The surface charges responsible

for nanoparticle repulsion were replaced here by steric repulsions introduced by 10 kDa PVP chains. In the same time, these polymer chains work against ordered packing of the cake. Furthermore, increasing the concentration of 10 kDa PVP caused less rejection of nanoparticles, as is visible in Fig. 6b, so the 10 kDa PVP chains clearly caused lower rejection.

4.4.2.3. Filtration of nanoparticles with added higher-molecular-weight PVP stabilizer

Figs. 9a and 9b display permeability and rejection data for filtration of silica nanoparticles with 40 kDa PVP as stabilizer, respectively. As in the experiments with 10 kDa PVP, the addition of 40 kDa PVP stabilizer influenced permeability decay and rejection of silica nanoparticles, but there are only minor differences with the 10 kDa case.

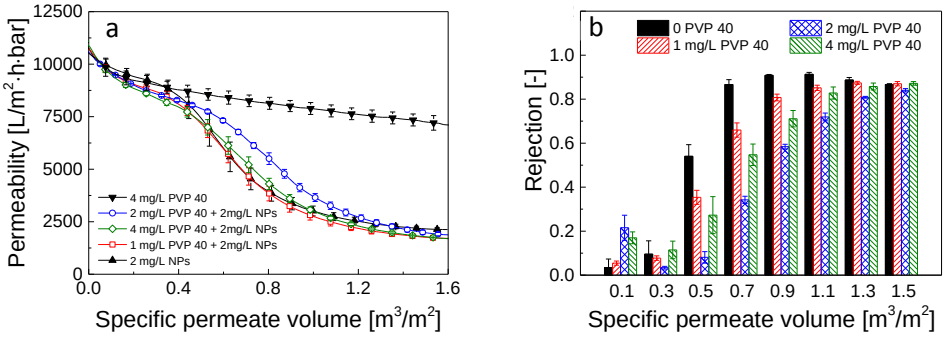

Fig. 9. (a) Permeability and (b) rejection of silica nanoparticles as a function of specific permeate volume during filtration of 2 mg/L of silica nanoparticles with various concentrations of 40 kDa PVP at a transmembrane pressure of 0.2 bar.

The initial stabilization (time until V_{block}) of the filtration curve in Fig 9a, signifying transport of the nanoparticles through the membrane pores, only lasted longer when 2 mg/L 40 kDa PVP was added (see Table 4). No effect on the permeability in this initial filtration stage was observed for 1 mg/L and for 4 mg/L of 40 kDa PVP. A synergic fouling effect of the nanoparticles and 40 kDa PVP molecules might explain this behavior. Firstly, the bulkier unadsorbed 40 kDa PVP molecules (diameter of about 10 nm; Table 3) may have contributed strongly to blockage of membrane pores. Secondly, adsorption of the longer 40 kDa PVP chains to silica nanoparticles caused a larger increase of the nanoparticle size than for 10 kDa PVP, as shown in Figs. 7c and. 7a, so

the difference between the nanoparticle diameter and the pore diameter became smaller. As a consequence, the pore blockage stage occurred sooner, despite the improved steric stabilization of the nanoparticles.

Similarly, as for 10 kDa PVP, rejection of silica nanoparticles became lower after addition of 40 kDa PVP to the feed solution (Fig. 9b). However, overall nanoparticle rejection was greater than with 10 kDa PVP (Fig. 8b). The 40 kDa PVP has longer polymer chains than 10 kDa PVP, and consequently may adsorb onto more than one nanoparticle in the filtration cake (bridging) [43]. This could lead to a more interconnected, more compact structure of the nanoparticle-PVP cake, across which silica nanoparticles cannot be transported that easily. Furthermore, with 40 kDa PVP, the pore blockage and cake filtration stages occurred earlier (see Fig. 9a) than with 10 kDa PVP (see Fig. 8a). Hence, more nanoparticles accumulated on the membrane surface over time, leading to a thicker deposit, in turn resulting in more rejection. This explanation is supported by the fact that delayed pore blockage in the case of 2 mg/L of 40 kDa PVP (Fig. 9a) results in a lower rejection of silica nanoparticles during the whole filtration process than with 1 mg/L and 4 mg/L 40 kDa PVP (Fig. 9b), pointing at a synergic effect.

Fig. 10a shows the permeability decay during filtration of silica nanoparticles with varying concentrations of 360 kDa PVP stabilizer. The 360 kDa PVP had an average hydrodynamic diameter almost twice as large (39.9 nm) as that of the silica nanoparticles (25 ± 5.2 nm). As Fig. 10a shows, this larger hydrodynamic diameter of PVP caused such a rapid permeability decay due to pore blockage, even for pure polymer, that estimation of the blocking point (V_{block}) was impossible. After this immediate pore blockage, cake filtration took place. With the mixtures of 360 kDa PVP and silica nanoparticles, fouling developed even faster and was more severe than with pure polymer or bare nanoparticles. Higher polymer concentrations caused faster pore blockage and a stronger reduction of the permeability during cake filtration because these higher concentrations of 360 PVP significantly increased nanoparticle size (see Fig. 6b). Additionally, the less negative zeta potential (Fig. 6a) and the higher polymer load did likely result in a thicker and more compact nanoparticle deposit [44].

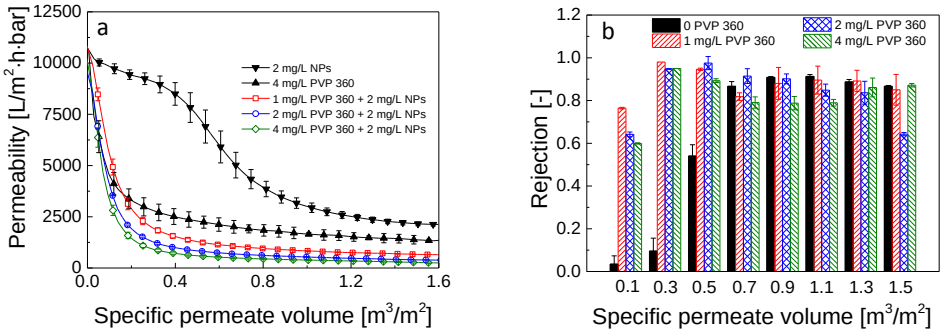

Fig. 10. (a) Permeability and (b) rejection of silica nanoparticles as a function of specific permeate volume during filtration of 2 mg/L of silica nanoparticles with various concentrations of 360 kDa PVP at a transmembrane pressure of 0.2 bar.

Fig. 10b makes clear that nanoparticle rejection during filtration with 360 kDa PVP was very high (60-80%), even for the first permeate sample. However, there was a slight reduction of this rejection later. This is surprising since we would expect a very high rejection of nanoparticles after the instantaneous pore blockage, and a very low permeability in the later filtration stage. One possible explanation for the decrease in rejection might be extensive concentration polarization occurring inside the fiber from the beginning of the filtration.

4.4.2.4. Role of transmembrane pressure

The applied transmembrane pressure can play an important role in the filtration of the silica nanoparticles – PVP mixtures, leading to a more compact or a more porous nanoparticle deposit. Therefore, the role of the polymeric stabilizers in the formation of nanoparticle deposits and rejection of nanoparticles may be different at different transmembrane pressures.

Fig. 11 shows permeability and rejection of bare silica nanoparticles for different transmembrane pressures. With a higher transmembrane pressure (0.4 bar) than the reference pressure of 0.2 bar, the flux declined faster in the first fouling stage (Fig. 11a), which can be explained by accelerated nanoparticle aggregation due to a higher convective drag force. Furthermore, this higher drag force compresses the filtration cake, thereby reducing cake porosity, leading to a significantly lower flux at the end of the filtration process. On the other hand, use of a lower transmembrane pressure (0.1 bar) did not significantly affect the duration of the initial nanoparticle transport and pore

blockage stages. It enabled maintaining a constant and much higher flux in the cake filtration stage, due to less compression of the cake and thus a more open cake structure. Unexpectedly, differences in the applied transmembrane pressure and the resulting fluxes did not influence rejection of the nanoparticles after formation of the filtration cake, as shown in Fig. 11b. The rejection of nanoparticles for all applied pressures was about 90% from the fourth permeate sample onward (0.7 m^3/m^2 specific permeate volume). Apparently, the highly ordered structure of the filtration cake, due to the high monodispersity of the nanoparticles and the strong repulsion among them, did not allow nanoparticle transport, even for very open cake structures (e.g. at 0.1 bar, in our experiments) [42].

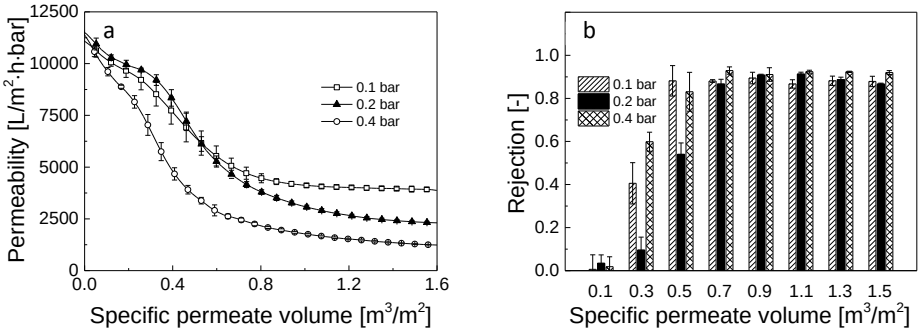

Fig. 11. (a) Permeability and (b) rejection of bare silica nanoparticles as a function of specific permeate volume during filtration of 2 mg/L bare silica nanoparticles (no PVP) at various transmembrane pressures.

When we carried out the filtration at a pressure of 0.4 bar (see Fig. 12a), the addition of 1 mg/L or 2 mg/L 10 kDa PVP had the same stabilization effect as with a pressure of 0.2 bar (see Section 4.2.2), allowing longer transport of nanoparticles through the membrane pores. Addition of 4 mg/L of 10 kDa PVP caused faster pore blockage, and rejection of the nanoparticles was reduced with increasing 10 kDa PVP concentrations (see Fig 12b), as was the case with 0.2 bar. However, at the end of the filtration test, rejection of the nanoparticles reached values of about 80-90%, which is higher than obtained with 0.2 bar (see Fig. 8b). This higher rejection can be explained by the before-mentioned cake compaction effect of higher transmembrane pressures.

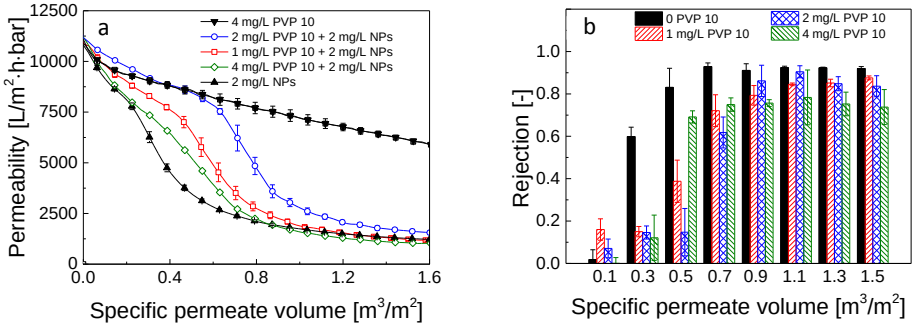

Fig. 12. (a) Permeability and (b) rejection of silica nanoparticles as a function of specific permeate volume during filtration of 2 mg/L of silica with various concentration of 10 kDa PVP at a transmembrane pressure of 0.4 bar.

At a transmembrane pressure of 0.1 bar, adding 10 kDa PVP to the silica nanoparticles had a clear impact on fouling development (Fig. 13a). The initial stabilization of the permeability (related to the nanoparticle transport through pores) was less pronounced or did not occur at all. We conclude that the pore blockage stage occurred immediately, since there was no transport stage. This is the result of the lower filtration-driving force at this pressure, which means that the contact time between the nanoparticles and PVP molecules in the concentration polarization zone on the membrane surface was longer. As a result, there was more time for adsorption of PVP molecules onto the nanoparticles at lower 10 kDa PVP concentrations (as visible in Figs. 6a and 7). In the nanoparticle deposit, this may have led to interconnection of nanoparticles by PVP chains [32, 33] via flocculation bridging (see Fig. 1b). This effect was less pronounced with higher 10 kDa PVP concentrations due to the higher coverage of the silica surface by polymer. Steric repulsion prevented flocculation bridging and no aggregation was observed, as can be deduced from Fig. 7a. Hence, for increasing 10 kDa PVP concentrations, we observed less permeability decay during the course of filtration (Fig. 13a). On the other hand, the lower zeta potential (Fig. 6a) and the increasing polymer concentration both led to a denser filtration cake. We therefore saw a significantly lower permeability at the end of the filtration with feed solutions containing PVP than with solutions containing bare nanoparticles. However, the nanoparticle deposit obtained with a transmembrane pressure of 0.1 bar was still more permeable for nanoparticles than the deposits obtained with 0.2 bar and 0.4 bar. The lower compaction of the cake and the lower packing order with increasing 10 kDa PVP concentration resulted in lower nanoparticle rejection (Fig. 13b).

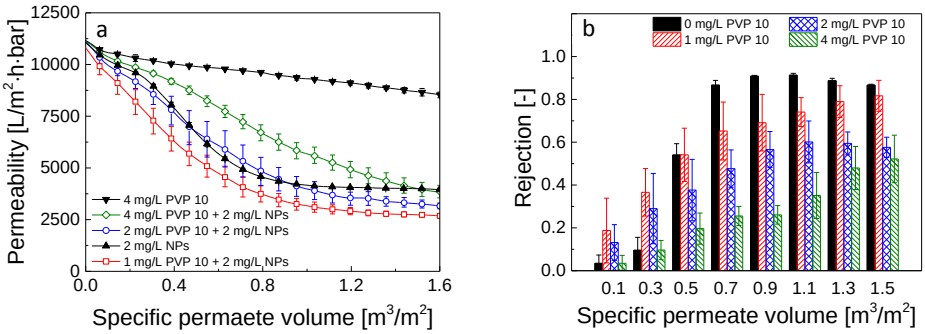

Fig. 13. (a) Permeability and (b) rejection of silica nanoparticles as a function of specific permeate volume during filtration of 2 mg/L of silica nanoparticles with various concentrations of 10 kDa PVP and a transmembrane pressure of 0.1 bar.

4.5. Conclusions

This experimental study investigated fouling and rejection during dead-end microfiltration of silica nanoparticles sterically stabilized with PVP polymers. Adsorption of PVP onto the nanoparticle surface changes nanoparticle interaction from electrostatic to steric. Characterization of our feed solutions by AF4 revealed the presence of two fractions, namely free PVP chains and sterically stabilized PVP-coated nanoparticles. Our research confirmed that fouling and rejection behavior of sterically stabilized nanoparticles is strongly determined by the properties of the used stabilizer (in our case, PVP), such as molecular mass and stabilizer concentration. Increasing the concentration of PVP stabilizer with a low molecular weight (10 kDa and 40 kDa) generally appears to result in a higher stability of the nanoparticles, and hence easier transportation of the nanoparticles through membrane pores, without aggregation. However, adding too much PVP stabilizer can result in a synergic fouling effect, where the effect of stabilization of nanoparticles is countered by the higher fouling contribution of the PVP stabilizer itself. Furthermore, nanoparticle rejection drops with increasing PVP stabilizer concentration, suggesting the formation of a more open and permeable cake structure. A higher molecular weight of the stabilizer results in a larger nanoparticle size and can also allow flocculation bridging. Consequently, pore blockage occurs faster and rejection of nanoparticles is greater. Moreover, the contribution of the PVP chains to fouling development increases with increasing molecular mass of the stabilizer. Finally, the transmembrane pressure also exerts control over the structure of the cake layer. Applying a higher transmembrane pressure results in a more compact cake structure,

which is less permeable for nanoparticles. Decreasing the transmembrane pressure results in a less dense cake layer; this lowers nanoparticle rejection.

References

[1] S. F. Hansen, E. S. Michelson, A. Kamper, P. Borling, F. Stuer-Lauridsen, A. Baun, Categorization framework to aid exposure assessment of nanomaterials in consumer products, Ecotoxicology 17 (2008) 438-47

[2] H. Weinberg, A. Galyean, M. Leopold, Evaluating engineered nanoparticles in natural waters, Trends. Anal. Chem. 30 (2011) 72-83

[3] P. Westerhoff, G. Song, K. Hristovski, M. A. Kiser, Occurrence and removal of titanium at full scale wastewater treatment plants: implications for TiO2 nanomaterials, J. Environ. Monitor. 13 (2011) 1195-203

[4] T. E. Abbott Chalew, G. S. Ajmani, H. Huang, K. J. Schwab, Evaluating nanoparticle breakthrough during drinking water treatment, Environ. Health. Perspect. 121 (2013) 1161-1166

[5] C. F. Jones, D. W. Grainger, In vitro assessments of nanomaterial toxicity, Adv. Drug Deliv. Rev. 61 (2009) 438-456

[6] N. Singh, B. Manshian, G. J. Jenkins, S. M. Griffiths, P. M. Williams, T. G. Maffeis, et al., NanoGenotoxicology: the DNA damaging potential of engineered nanomaterials, Biomaterials 30 (2009) 3891-3914

[7] C. Buzea, I. Pacheco, K. Robbie, Nanomaterials and nanoparticles: Sources and toxicity, Biointerphases 2 (2007) MR17-MR71

[8] K. M. Persson, G. Trägardt, G. Dejmek, Fouling behaviour of silica on four different microfiltration membranes, J. Membr. Sci. 76 (1993) 151-172

[9] S. Surawanvijit, H. H. Liu, M. Kim, Y. Cohen, Removal of metal oxide nanoparticles from aqueous suspensions, Separ. Sci.Technol. 49 (2014) 161-170

[10] K. Trzaskus, A. J. B. Kemperman, K. Nijmeijer, Towards controlled fouling and rejection in dead-end microfiltration of nanoparticles - role of electrostatic interactions, J. Membr. Sci. 496 (2015) 174-184

[11] M. Palencia, B. L. Rivas, H. Valle, Size separation of silver nanoparticles by dead-end ultrafiltration: Description of fouling mechanism by pore blocking model, J. Membr. Sci. 455 (2014) 7-14

[12] S. F. Sweeney, G. H. Woehrle, E. Hutchison, Rapid purification and size separation of gold nanoparticles via diafiltration, J. Am. Chem. Soc. 128 (2006) 3190-3197

[13] A. Grenier, M. Meireles, P. Aimar, P. Carvin, Analysing flux decline in dead-end filtration, Chem. Eng. Res. Des. 86 (2008) 1281-1293

[14] P. Aimar, P. Bacchin, Slow colloidal aggregation and membrane fouling, J. Membr. Sci. 360 (2010) 70-76

[15] D. Jassby, S. R. Chae, Z. Hendren, M. Wiesner, Membrane filtration of fullerene nanoparticle suspensions: effects of derivatization, pressure, electrolyte species and concentration, J. Colloid Interface Sci. 346 (2010) 296-302

[16] T. Yin, H. W. Walker, D. Chen, Q. Yang, Influence of pH and ionic strength on the deposition of silver nanoparticles on microfiltration membranes, J. Membr. Sci. 449 (2014) 9-14

[17] J. Labille, J. Brant, Stability of nanoparticles in water, Nanomedicine 5 (2010) 985-998

[18] Y. Liang, N. Hilal, P. Langston, V. Starov, Interaction forces between colloidal particles in liquid: theory and experiment, Adv. Colloid Interface Sci. 134-135 (2007) 151-166

[19] A. H. Taheri, L. N. Sim, C. T. Haur, E. Akhondi, A. G. Fane, The fouling potential of colloidal silica and humic acid and their mixtures, J. Membr. Sci. 433 (2013) 112-120

[20] A. I. Schäfer, U. Schwicker, M. M. Fischer, A. G. Fane, T. D. Waite, Microfiltration of colloids and natural organic matter, J. Membr. Sci. 171 (2000) 151-172

[21] A. S. Kim, A. E. Contreras, Q. Li, R. Yuan, Fundamental mechanisms of three-component combined fouling with experimental verification, Langmuir 25 (2009) 7815-7827

[22] X. Shi, R. Field, N. Hankins, Review of fouling by mixed feeds in membrane filtration applied to water purification, Desalin. Water Treat. 35 (2011) 68-81

[23] K. L. Chen, M. Elimelech, Influence of humic acid on the aggregation kinetics of fullerene (C60) nanoparticles in monovalent and divalent electrolyte solutions, J. Colloid Interface Sci. 309 (2007) 126-134

[24] Y. Chen, H. Kim, Monte Carlo simulation of pore blocking and cake formation by interfacial interactions during membrane filtration, Desalination 233 (2008) 258-266

[25] W. M., Two-dimensional stochastic modeling of membrane fouling, Sep. Purif. Technol. 24 (2001) 375–387

[26] A. E. Contreras, A. Kim, Q. Li, Combined fouling of nanofiltration membranes: Mechanisms and effect of organic matter, J. Membr. Sci. 327 (2009) 87-95

[27] D. Jermann, W. Pronk, R. Kagi, M. Halbeisen, M. Boller, Influence of interactions between NOM and particles on UF fouling mechanisms, Water Res. 42 (2008) 3870-3878

[28] D. Jermann, W. Pronk, M. Boller, Mutual influences between natural oganic matter and inorganic particles and their combined effect on ultrafiltration membrane fouling, Environ. Sci. Technol. 42 (2008) 9129–9136

[29] S. Lin, Y. Cheng, J. Liu, M. R. Wiesner, Polymeric coatings on silver nanoparticles hinder autoaggregation but enhance attachment to uncoated surfaces, Langmuir 28 (2012) 4178-4186

[30] J. Swenson, M. V. Smalley, H. L. M. Hatharasinghe, Mechanism and strength of polymer bridging flocculation, Phys. Rev. Lett. 81 (1998) 5840-5843

[31] K. Mühle, Particle adhesion in coagulation and bridging flocculation, Colloid Polym. Sci. 263 (1985) 660-672

[32] J. M. H. M. Scheutjens, G. J. Fleer, Statistical theory of the adsorption of interacting chain molecules. 2. Train, loop, and tail size distribution, J. Phys. Chem. 84 (1980) 178-190

[33] G. P. van der Beek, M. A. Cohen Stuart, Polymer adsorption and desorption studies via ^{1}H NMR relexation of the solvents, Langmuir 7 (1991) 327-334

[34] B. Cattoz, T. Cosgrove, M. Crossman, S. W. Prescott, Surfactant-mediated desorption of polymer from the nanoparticle interface, Langmuir 28 (2012) 2485-2492

[35] J. C. Dijt, M. A. Cohen Stuart, G. J. Fleer, Reflactometry as a tool for adsorption studies, Adv. Colloid Interface Sci. 50 (1994) 79-101

[36] W. M. de Vos, B. Cattoz, M. P. Avery, T. Cosgrove, S. W. Prescott, Adsorption and surfactant-mediated desorption of poly(vinylpyrrolidone) on plasma- and piranha-cleaned silica surfaces, Langmuir 30 (2014) 8425-8431

[37] W. van de Ven, I. Pünt, A. Kemperman, M. Wessling, Unraveling ultrafiltration of polysaccharides with flow field flow fractionation, J. Membr. Sci. 338 (2009) 67-74

[38] C. O. Metin, L. W. Lake, C. R. Miranda, Q. P. Nguyen, Stability of aqueous silica nanoparticle dispersions, J. Nanopart. Res. 13 (2010) 839-850

[39] J. K. Armstrong, R. B. Wenby, H. J. Meiselman, T. C. Fisher, The hydrodynamic radii of macromolecules and their effect on red blood cell aggregation, Biophys J. 87 (2004) 4259-70

[40] S. Robinson, P. A. Williams, Inhibition of protein adsorption onto silica by polyvinylpyrrolidone, Langmuir 18 (2002) 8743-8748

[41] M. A. Cohen Stuart, Adsorbed polymers in colloidal systems: from statics to dynamics, Polym. J. 23 (1991) 669-682

[42] R. M. McDonogh, A. G. Fane, C. J. D. Fell, H.-C. Flemming, The influence of polydispersity on the hydraulic behaviour of colloidal fouling layers on membranes Perturbations on the behaviour of the "ideal" colloidal layer, Colloids Surf., A 138 (1998) 231–244

[43] J. A. Kitchener, Principles of action of polymeric flocculants, Brit. Polym. J. 4 (1972) 217-229

[44] A. S. Kim, E. M. V. Hoek, Cake structure in dead-end membrane filtration: Monte carlo simulations, Environ. Eng. Sci. 19 (2002) 373-386

CHAPTER 5

Fouling behavior of silica nanoparticle-surfactant mixtures during constant flux dead-end ultrafiltration

Abstract

The increasing use of engineered nanoparticles in costumer products results in their accumulation in water sources. Membrane technology has proven to be effective in the removal of colloidal particles, and therefore is an obvious candidate for the separation of nanoparticles from water as well. Nanoparticle stability and the presence of various surfactants in the nanoparticle suspension may have a great effect on the filtration performance. In addition both nanoparticle and surfactants both contribute to fouling of the membrane.

In this experimental study, we investigated the role of surfactant type (cationic, anionic and non-ionic) and concentration on fouling development, nanoparticle rejection and fouling irreversibility during dead-end ultrafiltration of model silica nanoparticles. Our work demonstrates that type of the surfactant influences the nanoparticle stability, which in turn is responsible for differences in fouling behavior of the nanoparticles. Moreover, the surfactant itself interacts with the PES-PVP membrane and contributes to the fouling as well. We have shown that anionic SDS (sodium dodecyl sulfate) does not interact extensively with the negatively charged silica nanoparticles and does not change significantly the surface charge and size of these nanoparticles. Adsorption of the cationic CTAB (cetyltrimethylammonium bromide) onto the silica nanoparticles causes charge transition and nanoparticle aggregation, whereas non-ionic TX-100 (Triton X-100) neutralizes the surface charge of the nanoparticles but does not change significantly the nanoparticle size. The most severe fouling development was observed for the silica nanoparticle – TX-100 system, where nanoparticles in the filtration cake formed exhibited the lowest repulsive interactions. Rejection of the nanoparticles was also highest for the mixture containing silica nanoparticles and TX-100.

5.1. Introduction

The rapid growth of nanotechnology has resulted in multiple applications of engineered nanoparticles (NPs) [1]. The increasing production of such inevitably leads to their accumulation in the aqueous environment after usage [2]. Over the last decades, membrane technology has been proven to be effective in the removal of colloidal particles such as proteins, natural organic matter (NOM) and inorganic particles [3-5] from water sources. Stability of the NPs plays a key role in their membrane filtration behavior using porous membranes [6-8]. Aggregation of nanoparticles in the bulk solution or at the membrane surface (due to concentration polarization) changes the size distribution of the solutes, and thus the rate of membrane pore blockage and porosity of the filtration cake formed [8-10]. Due to the high surface-area-to-volume ratio of nanoparticles, their stability is strongly related to their surface properties [11]. Often, to improve the stability of such dispersions various surface-active stabilizers (e.g. surfactants) are added [12-14]. The effectiveness of nanoparticle stabilization is determined by the type of the stabilizer, its affinity to the nanoparticles, and the concentration of both nanoparticles and stabilizers [11]. Adsorption of surfactants onto the nanoparticle surface may enhance electrostatic or steric repulsions between the nanoparticles, thereby reducing their tendency towards aggregation [15-17]. Furthermore, the presence of small non-adsorbing species (e.g. micelles) in the nanoparticle suspension leads to additional depletion stabilization [18]. On the other hand, adsorption of surfactants that only screens the surface charge of nanoparticles without providing an additional stabilization mechanism, facilitates nanoparticle aggregation [19]. Furthermore, since adsorption of surfactants to NPs and micelle formation are concentration dependent [20-22], the concentration of the surfactant in the feed solution will play an important role on the nanoparticle stability as well.

Apart from nanoparticle stability, the presence of surface-active compounds will also change the interactions between the nanoparticles and the membrane. As a result, adsorption of the NPs onto the membrane surface is promoted or reduced, depending on the affinity between the surfactant and the membrane [23, 24]. Despite the much smaller size of the surfactant molecules in comparison to the nanoparticles, they can form micelles that above the so-called critical micellar concentration (CMC) can be much larger than the NPs. Furthermore, surfactants may adsorb on the membrane or associate on the membrane surface as micelles or bi-layers above the so-called critical association concentration (CAC). All these effects will inevitably lead to more severe fouling when filtering suspensions containing nanoparticles and surfactants.

Literature on nanoparticle filtration in the presence of surfactants is limited. Work that systematically compares the role of different surfactant types on the filtration of nanoparticles is lacking. Therefore, the aim of this study is to reveal the role of the type of surfactant on nanoparticle filtration. Three types of industrially prominent surfactants are used: anionic sodium dodecyl sulphate (SDS), cationic cetyltrimethylammonium bromide (CTAB), and non-ionic Triton X-100 (polyethylene glycol tert-octylphenyl ether). A detailed investigation of feed solution properties, combined with data from filtration experiments, allows determination of relevant mechanisms responsible for membrane fouling by nanoparticles in the presence of surfactants.

5.2. Experimental

5.2.1. Materials

Colloidal silica nanoparticles (Ludox TM-50) were used as model nanoparticles that were purchased as a 50% w/w suspension in water (Sigma Aldrich). Aqueous solutions of ACS grade NH_4HCO_3-$(NH_4)_2CO_3$, HCl and NaOH (Sigma Aldrich) were used to adjust the pH and ionic strength of the solutions, respectively. Sodium dodecyl sulfate (SDS), cetyltrimethylammonium bromide (CTAB) and Triton X-100 (TX-100) were purchased from Sigma-Aldrich. All solutions were prepared using ultrapure water (Milli-Q, resistivity>18.2 MΩ·cm); all chemicals were used without further purification.

5.2.2. Membrane and membrane characterization

Commercially available inside-out polyethersulfone-polyvinylpyrrolidone (PES-PVP) ultrafiltration (UF) membranes supplied by Pentair X-Flow BV (UFCLE type, MWCO 150 kDa) were used. UF filtration modules with a filtration area of 100 cm^2 were prepared by potting 10 hollow fiber membranes (inner diameter 0.8 mm, 40 cm long) in a PE tube (outer diameter 8 mm) with two-component polyurethane glue.

The membranes were characterized in terms of pure water permeability, inner surface charge and pore size distribution. The surface potential of the inner membrane was determined via streaming potential measurements using a SurPASS electrokinetic analyzer (Anton Paar GmbH). In the experiments, we used 1 mM KCl as a background electrolyte solution; the pH was adjusted using aqueous 0.1 M NaOH and 0.1 M HCl solutions. The zeta potential was calculated according to the Fairbrother-Mastin equation [25]. The pore size distribution of the membranes was measured by permporometry. This technique is based on the controlled stepwise blocking of pores by condensation of a

vapor, linked with the simultaneous measurement of the oxygen flux through the membrane [26]. Cyclohexane was used as the condensable vapor in our home made setup.

5.2.3. Characterization of nanoparticle – surfactant mixtures

The CMC values of cationic and anionic surfactants were determined using conductivity measurements of the solutions at 30° C in the presence of 1 mM ammonium bicarbonate buffer. The CMC values were found as the intersection of the two slopes describing conductivity rise with surfactant concentration before and after micelle formation [27]. Conductivity was measured using a conductometer Cond 3210 (WTW GmbH, Germany). The CMC of the non-ionic TX-100 was determined using a force tensiometer K20 (Krüss GmbH, Germany) equipped with a Du Noüy ring. The CMC value was obtained by plotting the logarithm of the obtained surface tension versus the surfactant concentration. The CMC was estimated from the intersection of the linear regression line describing the decrease of the surface tension with the surfactant concentration below the CMC and the line describing a constant surface tension with increasing surfactant concentration above the CMC.

The hydrodynamic diameter of the nanoparticles in the mixture with surfactants was measured in batch mode using a DAWN-Heleos-8 modified at an angle of 108°, to which a dynamic light scattering (DLS) apparatus (NanoStar, Wyatt Technology Corporation, USA) was connected via a glass fiber cord. DLS measurements were carried out at a wavelength of 658 nm at 30 ± 1°C. DLS data collection and analysis was performed using Astra® 6.1 software (Wyatt Technology Corporation, USA).
Electrophoretic mobility measurements of the silica nanoparticles were carried out via electrophoresis measurements using a Malvern ZetaSizer 3000Hsa (Malvern Instruments, United Kingdom) to obtain the zeta potential of the nanoparticles and their mixtures with surfactants. Both light scattering and zeta potential measurements were conducted using a 50 mg/L nanoparticle solution prepared in various concentrations of investigated surfactants in 1 mM ammonium bicarbonate buffer solution. All experiments were repeated at least three times.

5.2.4. Filtration experiments

All feed solutions were prepared from a 1 mM ammonium bicarbonate buffer solution (Milli-Q water, pH 8) containing 50 mg/L of silica nanoparticles. The

concentration of surfactants in the feed solutions was varied from 0.125 mM to 8 mM. The surfactant concentrations were chosen such to cover CMCs of all three surfactants in order to investigate the filtration behavior of silica nanoparticles below and above the CMC. The temperature of the feed solution was maintained at 30°C by immersing the feed vessel in a temperature-controlled stirred water bath. Filtration experiments were started 24 h after the feed solution was prepared in dead-end filtration mode using an 'OSMO Inspector' filtration setup developed and automated by Convergence Industry B.V. (Enschede, The Netherlands). The schematic diagram of the filtration setup is given in Fig. 1.

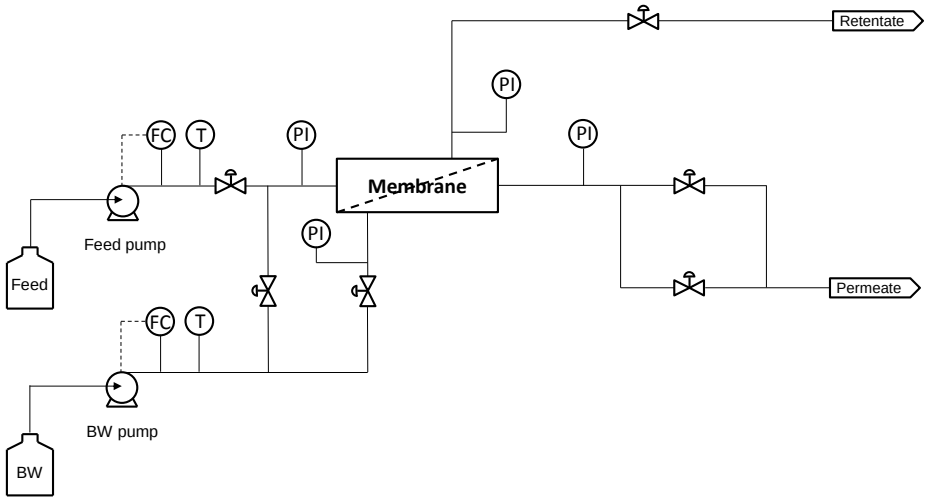

Fig. 1. Schematic diagram of the OSMO Inspector filtration setup. Feed and BW are feed and backwash water reservoirs, respectively. Two mass flow controllers (FC) control the feed and backwash flows. The pressure of the feed, the backwash, the permeate and the retentate is measured using pressure indicator (PI). The temperature (T) in the feed and downstream of the backwash pump is monitored as well.

The system contains a feed and a backwash pump (Liquiport® NF100, KNF, USA). By means of solenoid switching valves (Plast-o-matic Valves, Inc. USA), the water from the backwash tank can be fed either to the feed or the permeate side of the membrane, enabling the integration of automatic pure water flux experiments. Two high precision mass flow controllers (Cori-Flow™ model M15, Bronkhorst Cori-Tech, The Netherlands) are installed to measure and control the feed and backwash fluxes. Prior to filtration, the membranes were immersed in a 20% w/w ethanol solution for at least 24 h to remove conservation chemicals and to wet all the pores. After this, ultrapure water

was filtered across the membrane modules at 2 bar for 10 minutes. The OSMO software was programmed to perform single filtration-backwash experiments at a flux of 100 L/m·h. The schematic description of the filtration-backwash experiment is shown in Fig. 2.

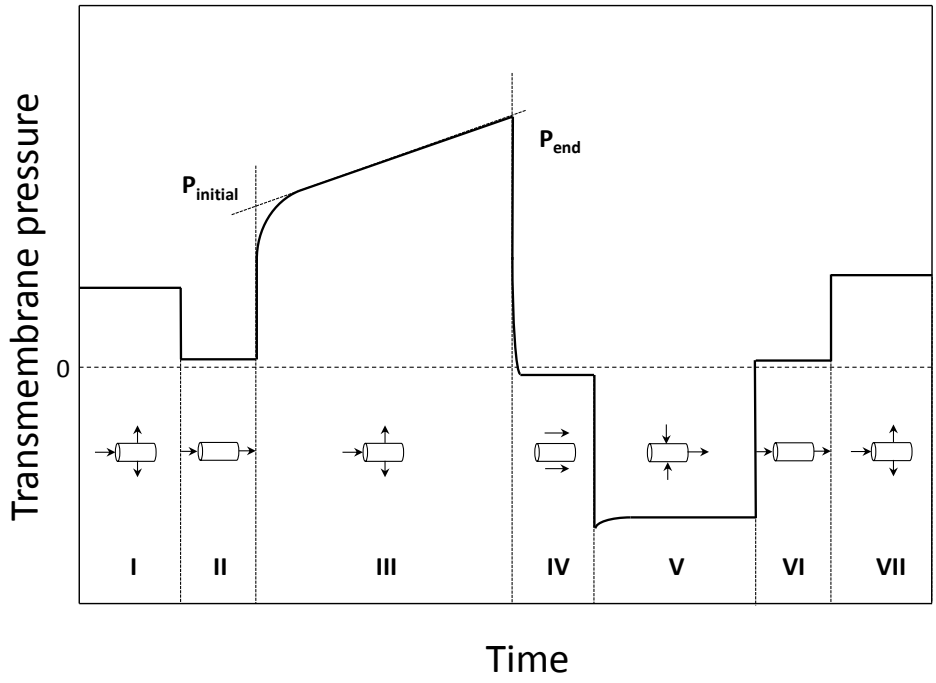

Fig. 2. Single filtration-backwash cycle (adapted from van de Ven et al. [28]). I – pure water permeation, II – forward flush with feed solution, III – filtration, IV – flush of the shell side, V – backwash, VI – forward flush with water, VII – pure water permeation.

Firstly, at the beginning of each filtration experiment the pure water permeability for each module was measured for 10 minutes at a flux of 100 L/m·h (I). As a result of the applied potting procedure, the obtained permeabilities for the individual modules varied slightly due to small variations in the membrane surface area. Secondly, a feed solution containing silica nanoparticles and surfactants was introduced into the lumen of the fibers by a forward flush (II) that was carried out for 1 minute. In the third step, the solenoid valve was switched to close the retentate outlet of the module and dead-end filtration (III) was started. The filtration was carried out under a flux of 100 L/m·h for one hour. After filtration, the shell side of the module was flushed with water (IV) for 1 minute in order to remove the retentate present and to prepare the module for backwash

(V), which was carried out for 30 minutes at 250 L/m·h. Relatively long backwash times were applied to remove surfactant residues adsorbed to the membrane surface. After the backwash step, the lumen of the fibers was flushed (VI) with water for 1 minute. In the last step, the permeability of the membrane (VII) was measured once again in order to calculate flux recovery. Each filtration experiment was repeated at least three times.

5.2.5. Data processing

Deposition of the nanoparticles on the membrane surface or inside the porous structure of the membrane leads to an increase of the filtration resistance, which can be calculated from Eq. 1:

$$R = \frac{\Delta P}{\eta \cdot J} \tag{1}$$

where R (1/m) is the total filtration resistance, ΔP (Pa) is the transmembrane pressure, η (Pa·s) is the viscosity and J ($m^3/m^2 \cdot s$) is the flux.

The rejection of the solute by the membrane is defined by Eq. 2:

$$\sigma = 1 - \frac{C_p}{C_f} \tag{2}$$

where σ is the rejection (-), C_P is the concentration of the solute in the permeate sample (mg/L), and C_f is the concentration of the solute in the feed solution (mg/L). For a single filtration experiment 6 permeate samples were collected during the filtration. In order to evaluate the nanoparticle rejection, concentrations of nanoparticles in the feed and permeate samples were determined using Inductively Coupled Plasma Mass Spectrometry (ICP-MS; Thermo Fisher Xseries 2). Since rejections obtained were more or less constant during a single filtration experiment, we report average rejection values, which are obtained from averaging rejections calculated from 6 collected permeate samples in 3 repeated filtration runs (in total 18 permeate samples per rejection point).

The total fouling rate describes the fouling development as defined in the improved flux-step method developed by van der Marel et al. [29]. The fouling rate was calculated according to Eq. 3.

$$F_{tot} = \frac{dR}{dt} = \frac{P_2 - P_1}{\eta \cdot J \cdot \Delta t} \tag{3}$$

where R (1/m) is the total filtration resistance, P_1 (Pa) is the initial transmembrane pressure, P_2 (Pa) is the final transmembrane pressure, η (Pa·s) is the viscosity, J ($m^3/m^2 \cdot s$) is the flux and Δt (s) is the filtration time.

The permeability recovery PR is used to describe irreversibility of the fouling and is defined as:

$$PR = \frac{R_m}{R_{mbw}} \tag{4}$$

where PR (-) is the permeability recovery, R_m (1/m) is the filtration resistance of the membrane before filtration (step I in Fig. 2) and R_{mbw} (1/m) is the hydraulic resistance of the membrane after the backwash step (step VII in Fig. 2).

5.3. Results and discussion

5.3.1. Membrane characteristics

The properties of the UF membrane used are listed in Table 1. The Molecular Weight Cut-Off (MWCO) reported by the manufacturer was 150 kDa. The experimentally determined pure water permeability measured was 1000 ± 100 $L/m^2 \cdot h \cdot bar$. According to the permporometry measurements, the mean pore diameter of this membrane was found to be 24 ± 5 nm. Streaming potential measurements showed that the inner surface of the membrane had a zeta potential of -24 ± 3 mV at pH 8.

Table 1. Properties of the applied membrane.

Membrane					
Type	Material	MWCO* [kDa]	Clean water permeability [$L/m^2 \cdot h \cdot bar$]	Pore Diameter [nm]	Zeta Potential at pH 8 [mV]
Pentair X-Flow UFCLE	PES/PVP	150	1000 ± 100	24 ± 5	-24.9 ± 3.4

*manufacturer's data

5.3.2. Feed solution characteristics

The properties of the surfactants applied are listed in Table 2. The experimentally determined CMC the values are comparable to values reported in literature [27]. Above the CMC, surfactants form micelles of which the size varies for each surfactant type, as shown in Table 2. The Krafft temperature is the minimum temperature at which

surfactants can form micelles. Since for CTAB this temperature is quite high (25°C), we carried out all our experiments at 30°C to ensure that all surfactants can form micelles.

Table 2. Properties of the applied surfactants at 30°C.

Surfactant	Type	M_w [g/mol]	CMC [mM]	Micelle diameter [nm]	Krafft temp. [°C]
SDS	anionic	288	7.49	3.7 [30]	18 [31]
CTAB	cationic	364	0.99	7 [32]	25 [33]
TX-100	non-anionic	647	0.25	7.4 [34]	<0 [35]

Since surfactants are surface active molecules, they can adsorb onto nanoparticles and change their surface properties, such as charge. Correspondingly, this can lead to increased or reduced the stability of the nanoparticles in the suspension, depending on whether the surfactants enhance or reduce repulsive interactions between the nanoparticles. The surface zeta potential and the hydrodynamic diameter of the silica nanoparticles as a function of the surfactant concentration at pH 8 are shown in Figs. 3a and Fig 3b, respectively. To take into account the behavior of the pure surfactants, zeta potential measurements were also conducted with pure surfactant suspensions at a concentration of 16 mM, which are represented as star symbols in Fig. 3a.

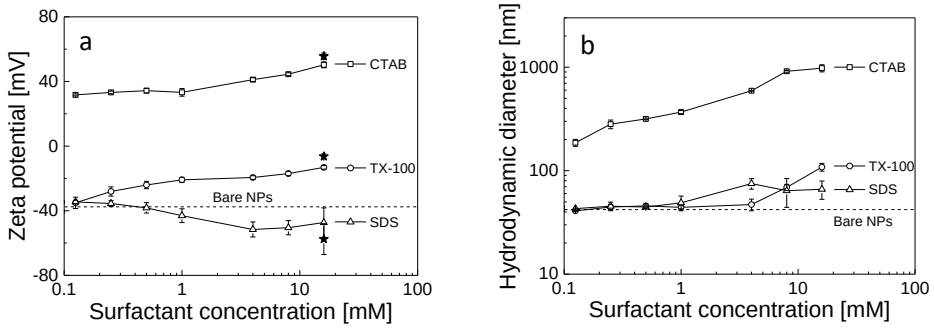

Fig. 3. Zeta potential (a) and hydrodynamic diameter (b) of silica nanoparticles as a function of the (CTAB, TX-100 or SDS) surfactant concentration at pH 8 at 30°C. The stars represents pure surfactant suspension at 16 mM.

As Fig. 3a shows, the zeta potential of the silica nanoparticles becomes slightly more negative in the presence of the negatively charged SDS compared to bare silica without any added SDS. These results are rather surprising as both silica and SDS are

negatively charged, and hence we would not expect any adsorption of SDS onto silica [36]. Nonetheless, our observations indicate that SDS could be adsorbed in small amounts onto the silica surface. Ahualli et al [15] reported a similar effect in electrophoretic mobility measurements of silica nanoparticles in SDS solutions ranging from 0.01 mM to 8 mM SDS. They observed an increase in the negative mobility and zeta potential and attributed the observation to a super charging effect that increased the effective charge of the silica nanoparticles (possible because only part of the interaction between silica and SDS is electrostatic) [15]. Another possible explanation for this observation could be the adsorption of small amounts of SDS onto the heterogeneities on the colloidal silica surface [17].

Fig. 3b shows a slight increase of the hydrodynamic diameter of the nanoparticles with the SDS concentration. These findings suggest either a limited aggregation of the nanoparticles or the presence of some large impurities in SDS (the applied SDS was 90% pure). Nevertheless, we can conclude that addition of SDS to the nanoparticle suspension has only a little effect on both nanoparticle charge and size.

In the case of CTAB-silica systems, addition of positively charged CTAB modifies the silica surface from negative to positive, implying strong adsorption of CTAB onto the nanoparticle surface. This process has been extensively studied using various techniques [37-39]. CTAB can adsorb onto the silica surface due to (i) surface charge neutralization, (ii) hydrophobic interaction by the long hydrocarbon tail, or (iii) a combined effect of these two mechanisms [39, 40]. In this study, however, we also observe that with the addition of CTAB to the silica nanoparticle suspension, the hydrodynamic diameter increases significantly, indicating the formation of larger aggregates (Fig. 3b). As such, we can conclude that aggregation occurs due to the adsorption of CTAB on the silica surface. During the adsorption of CTAB molecules onto silica surface, a negative charge of the nanoparticles is neutralized and thus repulsive interactions between nanoparticles vanish allowing aggregation. Further addition of CTAB causes nanoparticle charge transition to positive. The kinetic of this transition from positive to negative charge of the silica nanoparticles is mainly responsible for nanoparticle aggregation and size of the aggregates.

As shown in Fig. 3a, with increasing TX-100 concentration, the zeta potential becomes less negative. For pure TX-100 (being a non-ionic surfactant), the measured zeta potential at 16 mM was -6.4 ± 1.6 mV, which is much less negative than the value obtained for bare silica nanoparticles. This is an indication of surfactant adsorption and shielding of the nanoparticle charge by TX-100. The work of Levitz et al. [41],

Giordano-Palmino et al. [22] and Alexeev et al. [16], showed that TX-100 can adsorb effectively onto the colloidal silica surface as individual molecules at low concentrations via hydrogen bonding, followed by the formation of micelles on the nanoparticle surface through association at higher concentrations. Furthermore, similarly to the SDS case, at 8 mM of TX-100 a slight increment in the hydrodynamic diameter is observed, probably due to nanoparticle aggregation induced by reduced repulsive interactions between the nanoparticles upon adsorption of the surfactant.

These results show that the type of the surfactant has a significant effect on the nanoparticle charge and size in the suspension. SDS interacts only slightly with the silica nanoparticles and no significant charge or size change is observed. CTAB reverses the nanoparticles charge and causes their aggregation. In the case of the non-ionic surfactant TX-100, the nanoparticle charge is reduced but nanoparticle aggregation is not significant. These insights are essential to explain filtration behavior of nanoparticles/surfactant mixtures.

5.3.3 Filtration experiments

5.3.3.1. Filtration of pure surfactant and bare nanoparticles

The resistance development during constant flux filtration of the feed solutions containing bare silica nanoparticles (50 mg/L) or pure surfactants (8 mM) is shown in Fig. 4a.

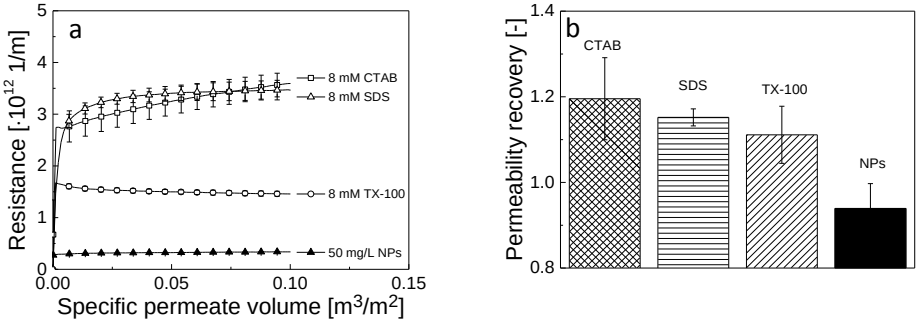

Fig. 4. Resistance (a) and permeability recovery (b) during filtration of pure surfactants and bare silica nanoparticles.

In comparison to the surfactants (of which the concentration was 2.31 g/L, 2.92 g/L, and 5.18 g/L for SDS, CTAB and TX-100, respectively), the applied concentration of nanoparticles was considerably lower (50 mg/L). Therefore, the lowest filtration

resistance was obtained for the filtration of bare silica nanoparticles. Due to their high stability, the nanoparticle deposit is porous and permeable, and thus the resistance increases only gradually with the permeate volume, as shown in Fig 4a. The thickness of the filtration cake at the end of the filtration was estimated to be about 3.1 μm taking into account the mass of deposited nanoparticles, assuming a hexagonal packing in the filtration cake and a uniform distribution along the module length.

As shown in Fig. 4a, pure surfactants at a concentration of 8mM contribute significantly to the membrane fouling. The highest resistance was generated during the filtration of the ionic surfactants – SDS and CTAB. A significantly lower resistance was observed for the non-ionic TX-100. For all three surfactants, hydrophobic interactions between the hydrophobic tail of the surfactant and the hydrophobic PES polymer molecules in the membrane are expected to be responsible for surfactant adsorption onto the membrane surface [42], as schematically shown in Fig. 5. Furthermore, for anionic SDS, Prasad et al. [23] reported the presence of attractive interactions between the negatively charged SDS and the polarizable pyrrolidone group of PVP in the membrane, which would result in the formation of micelle-like aggregates on the membrane surface by association (Fig. 5a). For cationic CTAB, electrostatic attractions between the positively charged head group of the CTAB molecule and the negatively charged membrane can be considered as an additional adsorption mechanism [47] (Fig. 5b). All these adsorption mechanisms contribute to surfactant deposition onto the membrane surface and inside the pores, enhancing the hydraulic resistance. For all three surfactants, subsequent stabilization of the resistance (Fig. 4a) can be related to saturation of the membrane with the surfactant. The maximum surfactant adsorption capacity of the membrane is reached and transport of surfactant through the membrane pores becomes undisturbed again. As a result, we do not observe any measurable surfactant rejection. This is expected, when we take into account the size difference between the membrane pores (Table 1) and the size of single surfactant molecules or even the micelles formed by the surfactants (Table 2).

As Fig. 4b shows, for all three pure surfactants the permeability recovery is higher than 1 (PR>1). These results clearly indicate that the surfactants contribute to the enhancement of the pure water permeability regardless of their adsorption during the filtration. We attribute this effect to improved wetting of the fibers by the surfactant [43, 44]. This clearly shows that the surfactants do not only influence the properties of the nanoparticles but also the membrane characteristics. In contrast to the results obtained for surfactants, the permeability recovery during the filtration of bare silica nanoparticles is lower than 1 (PR<1, see Fig. 4b) indicating irreversible fouling.

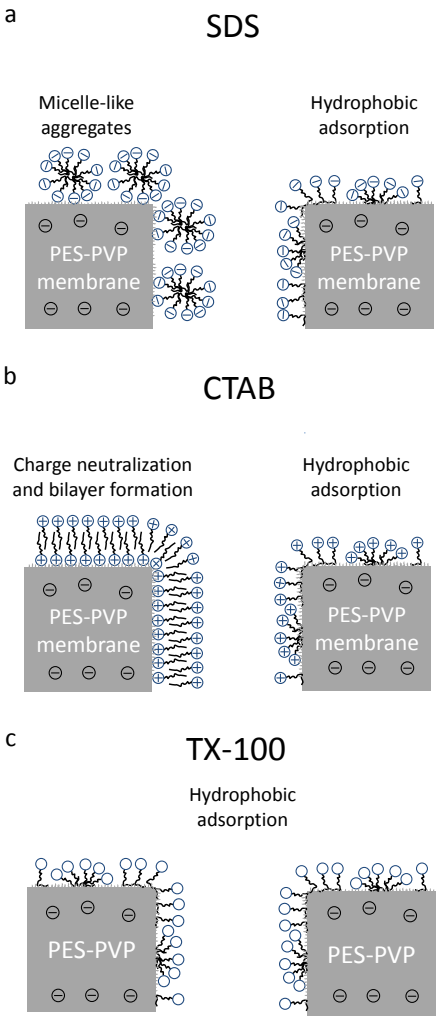

Fig. 5 Schematic representation of the possible interactions between a PES-PVP membrane and a) SDS (negative), b) CTAB (positive) and c) TX-100 (neutral) surfactants.

5.3.3.2. Fouling development of nanoparticles in the presence of anionic SDS

We also investigated the combined role of the surfactant type and the concentration on fouling development during dead-end filtration of silica nanoparticles. Fig. 6 summarizes the filtration results obtained during filtration of silica nanoparticles with various concentrations of the anionic surfactant SDS.

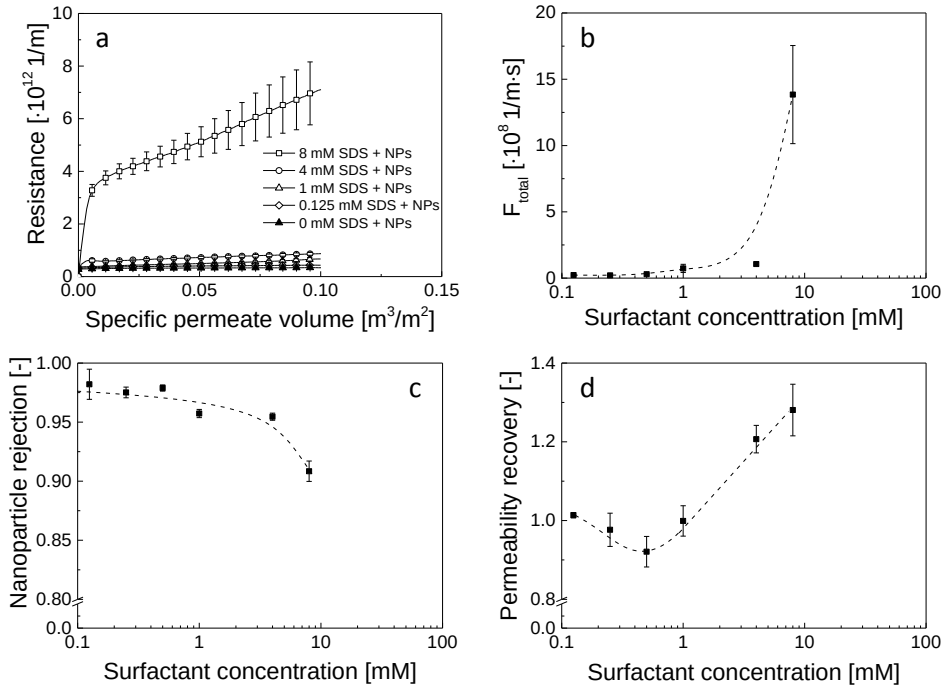

Fig. 6 (a) Resistance development as function of specific permeate volume, (b) fouling rate, (c) rejection of nanoparticles and (d) permeability recovery as a function of surfactant concentration during constant flux dead-end filtration of 50 mg/L silica nanoparticles with anionic SDS at 30 °C. Dashed lines are drawn to guide the eye.

Fig. 6a shows that for all SDS concentrations investigated (0.125 mM - 8 mM), an increase of the surfactant concentration in the feed solution results in a higher hydraulic resistance, although this effect is less pronounced for lower concentrations. These findings are opposite to previous studies, which reported that addition of surfactant at low concentrations can result in reduced fouling. Singh and Song [18] investigated the influence of the SDS concentration on fouling development during cross-flow filtration. They postulated that addition of SDS in concentrations below 0.3 mM allows formation of a more loosely packed cake on the surface of UF membrane. Thus, a lower fouling rare was obtained. However, in our case even for the lowest SDS concentration (0.125 mM) this effect was not observed. We relate this difference in fouling behavior of silica nanoparticles to the filtration mode at which the experiments were carried out (cross-flow in the case of Singh and Song and dead-end in this work) and limited interactions between nanoparticles and surfactants. The formation of a more porous cake layer in the

presence of SDS, as proposed by Singh and Song, could only occur if the electrostatic repulsions between the nanoparticles are enhanced. However, this is not the case for our feed solution since the zeta potential measured reduces only slightly with increasing SDS concentration. Therefore, the synergic contribution of the SDS molecules to fouling development dominates the effect of the increased surface charge of the nanoparticles. As a result, the filtration resistance slightly increases with SDS concentration, despite the slightly higher repulsive interactions between the nanoparticles (Fig. 3a). Interestingly, below 8 mM SDS the filtration resistance is on a significantly lower level (the maximum obtained resistance at 4 mM was $8.7 \cdot 10^{11}$ 1/m) than the resistance obtained at 8 mM of SDS (maximum obtained resistance $7.1 \cdot 10^{12}$ 1/m). This difference in the fouling development is clearly illustrated in Fig. 6b, where the fouling rate is plotted as a function of the surfactant concentration. The obtained fouling rate rises only marginally with SDS concentrations below 8 mM, but it significantly increases at 8 mM. Such behavior can originate from the fact that at 8 mM, SDS forms micelles (CMC of SDS for our system was in approx. 7.5 mM, see Table 2). This is in contrast to lower concentrations. At 8 mM, these micelles can also contribute to the filtration resistance. Consequently, due to the small effect of SDS on nanoparticle stability, there is only a limited contribution of SDS to fouling development below the CMC of SDS. However, above the CMC formed micelles contribute strongly to the filtration resistance.

The rejection of silica nanoparticles during their filtration in the presence of SDS as a function of the surfactant concentration is given in Fig. 6c. The rejection of bare silica nanoparticles during the complete filtration course was approx. 98 ± 1%. Such a high rejection was expected since the average pore size (see Table 1) is approximately the average size of the silica nanoparticle, as reported elsewhere [45]. Retention of nanoparticles is not only caused by size exclusion of the nanoparticles, but also by adsorption of the nanoparticles onto the membrane surface [46]. These two effects result in a more effective pore blockage and thus a more effective nanoparticle retention by the formation of a cake layer on the membrane surface, acting as an additional barrier for silica nanoparticles.

Addition of the SDS to the feed solution contributes to a noticeable reduction of the nanoparticle rejection, as shown Fig. 6c. Lower SDS concentrations (0.125-0.5 mM) do not change the nanoparticle rejection significantly. However, further increase of the SDS concentration gradually reduces the nanoparticle rejection to approx. 91% at 8 mM of SDS. This decrease in rejection can be related to the reduced interactions between the nanoparticles and the membrane after adsorption of SDS to the membrane and to the

nanoparticles. Nanoparticle adsorption onto the membrane is reduced since the adsorption sites are already occupied by SDS. Consequently, the nanoparticles will block the pores less effectively. Moreover, slightly enhanced repulsive interactions between the nanoparticles in the filtration cake formed and a less ordered structure of the filtration cake in the presence of SDS micelles both cause the cake layer to be more open [47]. This results in an easier diffusion of the nanoparticles through the filtration cake and consequently in a lower rejection.

As described in section 5.2.4, a pure water permeability check was carried out before filtration with the nanoparticle suspension and after the backwash procedure. The purpose of this was to ascertain the effect of the surfactant concentration and type on the extent of irreversible fouling. If nanoparticles irreversibly deposit on the membrane surface and irreversible fouling occurs, we expect a PR of <1. As shown in Fig. 4b, filtration of the pure surfactants leads to PR>1. We relate this to better wetting of the membrane in the presence of surfactants, which makes surface of the membrane more hydrophilic. Fig. 6d shows the permeability recovery as a function of the SDS concentration. At lower SDS concentrations (0.125 mM - 1 mM) the permeability recovery is approx. 1. However, it increases to values of 1.21 ± 0.07 and 1.28 ± 0.07 for 4 mM and 8 mM, respectively. We speculate that at lower surfactant concentrations (0.125 mM – 1 mM) irreversible fouling caused by the mixture of silica nanoparticles and SDS does not occur, which might be due to the moderate transmembrane pressure applied and only limited adsorption of the surfactant. At higher SDS concentrations (4 mM - 8 mM), adsorption of SDS onto the membrane is facilitated and the wetting of the membrane surface is more effective. Permeability recovery is likely to be greater due to this pronounced wetting, even when nanoparticle deposition is enhanced due to the higher transmembrane pressures that need to be applied to maintain a constant permeate flux.

5.3.3.3. Fouling development of nanoparticles in the presence of cationic CTAB.

Results obtained during the filtration of silica nanoparticles in a mixture with CTAB are summarized in Fig. 7. The observed change of the nanoparticle charge from negative to positive (see Fig. 3a) and subsequent aggregation of the nanoparticles (see Fig. 3b) does not result in a noticeably different nanoparticle filtration behavior compared to that observed for SDS. As also obtained for anionic SDS (section 5.3.3.2), an increase of the cationic CTAB concentration results in more severe fouling

development (see Fig 7a). Large aggregates of nanoparticles, existing already in the bulk of the feed solution upon CTAB addition (see Fig. 3b), result in the formation of a non-uniform filtration cake, full of defects. Furthermore, an increase of the nanoparticle size results in a more open filtration cake and thus reduced contribution of the nanoparticle deposit to the filtration resistance. Based on these observations, we suggest that the development of the resistance is dominated by the CTAB concentration in the feed solution and aggregated nanoparticles do not contribute significantly to fouling development. This hypothesis is supported by the fact that the fouling rate rises linear with the logarithm of CTAB concentration (Fig. 7b), and thus no synergic effect between nanoparticles and CTAB on fouling is observed.

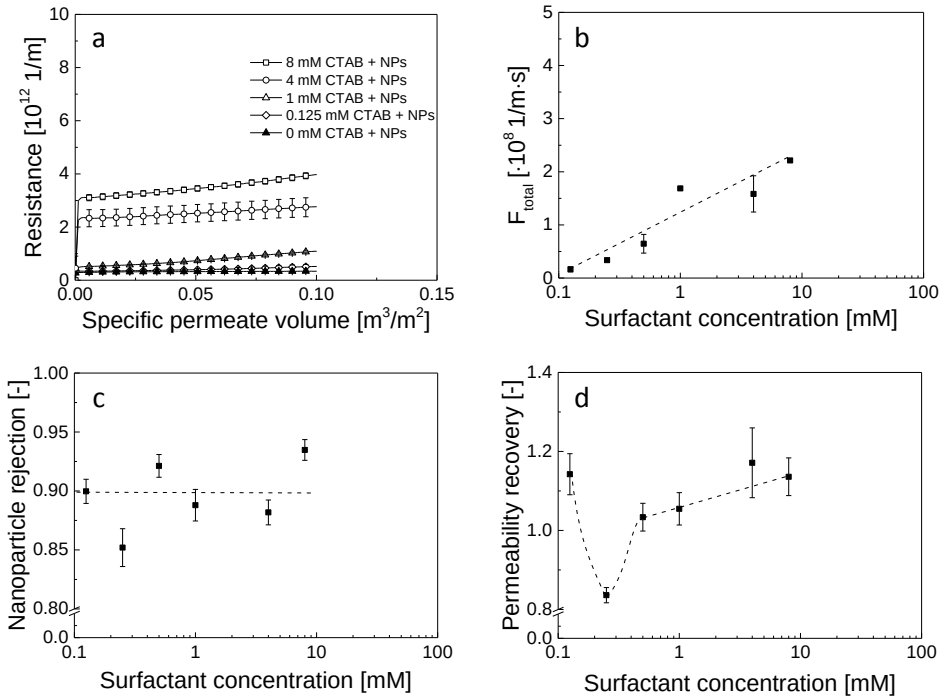

Fig. 7 (a) Resistance development as function of specific permeate volume, (b) fouling rate, (c) rejection of nanoparticles and (d) permeability recovery as a function of surfactant concentration during constant flux dead-end filtration at 30 °C of 50 mg/L silica nanoparticles with cationic CTAB. Dashed lines are drawn to guide the eye.

In the case of CTAB, nanoparticle rejection varies from approx. 85% for 0.25 mM CTAB to 95% for 8 mM CTAB (see Fig. 7c). The data obtained for CTAB are more scattered than for SDS, with large error bars, and it is more difficult to observe a clear correlation between surfactant concentration and rejection. We can associate this lower nanoparticle rejection and its irreproducibility to the aggregation of nanoparticles in the feed solution (see Fig. 3b) and the previously mentioned non-uniform nanoparticle deposition on the membrane surface. Since aggregation is a kinetic process, it can lead to a non-uniform size distribution of the nanoparticles in the feed solution during separate filtration runs. As a result, the uniformity of the filtration cake will vary for each of the separate filtration runs. This effect is more pronounced for CTAB than for the two other surfactants. Poor control over the aggregate size can be also responsible for the poor correlation between surfactant concentration and nanoparticle rejection. Surprisingly, the nanoparticle rejection is the lowest when CTAB is present in the feed solution (compared to the other surfactants). Although intuitively one would think that the formation of nanoparticle aggregates would result in higher rejections, the aggregation of nanoparticles in the feed solution can resulting in a non-uniform thickness of the filtration cake and formation of isolated areas on the membrane surface that are less effectively covered by the nanoparticle deposit. Transport of some non-aggregated nanoparticles through the membrane is facilitated in such regions resulting in slightly lower nanoparticle rejections. However, to validate this assumption additional detailed investigations on the transport phenomena of CTAB-coated silica nanoparticles in porous media need to be carried out, which is beyond the scope of this work.

The permeability recovery obtained after filtration of silica nanoparticles in a mixture with CTAB is plotted in Fig. 7d. The results obtained for cationic CTAB are similar to those obtained for anionic SDS. At the lowest investigated surfactant concentration (0.125 mM), permeability recovery was about 1.14 ± 0.05 (PR>1) indicating reduced nanoparticle deposition and wetting of the membrane. By increasing the concentration of CTAB to 0.25 mM, the transmembrane pressure during the filtration rises and more irreversible fouling is observed since permeability recovery decreases to about 0.84 ± 0.02 (PR<1). However, a further increase of the CTAB concentration causes improved wetting of the fibers and permeability the recovery raises again (PR>1).

5.3.3.4. Fouling development of nanoparticles in the presence of non-ionic TX-100.

From all three investigated surfactants, the presence of the non-ionic TX-100 in the feed solution causes the most severe fouling development, as shown in Fig 8a. Like for the other two ionic surfactants, an increase of the TX-100 surfactant concentration also caused greater filtration resistance. Furthermore, from a concentration of 1 mM, 4 mM and 8 mM of TX-100, the resistance increase exponentially with specific permeate volume as opposite to the linear increase observed for the two other surfactants. This severe fouling is not only a result of the higher surfactant load but it is clearly related to the less negative zeta potential of the nanoparticles in a mixture with TX-100 (Fig. 3a). Repulsive interactions between nanoparticles are weakened, and therefore a more compact and dense cake structure can be formed. As a result, the transmembrane pressure and filtration resistance increase considerably faster with specific permeate volume compared to those of SDS and CTAB, and in the extreme case, it grows exponentially. The significant contribution of TX-100 to fouling development is clearly illustrated in Fig. 8b, where the fouling rate is plotted as a function of the surfactant concentration. As shown in Fig. 8b, the fouling rate obtained during filtration of the silica nanoparticles with non-ionic TX-100 was one order of magnitude higher than those obtained for SDS (below 8 mM SDS, Fig. 6b) and CTAB (Fig. 7b), due to the more compact and dense cake formed (different scales on the y-axis in Figs. 6b, 7b and 8b).

Addition of non-ionic TX-100 to silica nanoparticles does not change significantly the rejection in comparison to the bare nanoparticles. For all concentrations of TX-100 investigated, the rejection is 98-99%, as shown in Fig. 8c. The more compact structure of the filtration cake and the more severe fouling (Fig. 8a) compared to the other two surfactants, results in the highest nanoparticle rejection observed for the three cases described. Limited diffusion of nanoparticles across such a dense nanoparticle deposit contributes to a high nanoparticle rejection, which is rather independent of the surfactant concentration.

Figure 8d shows that for non-ionic TX-100, the permeability recovery is the highest for the lowest surfactant concentration (0.125 mM). At intermediate surfactant concentrations, it is more or less constant (around 1) after which it reduces significantly at the highest surfactant concentration (8 mM) to 0.81 ± 0.01. The significantly higher transmembrane pressures used during filtration with 8 mM of TX-100 than those for all the other filtration runs and the lower repulsive interactions between the nanoparticles in the presence of TX-100 can explain the reduced permeability recovery. We think that

wetting of the membrane at increased TX-100 surfactant concentration is dominated by extensive irreversible fouling, as opposed to the behavior of the anionic and cationic surfactants (Figs. 6d and 7d).

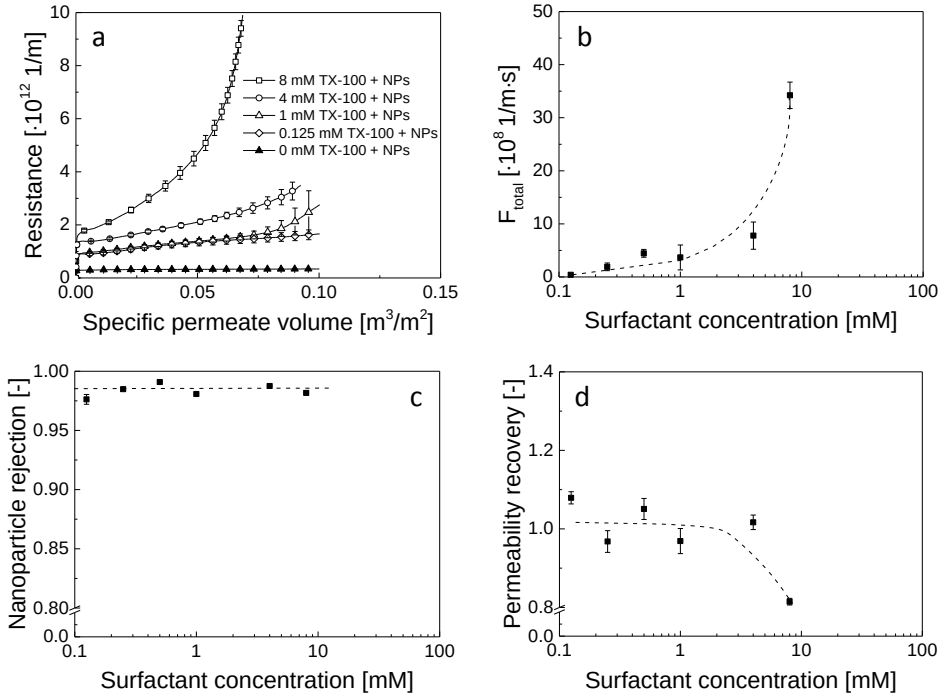

Fig. 8 (a) Resistance development as function of specific permeate volume, (b) fouling rate, (c) rejection of nanoparticles and (d) permeability recovery as a function of surfactant concentration during constant flux dead-end filtration of 50 mg/L silica nanoparticles at 30 °C with non-ionic TX-100. The dashed lines are drawn only to guide the eye.

5.4. Conclusions

In this experimental study, we investigated the effect of three different types of commercial surfactants (CTAB, SDS and TX-100) on the fouling development during hollow fiber dead-end ultrafiltration of silica nanoparticles and tried to give insight in the mechanisms of nanoparticle rejection and fouling development.

The stability of the nanoparticle suspension is found to be dependent on the type of surfactant. The most prominent aggregation of nanoparticles in the feed solution is observed after addition of CTAB, where the surface charge of the nanoparticles is inverted from negative to positive. Non-ionic TX-100 neutralizes the surface charge of

the silica nanoparticles causing a slight increase of the nanoparticle size. Anionic SDS does not interact extensively with the negatively charged silica nanoparticles.

Addition of anionic SDS to the feed solution has very limited synergic effect on fouling development below the CMC value of SDS, whereas above the CMC, fouling develops much more strong. For cationic CTAB, aggregation of the nanoparticles results in only a limited contribution of the nanoparticles to the built up of the filtration resistance and fouling development is dominated by the surfactant concentration. Addition of non-ionic TX-100 to the nanoparticle suspension indisputably reduces the repulsive interactions between the nanoparticles thus severely enhancing fouling. Furthermore, we observe that for each surfactant fouling is more pronounced at higher surfactant concentration.

Also the nanoparticle rejection is influenced by the type of surfactant and the concentration. In general, nanoparticle rejection increased in the order of CTAB-silica < SDS-silica < TX-100-silica. We speculate that the difference in nanoparticle rejection has its origin in the homogeneity and density of the cake layer formed. Fouling irreversibility is difficult to assess due to additional wetting phenomena of the fibers in the presence of the surfactants. In some cases, this results in permeability recoveries above 1.

In general, we can conclude that surfactants play a complex role in the fouling behavior of nanoparticles as they interact with the membrane, with the nanoparticles and with other surfactant molecules. This all contributes to the fouling. Our investigation provides some insights in the role of the surfactant on nanoparticle stability and the mechanisms responsible for fouling during filtration of mixtures containing both nanoparticles and surfactants.

References

[1] Willems, v. d. Wildenberg, Roadmap report on nanoparticles, W&W Espana s.l., Barcelona, Spain (2005)

[2] T. E. Abbott Chalew, G. S. Ajmani, H. Huang, K. J. Schwab, Evaluating nanoparticle breakthrough during drinking water treatment, Environ. Health. Perspect. 121 (2013) 1161-1166

[3] A. I. Schäfer, U. Schwicker, M. M. Fischer, A. G. Fane, T. D. Waite, Microfiltration of colloids and natural organic matter, J. Membr. Sci. 171 (2000) 151-172

[4] A. S. Kim, A. E. Contreras, Q. Li, R. Yuan, Fundamental mechanisms of three-component combined fouling with experimental verification, Langmuir 25 (2009) 7815-7827

[5] A. H. Taheri, L. N. Sim, C. T. Haur, E. Akhondi, A. G. Fane, The fouling potential of colloidal silica and humic acid and their mixtures, J. Membr. Sci. 433 (2013) 112-120

[6] P. Aimar, P. Bacchin, Slow colloidal aggregation and membrane fouling, J. Membr. Sci. 360 (2010) 70-76
[7] D. Jassby, S. R. Chae, Z. Hendren, M. Wiesner, Membrane filtration of fullerene nanoparticle suspensions: effects of derivatization, pressure, electrolyte species and concentration, J. Colloid Interface Sci. 346 (2010) 296-302
[8] T. Yin, H. W. Walker, D. Chen, Q. Yang, Influence of pH and ionic strength on the deposition of silver nanoparticles on microfiltration membranes, J. Membr. Sci. 449 (2014) 9-14
[9] Y. Chen, H. Kim, Monte Carlo simulation of pore blocking and cake formation by interfacial interactions during membrane filtration, Desalination 233 (2008) 258-266
[10] S. T. V. Sim, A. H. Taheri, T. H. Chong, W. B. Krantz, A. G. Fane, Colloidal metastability and membrane fouling – Effects of crossflow velocity, flux, salinity and colloid concentration, J. Membr. Sci. 469 (2014) 174-187
[11] J. Labille, J. Brant, Stability of nanoparticles in water, Nanomedicine 5 (2010) 985-998
[12] S. Y. Moon, T. Kusunose, T. Sekino, CTAB-assisted synthesis of size- and shape-controlled gold nanoparticles in SDS aqueous solution, Mater. Lett. 63 (2009) 2038-2040
[13] Z. Tan, H. Abe, M. Naito, S. Ohara, Oriented growth behavior of Ag nanoparticles using SDS as a shape director, J. Colloid Interface Sci. 348 (2010) 289-292
[14] W. Zhang, X. Qiao, J. Chen, Formation of silver nanoparticles in SDS inverse microemulsions, Mater. Chem. Phys. 109 (2008) 411-416
[15] S. Ahualli, G. R. Iglesias, W. Wachter, M. Dulle, D. Minami, O. Glatter, Adsorption of anionic and cationic surfactants on anionic colloids: Supercharging and destabilization, Langmuir 27 (2011) 9182-9192
[16] V. L. Alexeev, P. Ilekti, J. Persello, J. Lambard, T. Gulik, B. Cabane, Dispersions of silica particles in surfactant phases, Langmuir 12 (1996) 2392-2401
[17] G. M. Litton, T. M. Olson, Colloid deposition rates on silica bed media and artifacts related to collector surface preparation methods, Environ. Sci. Technol. 27 (1993) 185-193
[18] G. Singh, L. Song, Influence of sodium dodecyl sulfate on colloidal fouling potential during ultrafiltration, Colloids Surf., A 281 (2006) 138-146
[19] Y. Liu, M. Tourbin, S. Lachaize, P. Guiraud, Silica nanoparticles separation from water: Aggregation by cetyltrimethylammonium bromide (CTAB), Chemosphere 92 (2013) 681-687
[20] Y. Gao, J. Du, T. Gu, Hemimicelle formation of cationic surfactants at the silica gel-water interface, J. Chem. Soc. Faraday Trans. I 83 (1987) 2671-2679
[21] P. Somasundaran, D. W. Fuerstenau, Mechanisms of alkyl sulfonate adsorption at the alumina-water interface, J. Phys. Chem. A 70 (1966) 90-96
[22] F. Giordano-Palmino, R. Denoyel, J. Rouquerol, Interfacial aggregation of a nonionic surfactant: Effect on the stability of silica suspensions, J. Colloid Interface Sci. 165 (1994) 82-90
[23] M. Prasad, R. Palepu, S. P. Moulik, Interaction between sodium dodecyl sulfate (SDS) and polyvinylpyrrolidone (PVP) investigated with forward and reverse component addition protocols employing tensiometric, conductometric, microcalorimetric, electrokinetic, and DLS techniques, Colloid Polym. Sci. 284 (2006) 871-878
[24] S. X. Liu, J.-T. Kim, Study of adsorption kinetics of surfactants onto polyethersulfone membrane surface using QCM-D, Desalination 247 (2009) 355-361

[25] F. Fairbrother, H. Mastin, CCCXII.-Studies in electro-endosmosis. Part I, J. Chem. Soc.,Trans., 125 (1924) 2319-2330
[26] F. P. Cuperus, D. Bargeman, C. A. Smolders, Permporometry. The determination of the size distribution of active pores in UF membranes, J. Membr. Sci. 71 (1992) 57-67
[27] M. A. Khosa, S. S. Shah, M. F. Nazar, UV-visible spectrometric study and micellar enhanced ultrafiltration of alizarin red S dye, J. Dispersion Sci. Technol. 32 (2011) 1634-1640
[28] W. J. C. van de Ven, K. v. t. Sant, I. G. M. Pünt, A. Zwijnenburg, A. J. B. Kemperman, W. G. J. van der Meer, et al., Hollow fiber dead-end ultrafiltration: Influence of ionic environment on filtration of alginates, J. Membr. Sci. 308 (2008) 218-229
[29] P. van der Marel, A. Zwijnenburg, A. Kemperman, M. Wessling, H. Temmink, W. van der Meer, An improved flux-step method to determine the critical flux and the critical flux for irreversibility in a membrane bioreactor, J. Membr. Sci. 332 (2009) 24-29
[30] G. Duplâtre, M. F. Ferreira Marques, M. da Graça Miguel, Size of sodium dodecyl sulfate micelles in aqueous solutions as studied by positron annihilation lifetime spectroscopy, J. Phys. Chem. 100 (1996) 16608-16612
[31] M. S. Bakshi, A. Kaura, J. D. Miller, V. K. Paruchuri, Sodium dodecyl sulfate–poly(amidoamine) interactions studied by AFM imaging, conductivity, and Krafft temperature measurements, J. Colloid Interface Sci. 278 (2004) 472-477
[32] W. Zhang, G. Li, J. Mu, Q. Shen, L. Zheng, H. Liang, et al., Effect of KBr on the micellar properties of CTAB, Chin. Sci. Bull. 45 (2000) 1854-1857
[33] K. Eskilsson, V. V. Yaminsky, Deposition of monolayers by retraction from solution: ellipsometric study of cetyltrimethylammonium bromide adsorption at silica−air and silica−water interfaces, Langmuir 14 (1998) 2444-2450
[34] C. C. Ruiz, J. A. Molina-Bolívar, J. Aguiar, G. MacIsaac, S. Moroze, R. Palepu, Thermodynamic and structural studies of Triton X-100 micelles in ethylene glycol−water mixed solvents, Langmuir 17 (2001) 6831-6840
[35] M. Luckey, Membrane Structural Biology: With Biochemical and Biophysical Foundations: Cambridge University Press, 2014.
[36] S. Kumar, V. K. Aswal, J. Kohlbrecher, Size-dependent interaction of silica nanoparticles with different surfactants in aqueous solution, Langmuir 28 (2012) 9288-9297
[37] R. Atkin, V. S. J. Craig, S. Biggs, Adsorption kinetics and structural arrangements of cationic surfactants on silica surfaces, Langmuir 16 (2000) 9374-9380
[38] S. C. Howard, V. S. J. Craig, Very slow surfactant adsorption at the solid-liquid interface is due to long lived surface aggregates, Soft Matter 5 (2009) 3061-3069
[39] E. Tyrode, M. W. Rutland, C. D. Bain, Adsorption of CTAB on hydrophilic silica studied by linear and nonlinear optical spectroscopy, J. Am. Chem. Soc. 130 (2008) 17434-17445
[40] E. Y. Bryleva, N. A. Vodolazkaya, N. O. McHedlov-Petrossyan, L. V. Samokhina, N. A. Matveevskaya, A. V. Tolmachev, Interfacial properties of cetyltrimethylammonium-coated SiO_2 nanoparticles in aqueous media as studied by using different indicator dyes, J. Colloid Interface Sci. 316 (2007) 712-722
[41] P. Levitz, H. Van Damme, D. Keravis, Fluorescence decay study of the adsorption of nonionic surfactants at the solid-liquid interface. 1. Structure of the adsorption layer on a hydrophilic solid, J. Phys. Chem. 88 (1984) 2228-2235

[42] A.-S. Jönsson, B. Jönsson, The influence of nonionic and ionic surfactants on hydrophobic and hydrophilic ultrafiltration membranes, J. Membr. Sci. 56 (1991) 49-76

[43] J. T. F. Keurentjes, M. A. C. Stuart, D. Brinkman, C. G. P. H. Schroën, K. van 't Riet, Surfactant-induced wetting transitions: Role of surface hydrophobicity and effect on oil permeability of ultrafiltration membranes, Colloids Surf. 51 (1990) 189-205

[44] M. J. Rosa, M. N. de Pinho, Membrane surface characterisation by contact angle measurements using the immersed method, J. Membr. Sci. 131 (1997) 167-180

[45] K. W. Trzaskus, W. M. de Vos, A. J. B. Kemperman, K. Nijmeijer, Towards controlled fouling and rejection in dead-end microfiltration of nanoparticles – role of electrostatic interactions, J. Membr. Sci. 496 (2015) 174–184

[46] G. P. Van der Beek, M. A. C. Stuart, T. Cosgrove, Polymer adsorption and desorption studies via proton NMR relaxation of the solvent, Langmuir 7 (1991) 327-334

[47] R. M. McDonogh, A. G. Fane, C. J. D. Fell, H.-C. Flemming, The influence of polydispersity on the hydraulic behaviour of colloidal fouling layers on membranes: Perturbations on the behaviour of the “ideal” colloidal layer, Colloids Surf., A 138 (1998) 231–244

CHAPTER 6

Axial fouling development of engineered nanoparticles along a microfiltration hollow fiber membrane

Abstract

The extensive application of engineered nanoparticles leads to contamination of surface water by nanoparticles after their use. Membrane technology is one of the most promising techniques to remove these nano-sized pollutants, but still not much is known about the filtration behavior of engineered nanoparticles in terms of efficiency in nanoparticle removal and fouling development. Moreover, fouling development along a hollow fiber membrane during dead-end filtration is not uniform and this can lead to an uneven performance of the membrane along the fiber length.

In this study, non-uniform silica nanoparticle fouling development along microfiltration membrane fibers operated in inside-out dead-end filtration mode under constant flux was investigated. To evaluate the filtration performance along the fiber length, permeate was collected from five equally divided sections of the membrane fiber. The local flux, the filtration resistance and the nanoparticle rejection in each section were determined. This study shows that the lowest filtration resistance is always obtained in the first part of the fiber due to the highest cross-flow occurring at the entrance of the fiber. At higher feed flow rates (0.8 L/h), contradictory results to existing literature were obtained and the middle sections of the membrane revealed a higher resistance than the last section of the fiber.

Nanoparticle rejection increased during the course of the filtration to values above 95%, and it was not significantly influenced by the difference in accumulation of the nanoparticles along the fiber length.

6.1. Introduction

The numerous applications of nanoparticles and their exponentially growing production volume resulted in much concern about their destination after usage [1-3]. Especially surface water is prone to be contaminated by engineered nanoparticles [3-5], from which some are considered as toxic for living organisms [6]. Membrane technology can be a potential solution, since it is able to efficiently purify water containing engineered nanoparticles [7, 8]. However, there is still a lack of knowledge in terms of filtration mechanisms and fouling development during filtration of engineered nanoparticles using polymeric membranes.

Ultra- and microfiltration membranes that can be used for the removal of nanoparticles, are often produced in hollow fiber geometry and may operate in both dead-end as well as in cross-flow mode. However, the term dead-end filtration during inside-out filtration with a hollow fiber membrane is quite misleading, as there is always some cross-flow which reduces over the length of the fiber [9, 10]. Due to these uneven hydrodynamic conditions in a hollow fiber membrane, the performance is not only a function of time but can also depend on the axial position [11, 12].

The observed variations in fouling development over the length of the fiber are caused by the distribution of cross-flow velocity and pressure drop along the fiber [9-11]. These two parameters, however, are significantly influenced by fiber geometry (such as fiber diameter and length) and process parameters (such as flux and concentration) [13, 14]. The higher the aspect ratio between the length and the diameter of the fiber, the higher the pressure drop in axial direction and the more inhomogeneous the fouling is [14]. Hence, shorter fibers exhibit a more uniform fouling, but in practice long hollow fibers modules are used more often. Furthermore, highly permeable hollow fiber membranes such as microfiltration fibers are very sensitive to small variations of the transmembrane pressure or cross-flow velocity along the fiber length. In the extreme case, it even may lead to so-called reverse- or back-filtration at the exit of a membrane module [15]. Moreover, the increasing accumulation of solutes towards the end of the fiber results in different retentions along the fiber length. For example, van de Ven et al. [11] reported that the retention of humic acid dropped drastically at the end of the fiber due to the extensive accumulation of solute causing more pronounced concentration polarization.

As shown in our previous study [16], filtration of rigid nanoparticles much smaller than the membrane pores can result in the formation of a nanoparticle deposit, which acts as a secondary membrane. In that case, concentration polarization and cake formation are beneficial to increase nanoparticle rejection. However, inside-out dead-end filtration

using hollow fiber membranes can lead to non-homogeneous concentration polarization and the formation of a non-uniform cake layer along the length of the fiber length. In fact, this additional cake layer is responsible for the nanoparticle rejection. As a result, fouling and rejection can develop differently along the fiber length. This was investigated before for humic acids [11] and here we investigate the consequences of this non-homogeneous distribution on the filtration behavior in terms of fouling and rejection uniformity of engineered nanoparticles along a hollow fiber during hollow fiber dead-end microfiltration.

6.2. Experimental

6.2.1. Materials

Silica nanoparticles Ludox TM-50 were purchased from Sigma Aldrich as a 50% w/w water suspension. The properties of the nanoparticles were investigated and reported elsewhere [16]. Summarizing, the number average size of the nanoparticles was found to be 25.5 ± 5.2 nm (as measured with Transmission Electron Microscopy), and the zeta potential was reported as -37.7 ± 3.9 mV (at pH 8). ACS grade NH_4HCO_3, $(NH_4)_2CO_3$, HCl and NaOH (Sigma Aldrich) were used to adjust the pH and the ionic strength of the feed solution. All chemicals were used without further purification and all solutions were prepared using Milli-Q water (resistivity >18.2 MΩ·cm).

6.2.2. Membrane and membrane characterization

Pentair X-Flow B.V. kindly supplied the commercially available Pentair X-Flow 1.5MF02 inside-out PES-PVP microfiltration (MF) hollow-fiber membranes. The clean-water permeability of the applied membrane was measured as 11000 ± 500 $L/m^2 \cdot h \cdot bar$. A detailed characterization of the membrane is reported elsewhere [16]. The average pore size of the membrane as measured with capillary flow porometry (Porolux^{TM} 1000, Porometer N.V.) was 200 ± 15 nm. The membrane surface zeta potential at the inside of the fiber determined from streaming potential measurements (SurPass, Anthon Paar GmbH) was -23.1 ± 2.1 mV.

One single fiber (inner diameter: 1.5 mm) was potted at its ends in 8 mm PVC tubes with two-component polyurethane glue 2K Expert **(**Bison International B.V.). The part of the fiber between the two PVC tubes (36 cm) was open to the air and divided into five permeating sections with a length of 4 cm (effective membrane area: $9.4 \cdot 10^{-4}$ m^2). The permeating sections were separated by non-permeating sections of 4 cm each as well,

which were obtained by covering the membrane fiber from the outside with the polyurethane glue. A schematic illustration of the filtration module is shown in Fig. 1.

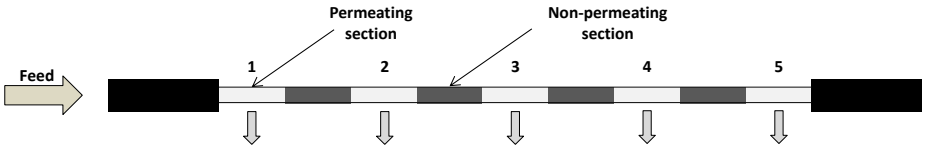

Fig. 1. Schematic description of used hollow fiber module divided into five permeating sections.

6.2.3. Filtration experiments

All the feed solutions were prepared by diluting the commercial Ludox TM-50 silica nanoparticle suspension in 1 mM bicarbonate buffer at pH 8. The concentration of nanoparticles in all experiments was 10 mg/L. The filtrations experiments were carried out at constant flux (i.e. constant feed flow rate) in inside-out dead-end mode using an OSMO Inspector filtration setup (Convergence Industry B.V.), of which a schematic description is given in Fig. 2.

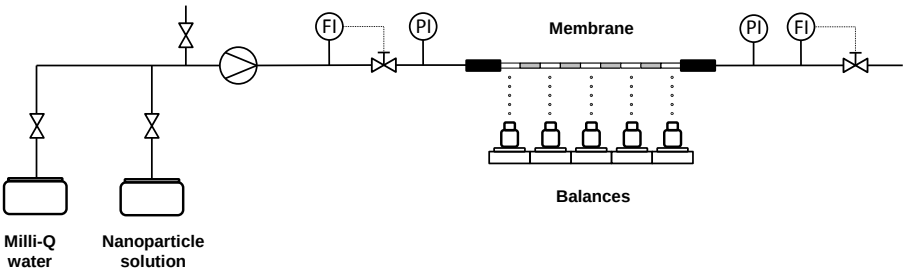

Fig. 2. Schematic description of the applied OSMO Inspector setup for inside out dead-end filtration.

Before filtration of the nanoparticles, Milli-Q water was pumped through the prepared membrane module by a gear pump (Micropump GA-T23, Micropump Inc.). A constant volumetric feed flow rate was maintained by high precision mass flow controllers (Cori-Flow^{TM}, model M53 and M14, Bronkhorst High-Tech B.V.). The amount of permeate collected from each of the five permeating sections of the membrane was monitored continuously using precision balances (Kern KB, Kern & Sohn GmbH). The pressure at the inlet and outlet of the membrane module were monitored with high accuracy piezoresistive pressure transducers (Omega PXM409, Omega Engineering Inc.). After

about 10 minutes of clean water filtration, the nanoparticle solution was fed to the filtration module by opening the appropriate valve. Filtration was stopped when about 1.5 L of nanoparticle solution was filtered or when the maximum allowed pressure of 9 bar was reached. Each experiment was repeated at least three times at a controlled room temperature (20 ± 1ºC). The results were averaged and reported.

6.2.4. Cross-flow and flux along the fiber

Solely inside-out dead-end filtration with hollow fiber membranes in fact does not exist. In the case of a module fed only from one side, distribution of the liquid inside the fiber causes different cross-flows over the length of the membrane fiber. This cross-flow is highest at the entrance of the module, and goes to zero at its exit due to the closed end of the fiber. Moreover, flow of the liquid inside the fiber causes a pressure drop. This results in a non-uniform flux distribution along the fiber length. Like van de Ven et al. [11], we used a system of two differential equations (Eq. 1) to describe the cross-flow velocity and transmembrane pressure during filtration of pure water as a function of the position z along the fiber. The first equation in Eq. 1 is derived from a mass balance combined with D'Arcy's law and taking into account permeation through the porous membrane wall. The second equation is the Hagen-Poiseuille equation, which describes the pressure drop in the lumen of the fiber [10].

$$\frac{d}{dz}v(z) = -\frac{2 \cdot P(z)}{\eta \cdot r \cdot R_m} \qquad (1)$$

$$\frac{d}{dz}P(z) = -\frac{8 \cdot \eta \cdot v(z)}{r^2}$$

In Eq. 1, v is the cross-flow velocity (m/s), P is the transmembrane pressure (Pa), z is the axial coordinate (m), η is the viscosity of water (Pa·s), r is the radius of the fiber (m), and R_m is the resistance of the membrane (1/m). The boundary conditions used to solve this system of differential equations were $v(0) = Q/A$ (resulting from the feed flow at the entrance of the fiber) and $v(L_{tot}) = 0$ (the velocity is zero at the end of the module), where Q is the volumetric flow rate of the feed solution (m^3/s), A is the cross-sectional area of the fiber (m^2), and L_{tot} is the total length of the fiber (m). The equations were solved analytically using Matlab R2013a software (MathWorks).

6.2.5. Data processing

In the experiments, the transmembrane pressure (TMP) and the accumulated permeate mass were monitored in time. The local permeate flux was calculated then according to Eq. 2:

$$J = \frac{\Delta V}{\Delta t} \cdot \frac{1}{\pi \cdot d \cdot L} \quad (2)$$

where J is the permeate flux (L/m^2·h), V the volume of permeate calculated from the accumulated permeate mass monitored by the precision balances (m^3), t the filtration time (s), L is the length of a single membrane section (m) and d is the fiber diameter (m). The total hydraulic resistance was calculated using Eq. 3:

$$R = \frac{\Delta P}{\eta \cdot J} \quad (3)$$

where R is the resistance (1/m), ΔP the transmembrane pressure (Pa) and η the viscosity of the feed solution (Pa·s). As the pressure could only be measured at the module entrance and exit, resistances for individual fiber sections were calculated taking into account local fluxes and assuming the same transmembrane pressure in every section. The transmembrane pressure was calculated as an arithmetic average from the pressure value measured at the module entrance and the module end. We think this approach is acceptable as the absolute pressure difference between the module entrance and the module end was never higher than 5 mbar. This is significantly below the accuracy of the pressure transducers in the set-up (8 mbar). Permeate was collected in batches of 50 mL. To determine the nanoparticle concentration in the feed and permeate samples, ICP-MS (Inductively Coupled Plasma Mass Spectrometry, Thermo Fisher Xseries 2) was used. The silica nanoparticle rejection was calculated according to Eq. 4:

$$\sigma = 1 - \frac{C_p}{C_f} \quad (4)$$

where σ is the rejection (-), C_P is the concentration of the nanoparticles in the permeate (mg/L), and C_F is the concentration of the nanoparticles in the feed solution (mg/L).

6.3. Results and Discussion

6.3.1. Cross-flow velocity, pressure and local fluxes along the fiber for pure water filtration

Permeation of the feed as well as the varying hydrodynamic resistance towards flow along the fiber lead to a distribution of the cross-flow velocity, pressure and the

local fluxes over the fiber length. This variation in hydrodynamic conditions can affect the local flux and shear forces inside the fiber and this can affect the fouling and rejection development along the hollow fiber membrane. In order to describe the hydrodynamics for pure water in the applied filtration module, the system of differential equations given in Eq. 1 was solved for the experimental conditions applied. In the calculations, we used the resistance of the membrane ($3.1 \cdot 10^{10}$ 1/m) [16], the total length of the permeating part of the membrane (20 cm) and three volumetric feed flow rates: 0.2 L/h, 0.5 L/h and 0.8 L/h. The results of the calculations of the axial velocity and the pressure profile along the fiber length are given in Fig. 3.

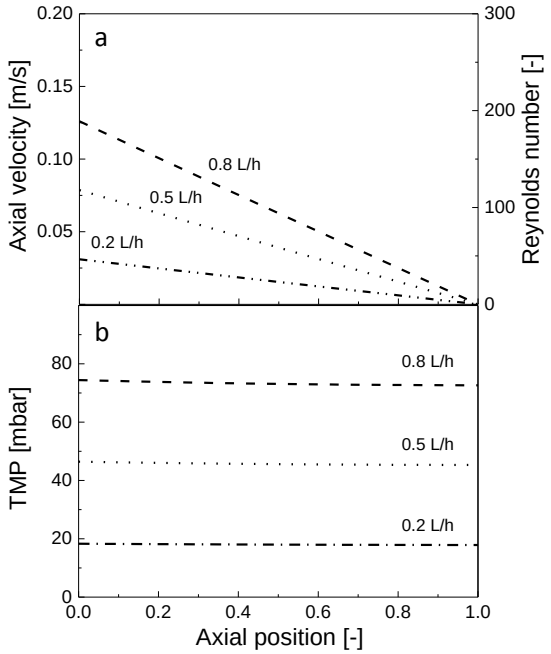

Fig. 3. a) Calculated axial velocity/Reynolds number and b) transmembrane pressure (TMP) along the applied hollow fiber microfiltration membrane as a function of the axial position in the module during dead-end filtration of pure water. The calculations are obtained for three volumetric feed flow rates (0.8 L/h, 0.5 L/h and 0.2 L/h). Axial position = 0 is the entrance of the fiber, and axial position = 1.0 is the end of the fiber. R = $3.1 \cdot 10^{10}$ 1/m [16], r = $1.5 \cdot 10^{3}$ m, $\eta = 1 \cdot 10^{-3}$ Pa·s.

The calculations show that the axial velocity and the pressure difference over the membrane decrease near-linearly over the fiber length. When using a hollow fiber membrane in constant flux dead-end mode, the axial velocity is the highest at the

entrance and decreases to zero at the end of the membrane. The initial cross-flow velocity at the fiber entrance is proportional to the volumetric feed flow rate, so the higher the volumetric feed flow rate, the higher the cross-flow velocity at the entrance of the fiber. The decline of the axial velocity is greater for higher volumetric feed flow rates applied, as at the end of the fiber the feed flow rate is zero (Fig. 3a). The range of cross-flows investigated shows that all the experiments are carried out in the laminar flow regime (Re << 2100) [17] and that the maximum cross-flow velocity, obtained for a feed flow rate of 0.8 L/h, was 0.125 m/s at the module entrance (see Fig 3a). As shown in Fig. 3b, for the filtration of pure water, the calculated transmembrane pressure decreases slightly with fiber length (2.4%). The pressure in the fiber declines towards the end of the module, mainly due to the hydraulic resistance to flow inside the capillary and the permeation of water through the porous membrane. Consequently, the driving force for water permeation (the transmembrane pressure) decreases slightly over the fiber length. This reduction in driving force results in a decrease of the local flux with the length of the membrane. We confirmed this effect of the reduction in driving force on the local flux experimentally (Fig. 4). The decline in local flux over the fiber length is in agreement with observations reported in literature (e.g. van de Ven et al. [11]) describing axial transport variations during dead-end hollow fiber membrane operation.

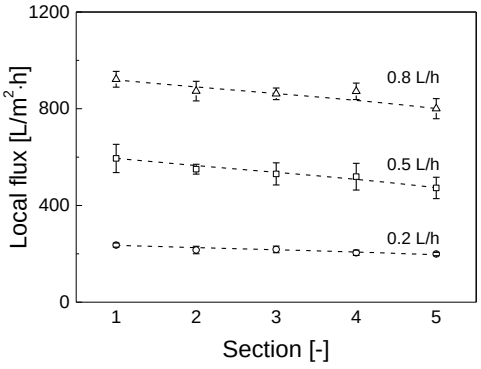

Fig. 4. Experimentally determined local fluxes during hollow fiber dead-end microfiltration of clean water for the five fiber sections, at three different feed flow rates: 0.2 L/h, 0.5 L/h and 0.8 L/h.

6.3.2. Fouling development along the fiber length

The differences in hydrodynamics inside a microfiltration hollow fiber (Figs. 3a and 3b) cause variations in local flux along the fiber length (Fig. 4). For feed solutions containing nanoparticles, this will result in fouling development that is not only time dependent but also depends on the position along the fiber length. The fouling behavior as a function of the axial position in the fiber is investigated experimentally for a feed flow rate of 0.5 L/h. Fig. 5 shows the local flux development as a function of the filtration time during hollow fiber dead-end filtration of 10 mg/L silica nanoparticles for the five fiber sections.

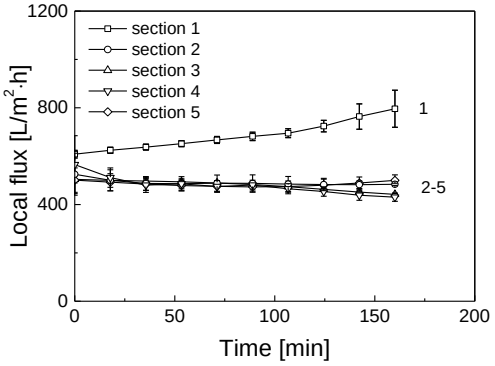

Fig. 5. Experimentally determined local fluxes for the five fiber sections as a function of the filtration time during microfiltration of 10 mg/L silica nanoparticles at pH 8 and at a constant volumetric feed flow rate of 0.5 L/h.

Fig. 5 shows that during filtration, the permeate flux in section 1 increases significantly with time, whereas in the same period in sections 2-5 the local permeate flux declines slightly. This is due to nanoparticle deposition and fouling. An increasing flux in time and the least severe fouling in section 1 of the fiber stems from the fact that at the fiber entrance experiences the highest cross-flow velocity, as is shown in Fig. 3a. The higher shear force in section 1 reduces the deposition of the nanoparticles and facilitates their transport towards the end of the fiber [9, 11]. This phenomenon causes an increase of the nanoparticle deposit thickness towards the end of the fiber in sections 2-5 [9, 11, 14], as schematically shown in Fig. 6. Due to accumulation of the nanoparticles in sections 2-5 the local permeate flux decreases in these sections, as can be seen in Fig. 5. In order to maintain a constant permeate flux (notice the constant feed flow of 0.5 L/h imposed)

through the whole membrane, the reduced local permeate flux in sections 2-5 has to be balanced by an increase in the local permeate flux in section 1.

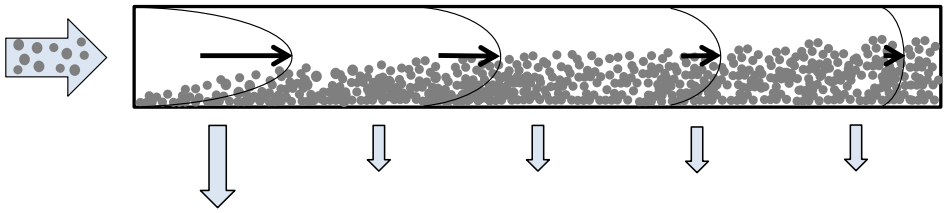

Fig. 6. Schematic representation of nanoparticle deposition inside a hollow fiber membrane during dead-end operation (adapted from van de Ven at al. [11]). Horizontal arrows indicate cross-flow velocity inside the fiber, whereas the parabolas show the laminar flow profile; the vertical arrows are the local permeate fluxes along the length of the fiber.

Deposition of nanoparticles on the membrane surface causes an increase of the filtration resistance. Fig. 7 shows the development of the resistance as a function of the permeate volume for the five fiber sections investigated. Due to differences in the local fluxes (Fig. 5), the resistance increase is not uniform for all fiber sections. The highest resistance and the strongest resistance increase is observed in sections 2-5 and significantly lower resistance increase is observed in section 1. Moreover, as a result of the non-uniform distribution of local fluxes, the collected amount of permeate is the highest for section 1 (approx. 350 mL) in comparison to the sections 2-5 (approx. 250 mL per section), as shown in Fig. 7.

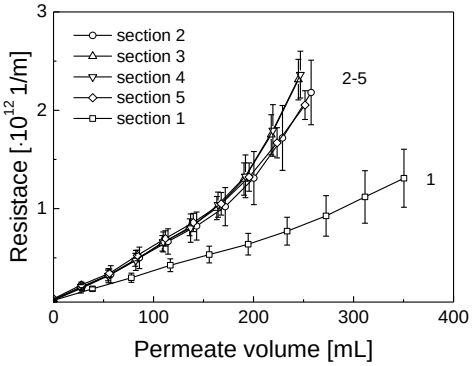

Fig. 7. Resistance as a function of permeate volume during filtration of 10 mg/L silica nanoparticles at pH 8 at a constant volumetric feed flow rate of 0.5 L/h for the five fiber sections.

Since fouling develops differently along the length of the membrane we expect that also nanoparticle rejection will depend on the axial position in the hollow fiber membrane, similarly to what was reported by van de Ven et al. for humic acid filtration [11]. Furthermore, the large difference between the pore size of the membrane (~200 nm) and the nanoparticle diameter (~25 nm) results in a slow increase of the rejection during the pore blockage stage, as described in our previous work [16]. Fig. 8 shows the initial nanoparticle rejection (at the beginning of the filtration process) and the final nanoparticle rejection (at the end of the filtration process) for the five fiber sections.

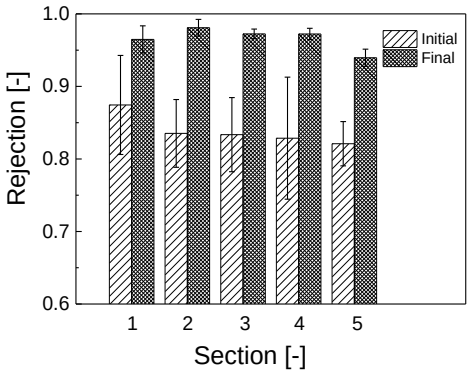

Fig. 8. Initial (first permeate sample) and final (last permeate sample) nanoparticle rejection for the five fiber sections obtained during filtration of 10 mg/L silica nanoparticles at pH 8 and at a constant volumetric feed flow rate of 0.5 L/h.

The nanoparticle rejection increases for all fiber sections from approx. 0.83-0.87 (initial sample) to 0.98 (final sample) during a filtration experiment. The relatively high flux applied (compared to normal operation of UF membranes) immediately results in the transport of nanoparticles towards the membrane surface, followed by their deposition and pore blockage. Subsequently, a filtration cake is formed that acts as a secondary membrane enhancing nanoparticle rejection. Since accumulating nanoparticles increase the thickness of the nanoparticle deposit, the nanoparticle rejection will be enhanced for all membrane sections during the filtration course. The difference in nanoparticle rejection between the five fiber sections is negligible when the error bars in Fig. 8 are considered. Contrary to the findings of van de Ven et al. who observed a decrease in humic acids rejection with the length of the fiber [11] apparently in this configuration for silica nanoparticles the rejection is not dependent on the axial position in the hollow fiber membrane. An increasing nanoparticle concentration along the fiber does result in

increased concentration polarization, but apparently this does not reduce nanoparticle rejection. We think that the monodisperse silica nanoparticles form an additional barrier that is less prone to be influenced by concentration polarization than the for soft and polydispersed humic acids used by van de Ven et al. [11]. We speculate that differences in softness, size and polydispersity between silica nanoparticles and humic acids are responsible for the different behavior in terms of rejection. For smaller, softer and polydisperse humic acid, diffusion through the deposit is more likely to occur, whereas significantly larger, more rigid and monodisperse nanoparticles have more difficulties to be transported through the filtration cake by means of diffusion.

6.3.3. Effect of the feed flow rate

The feed flow rate applied determines the convective flux through the membrane and the hydrodynamic conditions such as cross-flow velocity and transmembrane pressure inside the hollow fiber (see Figs. 3a and 3b). In order to investigate the influence of the applied feed flow rate on the uniformity of the fouling along the fiber length, 10 mg/L silica nanoparticles were filtered at feed flow rates of 0.2 L/h, 0.5 L/h and 0.8 L/h. The local fluxes as a function of the filtration time for the three feed flow rates investigated are given in Fig. 9. For clarity, we plotted only the results for the first section (1), the middle section (3) and the last section (5).

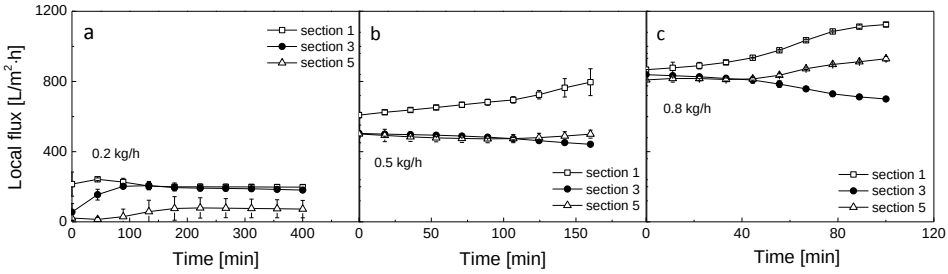

Fig. 9. Local fluxes for three fiber sections as a function of time during filtration of 10 mg/L silica nanoparticles at pH 8 at volumetric feed flow rates of a) 0.2 L/h, b) 0.5 L/h and c) 0.8 L/h.

A comparison of Figs. 9a, 9b and 9c shows that an increase of the feed flow rate results in a higher local flux for all fiber sections. Moreover, development of the local flux in time varies with the feed flow rate applied. At the reference feed flow rate of 0.5 L/h the local flux increases only in the first fiber section, whereas in other fiber sections the local flux slightly decreases or is stable.

In the case of a feed flow rate of 0.2 L/h (Fig. 9a) the first section also initially exhibits the highest local flux but after about 100 min this local flux in this section stabilizes. This behavior is quite expected since in this section the highest cross-flow is imposed resulting in the lowest amount of fouling in this section. Similar behavior is observed for middle section (3), whereas flux increases slowly with time to the same value as for first section (1). Furthermore, as expected, the lowest local flux was obtained in the last section (5) due to accumulation of the nanoparticles.

For the highest feed flow rate applied (0.8 L/h), also the local flux in the initial section is highest and it increases during filtration (Fig. 9c). At the same time, the flux in the middle section (3) decreases, whereas the flux in the last section increases again with time. The reduction of the flux in the middle part of the fiber is explained as before by extensive fouling due to the lowered cross-flow velocity allowing deposition of nanoparticles transported towards the end of the module (section 6.3.2). Since at the end of the fiber the cross-flow is the lowest and even decreases to zero, and since the nanoparticles are transported to the end of the fiber where they are assumed to deposit to the largest extend, we expect a greater decrease of the flux at the end of the fiber. In contrast to the results obtained for feed flow rates of 0.2 L/h and 0.5 L/h, this is not the case for 0.8 L/h. We think that an increase of the flux in the last fiber section originates from the dynamics of the fouling development and the initial distribution of the fluxes along the fiber length. A slightly higher flux in the middle part of the module (section 3) than in the last section (section 5) directly from the beginning of the filtration, in combination with transport of nanoparticles from the 1st section to the 3rd section, might have resulted in the preferential formation of a compact cake structure in the middle of the fiber. This causes the initially high flux in section 3 to become smaller in time. Consequently, taking into account conservation of the mass, this reduced flux in the middle of the fiber not only leads to a higher flux in the initial (section 1) but apparently in this case also in the last section (section 5) of the fiber. An increase of the flux at the fiber end and the minimal cross-flow there should result in acceleration of the fouling and extensive nanoparticle deposition. However, this is not the case here and we do not have a satisfactory explanation for this behavior. We suggest additional studies on fluid dynamics, which could help in understanding this unusual distribution of the local fluxes.

The nanoparticle rejection at the beginning of the filtration and at its end for three fiber sections (1, 3, 5) and for three different feed flow rates is shown in Fig. 10.

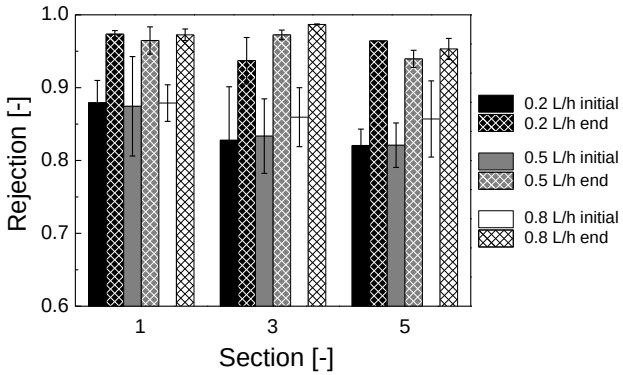

Fig. 10. Initial (first permeate sample) and final (last permeate sample) nanoparticle rejection for three fiber sections (1,3,5) obtained during filtration of 10 mg/L silica nanoparticles at pH 8 and at various volumetric feed flow rates (0.2 L/h, 0.5 L/h and 0.8 L/h).

Despite the differences in the fluxes for the different feed flow rates in the different sections, the rejections only show differences when the initial and the final values are compared. Independent of the feed flow rate, all initial rejections show the same values and all the final rejections as well. The higher final rejections compared to the initial ones are most probably due to an increasing thickness of the nanoparticle deposit with increasing time. This layer acts as a secondary membrane, and diffusion of nanoparticles through the filtration cake and membrane becomes is more difficult. Therefore, the final rejections for all investigated fiber sections and feed flow rates are above 0.95, regardless of the feed flow rate applied.

6.4. Conclusions

Uniformity of fouling development upon filtration of silica nanoparticles along a hollow fiber membrane was studied in inside-out dead-end microfiltration under a constant feed flow rate. This work clearly shows that fouling development is axially non-uniform due to differences in hydrodynamic conditions over the length at the inside of the fiber. It was observed that during dead-end hollow fiber microfiltration of silica nanoparticles the highest local flux always is obtained at the beginning of the fiber due to the highest cross-flow generated there. The lowest local flux was observed in the middle section of the fiber at the highest investigated feed flow rate of 0.8 L/h, whereas for the lower feed flow rates (0.2 L/h and 0.5 L/h) the last fiber section exhibited the lowest local flux. Nanoparticle rejection increased during the filtration course due to pore blocking and

subsequent formation of a filtration cake acting as a secondary membrane retaining nanoparticles. No significant influence of the axial position on the nanoparticle rejection was observed. After formation of the nanoparticle deposit on the membrane surface, nanoparticle rejection above 0.95 regardless of the axial position in the fiber.

References

[1] F. Piccinno, F. Gottschalk, S. Seeger, B. Nowack, Industrial production quantities and uses of ten engineered nanomaterials in Europe and the world, J. Nanopart. Res. 14 (2012) 1-11

[2] S. F. Hansen, E. S. Michelson, A. Kamper, P. Borling, F. Stuer-Lauridsen, A. Baun, Categorization framework to aid exposure assessment of nanomaterials in consumer products, Ecotoxicology 17 (2008) 438-47

[3] H. Weinberg, A. Galyean, M. Leopold, Evaluating engineered nanoparticles in natural waters, Trends. Anal. Chem. 30 (2011) 72-83

[4] T. V. Duncan, K. Pillai, Release of engineered nanomaterials from polymer nanocomposites: Diffusion, dissolution, and desorption, ACS Appl. Mater. Interfaces 7 (2015) 2-19

[5] Y. Liu, M. Tourbin, S. Lachaize, P. Guiraud, Nanoparticles in wastewaters: Hazards, fate and remediation, Powder Technol. 255 (2014) 149-156

[6] A. Elsaesser, C. V. Howard, Toxicology of nanoparticles, Adv. Drug Deliv. Rev. 64 (2012) 129-137

[7] A. I. Schäfer, U. Schwicker, M. M. Fischer, A. G. Fane, T. D. Waite, Microfiltration of colloids and natural organic matter, J. Membr. Sci. 171 (2000) 151-172

[8] S. Surawanvijit, M. Kim, Y. Cohen, Analysis of membrane filtration efficiency in removal of metal oxide nanoparticles from aqueous nanoparticle suspension in the presence of coagulation pretreatment, Clean Technology F(2010) 343 - 345

[9] S. Panglisch, R. Gimbel, Formation of layers of non-Brownian particles in capillary membranes pperated in dead-end mode, J. Chin. Ins. Chem. Eng. 35 (2004) 77-85

[10] S. Chang, A. G. Fane, T. D. Waite, Analysis of constant permeate flow filtration using dead-end hollow fiber membranes, J. Membr. Sci. 268 (2006) 132-141

[11] W. J. C. van de Ven, K. van't Sant, I. G. M. Pünt, A. Zwijnenburg, A. J. B. Kemperman, W. G. J. van der Meer, et al., Hollow fiber dead-end ultrafiltration: Axial transport variations during humic acid filtration, J. Membr. Sci. 314 (2008) 112-122

[12] C. Gourgues, P. Aimar, V. Sanchez, Ultrafiltration of bentonite suspensions with hollow fiber membranes, J. Membr. Sci. 74 (1992) 51-69

[13] T. Carroll, The effect of cake and fibre properties on flux declines in hollow-fibre microfiltration membranes, J. Membr. Sci. 189 (2001) 167-178

[14] Y. Bessiere, D. F. Fletcher, P. Bacchin, Numerical simulation of colloid dead-end filtration: Effect of membrane characteristics and operating conditions on matter accumulation, J. Membr. Sci. 313 (2008) 52-59

[15] E. Binabaji, J. Ma, S. Rao, A. L. Zydney, Theoretical analysis of the ultrafiltration behavior of highly concentrated protein solutions, J. Membr. Sci. 494 (2015) 216-223

[16] K. W. Trzaskus, W. M. de Vos, A. Kemperman, K. Nijmeijer, Towards controlled fouling and rejection in dead-end microfiltration of nanoparticles – Role of electrostatic interactions, J. Membr. Sci. 496 (2015) 174-184

[17] H. Chanson, "Applications of the momentum principle: Hydraulic jump, surge and flow resistance in open channels," in Hydraulics of Open Channel Flow, H. Chanson, Ed., 2 ed Oxford: Butterworth-Heinemann, 2004, pp. 50-93.

CHAPTER 7

General conclusions and outlook

7.1. Conclusions

This thesis clearly demonstrates the strong influence of particle-particle interactions between nanoparticles in the feed solution on rejection and fouling development during nanoparticle membrane filtration.

Chapter 2 shows that during dead-end microfiltration of electrostatically stabilized monodisperse silica nanoparticles, fouling develops in five stages: adsorption, nanoparticle transport through the membrane, pore blockage, cake filtration and cake maturation. In the latter case, approx. 90% nanoparticle rejection is possible, even with hollow fiber membranes having pores 8 times larger than the nanoparticle diameter. This is due to the formation of a filtration cake on the membrane surface that acts as a secondary membrane. Reduced electrostatic repulsion between nanoparticles (due to increased ionic strength, pH or addition of multivalent cationic salt ions) allows earlier pore blockage and the formation of a denser filtration cake, which enhances nanoparticle rejection at the expense of a lower permeability.

In **Chapter 3** the effect of polydispersity of the electrostatically stabilized nanoparticles in the feed solution is investigated. The results show that fouling and rejection of suspensions with smaller and bigger particles develops in between the results obtained for both monodisperse nanoparticles. Moreover, the formed filtration cake is still permeable for smaller nanoparticles due to electrostatic repulsions and possible defects in the filtration cake. Compaction of the filtration cake at higher transmembrane pressures does not enhance significantly the nanoparticle rejection.

Chapter 4 describes the role of a common steric stabilizer PVP (polyvinylpyrrolidone) and its behavior in microfiltration of silica nanoparticles. The results elucidate that the concentration of PVP, its molecular mass and the transmembrane pressure applied significantly influence the filtration behavior of the nanoparticles. For low molecular weight PVP, an increase of its concentration results in longer transport through the pores due to reduced aggregation of the nanoparticles on the membrane surface and delayed formation of a filtration cake. This effect is less pronounced at higher PVP concentrations due to the contribution of the PVP itself to fouling. Delayed pore blockage is less distinct with an increase of molecular mass although larger stabilizer molecules can easily block the pores. An increase of the transmembrane pressure applied results in compaction of the filtration cake, thereby improving the nanoparticle rejection.

The role of anionic (SDS, sodium dodecyl sulphate), cationic (CTAB, cetyltrimethylammonium bromide), and non-ionic (Triton X-100) surfactants added to

the feed solution is investigated in **Chapter 5.** An increased concentration of surfactants in the nanoparticle-surfactant mixture contributes significantly to the filtration resistance for all surfactants investigated, even though rejection of the surfactants could not be measured. The most severe fouling and the highest nanoparticle rejection is observed for non-ionic Triton X-100, due to significantly reduced repulsive interactions between the nanoparticles and the formation of a compact nanoparticle deposit on the membrane surface.

Chapter 6 shows that the hydrodynamic conditions during inside-out dead-end filtration using a hollow fiber membrane can result in a variation in fouling development over the fiber length. Fouling behavior along the fiber is strongly determined by the applied feed flow rate. Nevertheless, unexpectedly, rejection of nanoparticles is not significantly influenced by the axial position and associated extensive concentration polarization occurring in some parts of the hollow fiber membranes.

7.2. Outlook

Physico-chemical properties of nanoparticles have a profound effect on their filtration behavior using polymeric membranes. The variety of nanoparticle types present, possible stabilizers that can be applied, and specific nanoparticle properties complicate a general and accurate prediction of the filtration behavior of engineered nanoparticles as a group. Future work on membrane filtration of engineered nanoparticles should mainly focus on revealing fundamental phenomena occurring inside the membrane pore, and the membrane-feed interface and inside the filtration cake.

7.2.1. Fouling observation

Chapter 3 and Chapter 4 show that nanoparticles can be transported through the nanoparticle deposit formed on the membrane surface, reducing their rejection in the cake filtration stage. We hypothesized that the origin of such behavior is the strong repulsive interaction between nanoparticles and reduced ordering of the filtration cake. Nevertheless, direct observation of nanoparticles during filtration and their behavior at the membrane surface would bring an additional level of understanding. The difficulty, however, is related to the size of the nanoparticles, as the particles cannot be observed by classical optical microscopes or high speed cameras. Nevertheless, exponential progress in fluorescent microscopy allows the observation of objects with sizes below 100 nm

after preparation of the sample with appropriate fluorescent dye [1]. In that case, the nanoparticles in the feed can be monitored during the filtration process. Moreover, investigation of more complicated feeds (e.g. polydisperse nanoparticles or sterically stabilized nanoparticles) would also be possible by applying markers for the more interesting fractions in the feed solution. Of course, equally important is the preparation of the microfluidic chip necessary to visualize the particles, which could resemble a model membrane. Such a microchip can be prepared e.g. from PDMS (polydimethylsiloxane) rubber similarly to the one presented in the work of Bacchin et al. [2] or Marty et al. [3]. Nevertheless, downscaling of the pore size in the microfluidic chip is necessary since in the work of Bacchin et al. [2] the pore mouth has a size of about 20 μm, which is definitely too large to investigate ultra- or microfiltration of nanoparticles. In order to further study the effects described in this thesis, the pore size of the chip should be at least approx. 500 nm. Application of photolithographic techniques in the preparation of the microfluidic chip allow the formation of approx. 80 nm channels [4], which may act as model UF or MF membrane pores

7.2.2. Fouling: modeling versus experiment

Mathematical models are necessary for the fundamental understanding of the phenomena occurring during membrane filtration. Especially models that take into account phase transitions of the nanoparticles [5] and local hydrodynamics [6] in a hollow fiber membranes during filtration, can be helpful for the explanation of the phenomena occurring during nanoparticle filtration. Often, however, good models are not only very complex but also difficult in assessing their validity with regard to the experimental results. Due to simplifications and multiple parameters omitted by these models, such verification of fouling models is often challenging. Ideally, the experimental setup used for the validation of a theoretical model should be as simplified and as idealized as is possible. Development of a microfluidic platform (as proposed in section 7.2.1.) that provides stable and tunable properties of the filter after many tests can be an answer for this problem. Moreover, chosen modeling approaches set the window for model validation. In general, results obtained from stochastic approaches such as diffusion-limited aggregation or other stochastic particle-based methods [7, 8] are obtained for single pore systems, which can be computationally prohibitive to expand to a larger system with pore-size distributions, including surface roughness effects, etc.

This motivates the use of simpler continuum macroscale models, such as a finite element approach [6].

7.2.3. Choice of model nanoparticles

Engineered nanoparticles can be classified into different groups according to their mechanism of stabilization, their toxicity and their physical or chemical properties. In this work, silica nanoparticles were selected as a model nanoparticle representative for a broader group of electrostatically stabilized nanoparticles. Our choice was based on their high suspension stability in water, easy availability of various sizes and surface properties. Nevertheless, further studies should focus on nanoparticles representative also for other nanoparticle groups. For example, nanoparticles having a proven negative influence on living organisms such as carbon nanotubes, metal nanoparticles or heavy metal nanoparticles [9] can be examined in terms of their removal from water using membranes. Other interesting parameters to investigate can be rigidity and deformability of the nanoparticles and the influence on nanoparticle rejection [10]. In chapter 6 we showed that for rigid monodisperse silica nanoparticles, concentration polarization does not influence their rejection, whereas van der Ven et al. [11] reported that in the case of soft and polydisperse humic acid, severe concentration polarization results in a drop of the rejection. Consequently, under some conditions, filtration of rigid metal, metal oxide or cross-linked polymeric nanoparticles can be considerably different than filtration of microgels, proteins or viruses.

7.2.4. Synergic fouling

The results in Chapter 4 and Chapter 5 of this thesis clearly demonstrate the importance of synergic effects between nanoparticles and various additives present in the nanoparticle suspension on the filtration behavior of the nanoparticles. Further studies on the role of such additives on particle-particle and membrane-particle interactions need to be carried out in order to fully understand the filtration behavior of the nanoparticles in more challenging feed solutions, such as surface or produced waters. Due to the complexity of the feed solution, the membrane-additive, additive-particle and membrane-particle interactions should be investigated separately on model systems prior the investigation of complex feed solutions. Only the combination of the results obtained for simplified cases can give valid insights helpful in fouling description of complex feed solutions. However, due to the various types of additives used, this task requires first a

definition of representative groups, which would cover the whole spectrum of interesting stabilizers.

References

[1] T. Ha, P. Tinnefeld, Photophysics of Fluorescence Probes for Single Molecule Biophysics and Super-Resolution Imaging, Annu. Rev. Phys. Chem. 63 (2012) 595-617

[2] P. Bacchin, A. Marty, P. Duru, M. Meireles, P. Aimar, Colloidal surface interactions and membrane fouling: Investigations at pore scale, Adv. Colloid Interface Sci. 164 (2011) 2-11

[3] A. Marty, C. Roques, C. Causserand, P. Bacchin, Formation of bacterial streamers during filtration in microfluidic systems, Biofouling 28 (2012) 551-562

[4] D. S. Engstrom, B. Porter, M. Pacios, H. Bhaskaran, Additive nanomanufacturing – A review, J. Mater. Res. 29 (2014) 1792-1816

[5] P. Harmant, P. Aimar, Coagulation of colloids retained by porous wall, AIChE J. 42 (1996) 3523-3532

[6] Y. Bessiere, D. F. Fletcher, P. Bacchin, Numerical simulation of colloid dead-end filtration: Effect of membrane characteristics and operating conditions on matter accumulation, J. Membr. Sci. 313 (2008) 52-59

[7] M. Wessling, Two-dimensional stochastic modeling of membrane fouling, Sep. Purif. Technol. 24 (2001) 375–387

[8] J. C. Chen, M. Elimelech, A. S. Kim, Monte Carlo simulation of colloidal membrane filtration: Model development with application to characterization of colloid phase transition, J. Membr. Sci. 255 (2005) 291-305

[9] C. M. Keck, R. H. Müller, Nanotoxicological classification system (NCS) – A guide for the risk-benefit assessment of nanoparticulate drug delivery systems, Eur. J. Pharm. Biopharm. 84 (2013) 445-448

[10] G. H. Meeten, Septum and filtration properties of rigid and deformable particle suspensions, Chem. Eng. Sci. 55 (2000) 1755-1767

[11] W. J. C. van de Ven, K. van't Sant, I. G. M. Pünt, A. Zwijnenburg, A. J. B. Kemperman, W. G. J. van der Meer, et al., Hollow fiber dead-end ultrafiltration: Axial transport variations during humic acid filtration, J. Membr. Sci. 314 (2008) 112-122

Summary

Sustainable development requires focus not only on the advantages of a certain technology, but also on its drawbacks and threats. The same is valid for nanotechnology, involving the manufacturing and use of engineered nanoparticles. Therefore, more and more attention is drawn to the fate of engineered nanoparticles after usage and their removal from aquatic environments. Membrane technology is an emerging technology frequently applied in water purification and can be a solution for nanoparticle removal in water sources since porous membranes are designed to retain colloidal particles. However, nanoparticles are a new, unexplored cause of water contamination, and the application range of membranes for nanoparticle filtration and retention combined with the exact mechanisms responsible for their removal using membranes need to be investigated in order to guarantee safe and secure drinking water in the future as well. The research presented in this thesis aims at providing a better understanding of the fundamental aspects responsible for nanoparticle removal and fouling development during filtration of engineered nanoparticles. The emphasis is put on the role of interparticle interactions in the feed solution, nanoparticle stability and aggregation in relation to the filtration mechanism.

In order to investigate the role of electrostatic interactions during membrane filtration of nanoparticles, a microfiltration hollow fiber membrane was used in constant pressure dead-end mode for the filtration of model silica nanoparticles. A low concentration of nanoparticles in the feed solution and a large difference between the membrane pore size (~200 nm) and the nanoparticle size (25 nm) allow determination of the fouling mechanisms. We postulate that for a stable suspension of electrostatically stabilized nanoparticles fouling occurs in five subsequent stages: adsorption, unrestricted transport through pores, pore blocking, cake filtration and finally cake maturation (**Chapter 2**). After the pore blockage stage, nanoparticle rejection is enhanced from approx. 10% to 90-95%. An increase of the nanoparticle concentration does not change the filtration behavior but only accelerates fouling. Due to the high sensitivity of the stability of electrostatically stabilized nanoparticles to the solution chemistry, the presence of salts, solution pH and valence of the cation strongly influences the duration and severity of the fouling stages. In general, lower repulsive interactions between the nanoparticles accelerate fouling by faster pore blockage and aggregation on the membrane surface. Moreover, porosity and permeability of the formed filtration cake are strongly dependent on the repulsive interactions between the nanoparticles.

In **Chapter 3,** the role of nanoparticle size and polydispersity on fouling development and nanoparticle rejection during dead-end microfiltration of electrostatically stabilized silica nanoparticles was investigated. We demonstrate that bigger monodisperse silica nanoparticles block membrane pores easily, accelerating pore blockage and cake layer formation, acting as secondary membrane responsible for nanoparticle rejection. In the case of polydisperse silica nanoparticles (obtained by mixing monodisperse suspensions in various ratios), an increasing concentration of smaller nanoparticles in the suspension causes delayed pore blockage and cake filtration occurs at a later stage. Moreover, due to the surface charge of the nanoparticles and a less ordered structure of the filtration cake formed due to the polydispersity of the particles in the suspension, the filtration cake has a more porous, open structure. This allows transport of smaller nanoparticles through the filtration cake and the polymeric membrane. As a result, nanoparticle rejection is reduced proportional to the fraction of the smaller nanoparticles present in the feed solution. An increase in transmembrane pressure applied during filtration of the polydisperse suspension causes densification of the filtration cake with only a slight improvement in nanoparticle rejection.

Stabilizers or surface-active compounds added to a feed solution containing nanoparticles change both membrane-nanoparticle and nanoparticle-nanoparticle interactions. An improved stability due to enhanced steric repulsions (introduced by polymers) or stronger surface charges (introduced by low-molecular weight compounds, e.g. surfactants), reduce aggregation of nanoparticles. This facilitates their transport through the porous membrane and increases porosity of the filtration cake formed. On the other hand, stabilizers can also act as foulants, and as such can increase the thickness of the filtration cake and occupy the voids between the nanoparticles in the filtration cake.

Chapter 4 shows that the molecular mass, concentration of the steric stabilizer (in our case PVP) and the transmembrane pressure applied significantly influence the pore blockage and the cake filtration stage during filtration of model silica nanoparticles. In general, PVP with a lower molecular mass is a better stabilizer for nanoparticles and contributes less to fouling by delaying the occurrence of pore blockage. On the other hand, at a higher PVP concentration, PVP contributes to the fouling due to an increase of the total solute load. Moreover, stabilizers with a higher molecular mass block the pores more easily, leading to faster fouling- and rejection development. The nanoparticle rejection drops with increasing PVP concentration and this effect is more pronounced for

low-molecular weight PVP. Use of a higher transmembrane pressures results in compression of the filtration cake and improved nanoparticle rejection at the expense of permeability.

Low-molecular weight compounds such as surfactants are often added to nanoparticle suspensions in order to influence their surface properties and stability. **Chapter 5** demonstrates that the type of surfactant used (anionic, cationic or non-ionic) and its concentration determine the nanoparticle stability. This directly affects the fouling behavior of the nanoparticles and their rejection during dead-end constant flux membrane filtration. Reduced repulsive interactions between nanoparticles due to the addition of non-ionic surfactant (Triton X-100) cause the most severe fouling and the highest nanoparticle rejection. We hypothesize that the difference in nanoparticle rejection in the presence of the investigated surfactants has its origin in the homogeneity and density of the cake layer formed.

Non-homogeneous hydrodynamic conditions over the length of a membrane fiber during inside-out dead-end filtration can result in different fouling development depending on the axial position inside the fiber. **Chapter 6** demonstrates that fouling along the fiber length develops irregularly during filtration of model silica nanoparticles. Moreover, the exact fouling behavior along the hollow fiber membrane is strongly influenced by the applied feed flow rate. However, after the occurrence of pore blockage and the formation of nanoparticle deposit on the membrane surface, rejection of the nanoparticles is no longer determined by the position inside the hollow fiber. Extensive concentration polarization as occurs at some parts of the fiber does not influence significantly the rejection of the silica nanoparticles.

Finally, **Chapter 7** discusses the challenges in nanoparticle filtration and suggests directions for further studies that can contribute to a better understanding of the mechanism of nanoparticle filtration.

Samenvatting

Duurzame ontwikkeling richt zich niet alleen op de voordelen van een bepaalde technologie, maar ook op de nadelen en bedreigingen. Hetzelfde geldt voor nanotechnologie, en dan vooral voor het vervaardigen en het gebruik van nanodeeltjes. Daarom wordt meer en meer de aandacht gevestigd op de bestemming van synthetische nanodeeltjes na gebruik, en het verwijderen ervan uit waterige milieus. Membraantechnologie is een opkomende technologie, veelvuldig toegepast in de waterzuivering. Deze techniek kan een oplossing zijn voor het verwijderen van nanodeeltjes uit waterbronnen omdat poreuze membranen zijn ontworpen om colloïdale deeltjes tegen te houden. Echter, nanodeeltjes zijn een nieuwe en weinig onderzochte oorzaak van verontreinigingen in water. Het toepassingsgebied van membranen voor nanodeeltjes filtratie en -retentie zal onderzocht moeten worden om veilig drinkwater in de toekomst te kunnen garanderen. Dit zal gecombineerd moeten worden met onderzoek naar de exacte mechanismen die ervoor zorgen dat de nanodeeltjes worden verwijderd door deze membranen. Dit proefschrift heeft als doel een beter inzicht te verkrijgen in de fundamentele aspecten verantwoordelijk voor het verwijderen van nanodeeltjes en de membraanvervuiling die optreedt tijdens de filtratie van synthetische nanodeeltjes. De nadruk wordt gelegd op de rol van interacties tussen deeltjes in de voedingsstroom, stabiliteit van de nanodeeltjes, en aggregatie van de nanodeeltjes in relatie tot het filtratiemechanisme.

Om de rol van elektrostatische interacties tijdens membraanfiltratie van nanodeeltjes te onderzoeken, werd een holle vezel microfiltratie membraan gebruikt. Deze werd bij constante druk in dead-end mode gebruikt voor het filtreren van silica nanodeeltjes als modelstof. Een lage concentratie van nanodeeltjes in de voedingsoplossing en een groot verschil tussen de membraan poriegrootte (~200 nm) en de nanodeeltjes grootte (25 nm) maken het mogelijk de vervuilingsmechanismen te onderzoeken. We veronderstellen dat er bij een stabiele suspensie van elektrostatisch gestabiliseerde nanodeeltjes vervuiling optreedt in vijf opeenvolgende fasen: adsorptie, onbeperkt transport door poriën, porie blokkade, koekfiltratie en tenslotte koekontwikkeling (**hoofdstuk 2**). Na het porie blokkade stadium neemt de retentie van de nanodeeltjes toe van ca. 10% tot 90-95%. Een toename van concentratie van de nanodeeltjes verandert de filtratie eigenschappen niet, maar versnelt de vervuiling. De hoge gevoeligheid van de stabiliteit van elektrostatisch gestabiliseerde nanodeeltjes voor de chemie van de oplossing, de aanwezigheid van zouten, de pH en de valentie van het

kation, beïnvloedt in sterke mate de duur en de ernst van de vervuiling. Minder afstoting tussen de nanodeeltjes versnelt porie blokkade en aggregatie op het membraanoppervlak. Bovendien zijn porositeit en permeabiliteit van de gevormde filterkoek sterk afhankelijk van de onderlinge afstoting tussen de nanodeeltjes.

In **hoofdstuk 3** worden de invloed van nanodeeltjesgroote en -polydispersiteit op het vervuilingsgedrag en de retentie tijdens dead-end microfiltratie van elektrostatisch gestabiliseerde silica nanodeeltjes onderzocht. We laten zien dat grotere monodisperse silica nanodeeltjes de blokkade van de membraanporiën vergemakkelijken, het verstoppen van de poriën versnellen, en koeklaag vorming bevorderen. Voor polydisperse silica nanodeeltjes (verkregen door het mengen van monodisperse suspensies in verschillende verhoudingen), resulteert een verhoogde concentratie van kleinere nanodeeltjes in de suspensie in een vertraagde porie blokkade. Koekfiltratie vindt in een later stadium plaats. Door de oppervlaktelading van de nanodeeltjes en een minder geordende structuur van de gevormde filterkoek door de polydispersiteit van de deeltjes in de suspensie, heeft de filterkoek een poreuzere, opener structuur. Dit maakt het transport van kleinere nanodeeltjes door de filterkoek en het polymere membraan mogelijk. Hierdoor wordt de retentie van nanodeeltjes verminderd, evenredig aan de fractie van kleinere nanodeeltjes in de voedingsoplossing. Een toenemende transmembraandruk tijdens het filtreren van de polydisperse suspensie veroorzaakt verdichting van de filterkoek, met slechts een kleine verbetering van de nanodeeltjes afwijzing.

Stabilisatoren of oppervlakte-actieve stoffen, toegevoegd aan een voedingsoplossing met nanodeeltjes, veranderen zowel membraan-nanodeeltje als nanodeeltje-nanodeeltje interacties. Een verbeterde stabiliteit door verhoogde sterische afstotingen (door toevoegen van polymeren) of sterkere oppervlakteladingen (door toevoegen van laagmoleculaire verbindingen zoals oppervlakte-actieve stoffen), vermindert de aggregatie van nanodeeltjes. Dit vergemakkelijkt het transport door het poreuze membraan en verhoogt de porositeit van de gevormde filterkoek. Anderzijds kunnen stabilisatoren zelf ook vervuilers zijn, en als zodanig de dikte van de filterkoek verhogen en de ruimte tussen de nanodeeltjes in deze filterkoek vullen.

Hoofdstuk 4 laat zien dat molecuulgewicht, concentratie van de sterische stabilisator (in ons geval PVP) en de transmembraandruk een aanzienlijke invloed hebben op de porie blokkade en de koekfiltratie tijdens de filtratie van silica nanodeeltjes. Over het algemeen is PVP met een lager molecuulgewicht een betere stabilisator voor

nanodeeltjes, en draagt het minder bij aan de vervuiling omdat de poriën minder snel verstoppen. Aan de andere kant, hogere concentraties PVP dragen resulteren in meer vervuiling vanwege de toename in de totale hoeveelheid opgeloste stoffen. Daarnaast blokkeren stabilisatoren met een hogere molecuulgewicht de poriën makkelijker, wat weer leidt tot een snellere ontwikkeling van vervuiling en retentie. De retentie van de nanodeeltjes daalt met toenemende PVP-concentratie. Dit effect is nadrukkelijker aanwezig bij laagmoleculair PVP. Een hogere transmembraandruk leidt tot samendrukken van de filterkoek en zorgt voor een verbeterde retentie van nanodeeltjes. Dit gaat echter wel ten koste van de permeabiliteit.

Laagmoleculaire verbindingen, zoals oppervlakte-actieve stoffen, worden vaak toegevoegd aan suspensies van nanodeeltjes om hun oppervlakte-eigenschappen en stabiliteit te beïnvloeden. **Hoofdstuk 5** toont aan dat het type oppervlakte-actieve stof (anionisch, kationisch of niet-ionisch) en de concentratie bepalend zijn voor de stabiliteit van de nanodeeltjes. Dit heeft direct effect op het vervuilingsgedrag van de nanodeeltjes en hun retentie tijdens dead-end constant flux membraanfiltratie. Verminderde afstoting tussen de nanodeeltjes door de toevoeging van een niet-ionogene oppervlakte-actieve stof (Triton X-100) veroorzaakt de meest ernstige vervuiling en de hoogste nanodeeltjes retentie. We veronderstellen dat het verschil in retentie van de nanodeeltjes, in aanwezigheid van de onderzochte oppervlakte-actieve stoffen, komt door de homogeniteit en de dichtheid van de gevormde koek.

Niet-homogene hydrodynamische condities over de lengte van een membraanvezel tijdens inside-out dead end filtratie kan resulteren in verschillen in de aangroei van de vervuiling. Dit hangt af van de axiale positie binnen de vezel. **Hoofdstuk 6** toont aan dat vervuiling langs de vezellengte zich onregelmatig ontwikkelt tijdens de filtratie van silica nanodeeltjes. Bovendien wordt het exacte vervuilingsgedrag langs het holle vezel membraan sterk beïnvloed door het toegepaste voedingsdebiet. Echter, nadat de poriën verstoppen en nanodeeltjes zich afzetten op het membraanoppervlak, wordt de retentie van de nanodeeltjes niet meer bepaald door de positie in de holle vezel. Grootschalige concentratie polarisatie, die optreedt in bepaalde delen van de vezels, hebben geen significante invloed op de retentie van de silica nanodeeltjes.

Tenslotte bespreekt **hoofdstuk 7** de uitdagingen bij nanodeeltjes filtratie en geeft aanbevelingen voor verdere studies die kunnen bijdragen aan een beter begrip van het mechanisme van nanodeeltjes filtratie.

Acknowledgements

It is maybe a trivial remark, but, indeed, when I think about last four years it seems like one day. As a fresh PhD you don't realize that someday it will be your task to write an article, a thesis or – the most difficult – to write acknowledgements. Life goes on and today it is my turn to summarize last four years in a couple of sentences. On the one hand, I am happy and proud that I discover a new country, its culture and habits. Within these four years, I developed both professionally and personally and the most important, I meet great people without whom I would not manage all those things. On the other hand, it is very sad that this great adventure is over today. In these few sentences, I would like to express my gratitude to all those who accompanied me during this four years.

Firstly, I would not be where I stand today without two people who gave me the opportunity to start this PhD project, who believed in me and supported me all the time during my work in MST group. First of all, I would like to thank my daily supervisor **Dr.Ir. A.J.B. Kemperman**. Antoine, I really enjoyed working together with you for the past four years. I am very grateful for the freedom you gave me to organize my research, carry out experiments and analysis. I learned a lot from you from the scientific and non-scientific point of view. I am sure that we would have many occasions to meet and talk again. I'd also like to extend my thanks to my promotor, **Prof.Dr.Ir. D.C. Nijmeijer**. Kitty, without your support, enthusiasm and good words my life of a PhD student would be much tougher. Thank you for your guidance and constructive criticism on my work.

I would like to extend my gratitude to my **promotion committee** for reading my thesis and allowing me to defend it. Dr. Pierre Aimar, Prof.Dr.Ir. W.G.J. van der Meer, Prof.Dr.Ir. C.G.P.H. Schroën, Prof.Dr.-Ing. Matthias Wessling and Prof.Dr.Ir. R.G.H. Lammertink, it is an honor for me that such great scientists agreed to be members of my proportion committee. I would also like to thank Prof. Dr. Ir. J.W.M. Hilgenkamp for chairing my defense.

Furthermore, I would like to thank my project **partners from NanoNextNL program**, especially Dr.Ir. Emile Cornelissen and Roberto Floris from KWR, Ron Jong, Stefan Smit, Bernard Bajema from Vitens and Dr.-Ing. Jens Potreck, Dr.Ir. Joris de Groot and Dr. Jeroen Ploegmakers from Pentair X-Flow. I am sure that without your collaboration, support and openness this research would not be possible.

I would like to thank **Felix Broens**, **Chielant de Wit** from Convergence Industry B.V., **Kees de Ruijter** from Wyatt Technology Europe GmbH and **Joop van den Ouweland** from Anthon Paar Benelux BVBA for their flexibility, help and support, which I obtained from them.

Many thanks to the stuff members of MST group who assisted me with their expertise, invaluable support and help: **Prof. Dr. Ir. Erik Roesink**, **Dr. Ir. Wiebe de Vos**, **Dr. Ir. Zandrie Borneman**, **Erik Rolevink**, **Herman Teunis**, **John Heeks**, **Harmen Zwijnenberg**, **Bob Siemerink**, **Greet Kamminga** and **Audrey Haarnack**. It was a pleasure to work with you.

Special thanks to my paranymphs, **Erik V.** and **Damon R.**. Thank you for taking this special role in my defense ceremony. I was really fortunate that you both guys started and fished (almost) at the same time as me. I have no doubt, that without you I would have enjoyed this time much less, I would have partied less and would have done less stupid things. Thank you for disco Damon, smoking brakes outside, lunch gym, body pumping, micronano parties, legendary borels, Salman schools and many many other things, which I can't or shouldn't mention here. It was great time with you guys.

I would like to express my gratitude to all fellow members of MST Group. However, first of all, I would like to thank my office mates: **Herman**, **Erik R**., **Salman**, **Beata**, **Jeroen**, **Shazia**, **Joanna C**. and **Izabella**. Thank you all for a nice atmosphere in the office, for our dissuasions and for time spent together. **Herman** and **Erik. R.**, thank you for your priceless help not only at the beginning of my adventure in MST group but also over those four years. **Beata**, thank you for our conversations in Polish. It was really nice to talk to you about actually everything in my mother tongue (however, I am not sure, if other people in office also liked it). **Jeroen**, it was fun to be your office mate. You had always something funny or smart (or both) to say. I was very happy that we could discuss even more of my scientific problems when you started working for Pentair X-Flow. **Salman**, it was great to share office with you. For sure, I will not forget our legendary parties, courses and the most important, Salman's schools. **Shazia**, thank you for our conversations and your sense of humour. I would like to thank **Joanna C.**, for your endless discussions and motivating me to work in the lab. **Izabella**, thank you for a nice atmosphere in the office and fun you made out of me and other frustrated PhDs at the end of their contract.

Secondly, I would like to thank my students: **Miran**, **Aneta**, **Mariël**, **Sooi Lee**, **Andrew** and **Amin**. It was a pleasure and great fun to work with you. I learned a lot from each one of you. Definitely, without your effort and contribution, this book would be much thinner than it is now. Thanks to you, I took great lessons and had an opportunity to find out how difficult it is to be a supervisor.

I am also very grateful to **Wojtek**, **Can**, **Olga**, **Sinem**, **Joris**, **Harmen** and others mentioned before. I am very happy that I had a chance to meet you all. You created a good atmosphere in the group and will always be my good friends. **Wojtek**, thank you for those years we spent together traveling from Steinfurt. Thank you for your openness, willing to help and understanding. Special thanks to **Can** for his wild ideas (which were even better after Jägermeister), jokes and all the funny moments, which he provoked. Thank you for your crazy PhD defense party, from which I remember only a few things but those things were enough to felt as a real member of the group from that moment on. Thank to **Olga** for being active in the group, for preparation of stukje, groups events and lunch breaks. I can even forgive you for your Latin fanaticism since with you everything was always perfect, extraordinary and unique. **Sinem**, we shared our struggles, difficulties and complaining but there were also good moments and only those I will remember. It was great pleasure to work with you (even on the weekends). **Joris**, I learned a lot from you about membranes, I had great time talking to you and playing football with you and your friends. I was always impressed by you knowledge, intelligence and cleverness. However, now I am quite afraid of your potential. I saw some samples of it when you make jokes about someone or during preparation of stukjes. I hope, in my stukje there is none of your ideas☺. **Harmen**, thank you for all your help and ideas. You had always something interesting to say (not necessary on the subject). Thank you for legendary borrels, which without you woudn't be that legendary.

I would like to express my gratitude to all my colleagues from MST, SFI and IM groups for having fun together during random working days, coffee breaks, borrels, conferences, social events, football games and many other occasions. Also for their smile every day and nasty jokes from time to time: **Anne-Corine IJzer**, **Yali Zhang**, **Enver Güler**, **Mette Birch Kristensen**, **Alessio Fuoco**, **Ramato Ashu**, **Aylin, Kertik**, **Violeta Martin**, **Kah Peng Lee**, **Patrick Goossens**, **Harro Mengers**, **David Vermaas**, **Marcel, Boerrigter**, **Miriam Girones**, **Yusuf Wibisono**, **Terica Sinclair**,

Kanwal Shahid, **Jordi Moreno**, **Björn Heindich**, **Janneke Dickhout**, **Özlem Demirel**, **Charu Basu**, **Vic van Dijk**, **Timon Rijnaarts**, **Parashu Kallem**, **Zeljka Madzarevic**, **Roberto Floris**, **Sander Haase**, **Jeff Wood**, **Elif Karatay**, **Aura Visan**, **Ineke Pünt**, **Jan van Nieuwkasteele**, **Hani Baziar, Ivonne Escalona**, **Hammad Qureshi**, **Khalid Eltayeb**, **Giri Sripathi**, **Martin Wolf**, **Bas ten Donkelaar**, **Marcel ten Hove**, **Michiel Raaijmakers**, **Patrick de Wit**, **Evelien Maaskant**, **Emiel Kappert**, **Kristianne Tempelman**, **Cheryl Tanardi, Anne Benneker**, **Abdulsalam Alhadidi**, **Amy Tsai**, **Pelin Karakiliç**, **Joeri de Valença**, **Renaud Merlet**, **Rian Ruhl**, **Frank Morssinkhof**, **Prof. Dr. Ir. Arian Nijmeijer**, **Prof.Dr.Ir. Nieck Benes**, **Prof.Dr. Henny Bouwmeester**, **Prof.Dr. Louis Winnubst**, **Dr.Ir. Mieke Luiten-Olieman**, **Cindy Huiskes**, **Susanne van Rijn**.

I thank my Polish (and not only) community from Steinfurt and Enschede for tea drinking, great atmosphere and time spent together: **Basia**, **Bram**, **Agnieszka**, **Matteo**, **Kasia S**., **Wojtek**, **Joanna O**., **Szymon**, **Danusia**, **Kasia M.-P.**, **Grzesiek** and **Asia M.**.

Szczególne podziękowania kieruję do moich rodziców **Marii** i **Zbigniewa** za ich trud i wyrzeczenia, jakie włożyli w wychowanie mnie i mojego rodzeństwa. Dziękuję Wam za miłość i wsparcie, jakie towarzyszą mi przez całe życie. Mojemu rodzeństwu: **Annie**, **Katarzynie**, **Andrzejowi** i **Oli** dziękuję za ich troskę i pomoc, które są nie do przecenienia. Dziękuję także moim dziadkom: **Genowefie**, **Władysławowi**, **Emili** i **Stefanowi** za pomoc w wychowaniu mnie oraz za bycie wzorcami do naśladowania.

Mojej ukochanej żonie **Marzenie** chciałbym szczególnie podziękować za jej miłość, wyrozumiałość i wyrzeczenia, jakie ponosi, będące nierzadko konsekwencją moich wyborów życiowych. Dziękuje Ci za to, że ponad trzy lata temu zdecydowałaś się wyjechać do Niemiec i zamieszkać razem ze mną. Wiem, że nie była to łatwa decyzją dla Ciebie a mimo to zdecydowałaś się poświęcić dla naszej wsólnej przyszłości. Dziękuję Ci za to, za nasze przeszłe i przyszłe dni razem!

Filtration of Engineered Nanoparticles using Porous Membranes Krzysztof Trzaskuś 2016

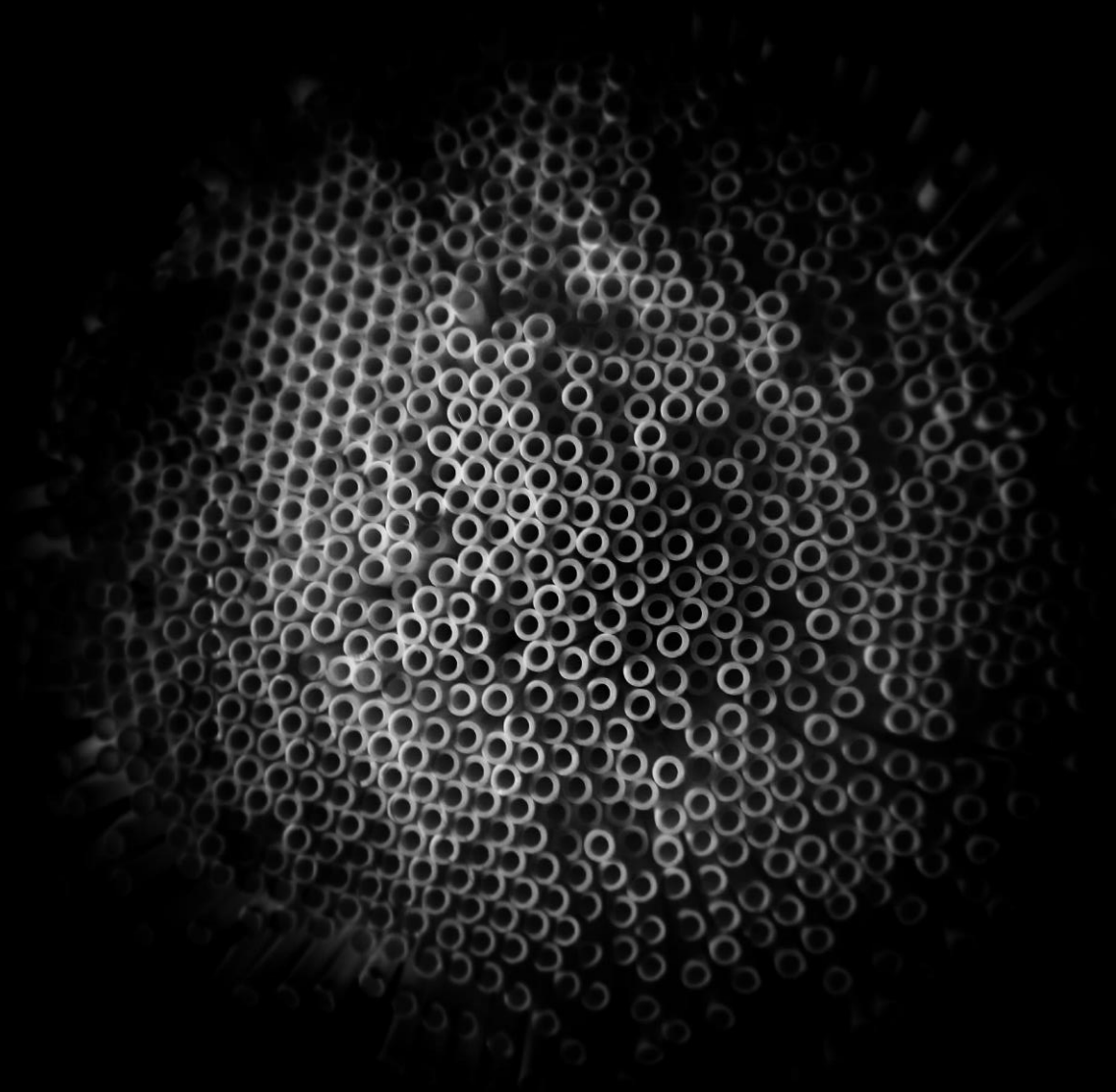

ISBN: 978-90-365-4045-2